Title	Studies on Visible-Light-Driven Photocatalysis on Platinum Nanoparticles/Semiconductor Heterojunction
Author(s)	坂本, 浩捷
Citation	大阪大学, 2017, 博士論文
Version Type	VoR
URL	https://doi.org/10.18910/61815
rights	
Note	

Studies on Visible-Light-Driven Photocatalysis on Platinum Nanoparticles/Semiconductor Heterojunction

Hirokatsu Sakamoto

March 2017

Studies on Visible-Light-Driven Photocatalysis on Platinum

Nanoparticles/Semiconductor Heterojunction

A dissertation submitted to
The Graduate School of Engineering Science
Osaka University
In partial fulfillment of the requirements for the degree of
Doctor of Philosophy in Engineering

By

Hirokatsu Sakamoto

March 2017

Abstract

There has been much interest in the development of metal nanoparticles/semiconductor heterojunction because it has attracted much attention to application for visible-light-driven photocatalyst due to the generation of hot electrons by the wide visible light absorption (400–800 nm) of metal nanoparticles. Although many research groups have studied this photocatalytic system driven by an absorption of visible light by gold (Au) nanoparticles due to their intraband transition, their activities are insufficient. The main objective of this thesis is to develop the highly efficient visible-light-driven photocatalysis based on interband transition of platinum (Pt) nanoparticles. This thesis consists of the following three chapters.

In Chapter I, photocatalytic activity of Pt nanoparticles/titanium dioxide (TiO_2) heterojunction was studied. Pt nanoparticles were supported on Degussa P25 TiO_2, a mixture of anatase and rutile TiO_2. The obtained Pt/P25 catalysts efficiently promote aerobic oxidation of aniline under visible light (λ >450 nm), and produce nitrosobenzene with high selectivity (~90 %). In that, Pt nanoparticles produce hot electrons (e_{hot}^-) by absorbing of visible light. The formed e_{hot}^- are injected into P25 TiO_2 conduction band (CB) by overcoming the Schottky barrier created at the Pt–TiO_2 interface, resulting in the charge separation. The CB electrons reduce molecular oxygen (O_2), while the positive charge formed on Pt nanoparticles oxidizes aniline. The high activity of Pt/P25 is due to the high electron density of Pt nanoparticles. They behave as Lewis base sites for reductive deprotonation of aniline, promoting efficient aniline oxidation. The nitrosobenzene selectivity strongly depends on the reaction temperature. At high temperature, azobenzene is produced as byproduct, which is formed by subsequent condensation of aniline and the formed nitrosobenzene. Pt/P25 catalysts promotes aerobic oxidation of aniline under visible light at a low temperature (~283 K), and successfully produce nitrosobenzene with a very high selectivity by suppressing the condensation of aniline and nitrosobenzene.

In Chapter II, Pt–copper (Cu) bimetallic alloy nanoparticles were supported on TiO_2 (PtCu/TiO_2) for the activity improvement of the Pt/TiO_2 system. PtCu/TiO_2 promote aerobic oxidation under visible light irradiation with high quantum yields (17 %, 550 nm), which is much higher than that obtained on the Pt/TiO_2 (~7 %). Cu alloying with Pt decreases the work function of nanoparticles due to the lower work function of Cu, and decreases the height of Schottky barrier created at the metal nanoparticles/TiO_2 interface. This thus efficiently promotes the e_{hot}^- injection from photoactivated Pt to TiO_2 CB, resulting in enhanced photocatalytic activity. The mole fraction of Cu in the alloy and the size of metal nanoparticles strongly depend on the photocatalytic activity. The catalyst loaded with alloy nanoparticles, consisting of 80 mol % of Pt and 20 mol % Cu with 3–5 nm diameter, exhibits the highest activity.

In Chapter III, Pt nanoparticles were loaded on tantalum oxide (Ta_2O_5) and used for photocatalytic reactions. The author found that the Pt/Ta_2O_5 catalyst promotes aerobic oxidation under visible light with significant high quantum yields (25 % at 550 nm). In the Pt/TiO_2 system, the e_{hot}^- formed on the Pt are injected into the TiO_2 CB by overcoming the Schottky barrier. The e_{hot}^- injection is the rate-determining step, and the Pt/TiO_2 system exhibits low photocatalytic activity. However, in the Pt/Ta_2O_5 system, the e_{hot}^- are not injected into Ta_2O_5 conduction band due to the high Schottky barrier. Strong $Pt–Ta_2O_5$ interaction increases the electron density of Pt nanoparticles by promoting electron transfer from Ta_2O_5 to Pt nanoparticles. A large number of e_{hot}^- are therefore produced on the photoactivated Pt nanoparticles by the enhanced interband transition of Pt electrons. These e_{hot}^- directly activate O_2 on the Pt surface and efficiently produce active oxygen species, thus promoting efficient aerobic oxidation. There has been no report of photocatalytic system without e_{hot}^- injection from metal nanoparticles to semiconductor. This new concept may contribute to the creation of highly efficient photocatalytic system driven under visible light.

This thesis described the visible-light driven photocatalysts based on Pt nanoparticles/semiconductor heterojunction, and suggested for the structural design for highly efficient photocatalysts driven under visible light.

Preface

This dissertation work was carried out under the joint supervision of Professor Dr. Takayuki Hirai and Associate Professor Dr. Yasuhiro Shiraishi at the Research Center for Solar Energy Chemistry, and Division of Chemical Engineering, Graduate School of Engineering Science, Osaka University from 2012 to 2017.

The objective of this thesis is to create highly efficient visible-light-driven photocatalysts based on platinum (Pt) nanoparticles/semiconductor heterojunction. The author hopes that the results obtained in this work would give some suggestions for the future development of highly efficient photocatalysts driven under visible light.

Hirokatsu Sakamoto

Division of Chemical Engineering

Graduate School of Engineering Science

Osaka University

Toyonaka 560-8531, Japan

CONTENTS

General Introduction

"*Solar Energy*" is an energy source that attracts a lot of attention as one of the renewable energy sources, and is expected to as a new energy source to replace fossil fuels such as coal, oil, and natural gas.[1] A long time ago, human beings used firewood as an energy source to their easy life, but the energy consumption is only little. Since the Industrial Revolution in the 18th century, human beings has used coal as an energy source to power source of steam engine. The energy consumption has rapidly increased with the development of industry in exchange for convenient and prosperous life. According to the improvement of scientific technology and the further increase in the energy consumption and expansion of the application such as factory, transportation, and electric power generation, human beings have used oil as an energy source. The lives therefore became more comfortable and wealth, and the energy consumption and world population explosively increased. Heavy consumption of fossil fuels, however, induced the problem of depletion of limited fossil fuels and the environment issue such as global warming. The technology of using solar energy, which is one of the renewable energy sources, has been developed to reduce the dependence of fossil fuels and environmental burdens, especially since Oil Crisis of 1973–1974.[2]

Renewable energy is generally defined as energy that is derived from natural processes that are naturally replenished at more speed than consumption such as sunlight, wind, rain, tides, and geothermal heat.[3] Renewable energy sources exist around the world in contrast to fossil fuels, which are concentrated in a limited number of countries. Especially, solar energy, which is radiant light and heat from solar irradiance, consists of ultraviolet light (UV) (~6 %), visible light (~45 %), and near-infrared light (IR) (~49 %),[4] has attracted attention due to its vast amounts of energy. The amounts of solar energy reaching the surface of the earth is much larger than the total world energy consumption. The efficient utilization of solar energy is therefore considered to be a key to solve the energy and environmental problems. Solar energy has been studied at the various fields such as photovoltaic generation, artificial photosynthesis, and photocatalysis.

Photocatalysis has a potential to efficiently utilize solar energy for hydrogen (H_2) production and carbon dioxide (CO_2) reduction, redox reactions of organic compounds at room temperature. Photocatalysts has therefore attracted much attention for future hydrogen society (H_2 production), solution of global warming problem (CO_2 reduction), and chemical industry (redox of organic compounds). In the photocatalysis, titanium dioxide (TiO_2) has been widely studied. TiO_2 has been used as paints, pigments, cosmetics, medicines or foods because it is abundant, inexpensive, harmless and chemically and photochemically stable. In 1972, Fujishima and Honda discovered the photoelectrocatalysis of water (H_2O) into H_2 and O_2 using a platinum (Pt) metal electrode as cathode and a TiO_2 photoanode with UV irradiation.[5] They found that UV

irradiation to the TiO_2 electrode promotes water splitting at much lower bias voltage as compared to normal electrolysis. Since this report and oil crisis in 1973, the TiO_2 photocatalysis has extensively been investigated by many researchers for the generation of clean energy such as H_2 from H_2O. Schrauzer and Guth reported that photoactivated TiO_2 produces H_2 and O_2 from water under UV irradiation and ammonia (NH_3) from nitrogen (N_2) and H_2O.[6] Frank and Bard reported that photoactivated TiO_2 powders promote photocatalytic oxidations of inorganic anions such as CN^- and SO_3^{2-}.[7] Kraeutler and Bard applied TiO_2 photocatalysts to photodecomposition of organic compounds.[8] Inoue et al. reported that TiO_2 also promote photocatalytic reduction of CO_2.[9] These pioneering reports accelerated the investigation of TiO_2 photocatalysis.
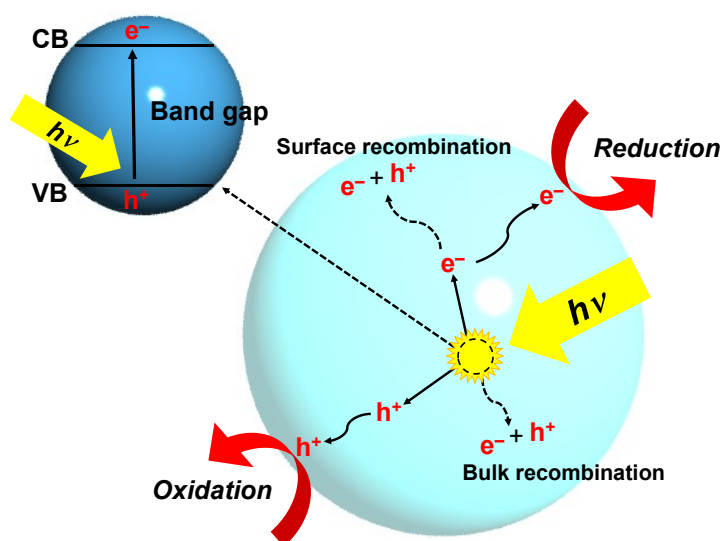
Figure 1. The mechanism for photocatalytic reaction with semiconductor photocatalysts.

The mechanism for photocatalysis by semiconductor photocatalysts has been clarified by many researchers.[10] **Figure 1** describes the mechanism for photocatalytic reaction with semiconductor under the photoirradiation. When semiconductor absorbs light ($h\nu$) with the energy equal to or larger than their band gap energy (E_G) ($h\nu \geq E_G$), the electrons of the valence band (VB) is excited to the conduction band (CB), and photoexcited electrons (e^-) and holes (h^+) are generated in the CB and VB, respectively. The e^- induce reduction reactions at the semiconductor surface, while the h^+ induce oxidation reactions, although some e^-–h^+ pairs are deactivated by recombination at bulk and surface of semiconductor.

TiO_2 efficiently promotes various photocatalytic reactions such as organic transformation, water splitting, and CO_2 reduction under UV irradiation. TiO_2 is, however, a wide band gap semiconductor (3.0–3.2 eV), which corresponds to the energy of ca. 400 nm wavelength light. This indicates that TiO_2 cannot utilize the light in visible wavelength region (400–800 nm). It is well known that UV light (λ <400 nm) only accounts for ~6 % of solar radiation. This means that only small portion of solar light can be utilized for

TiO₂ photocatalysis. The creation of visible-light-driven photocatalysts is therefore an important issue for efficient utilization of solar energy.
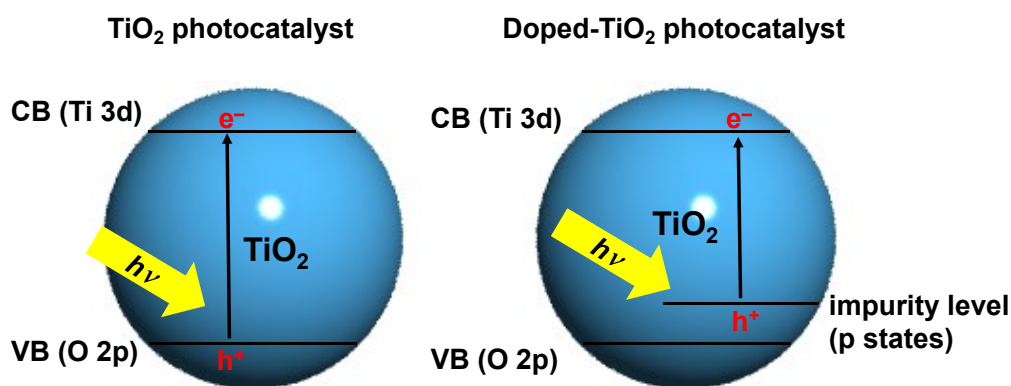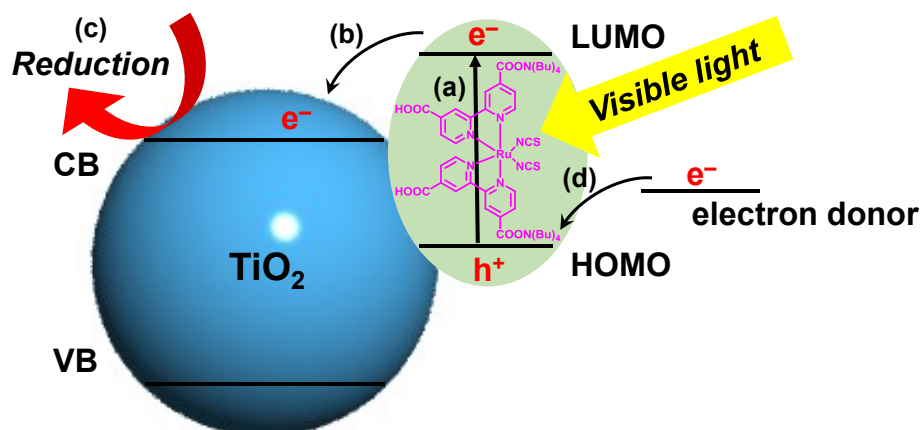

Figure 2. Schematic representation for the mechanism for photocatalytic reaction with TiO_2 photocatalyst and doped TiO_2 photocatalyst.

Many research groups have investigated to extend photoresponse of TiO_2 into visible region. First approach is the use of TiO_2 doped with nonmetal elements. In 1986, Sato reported that nitrogen (N)-doped TiO_2 promotes oxidation of CO or ethane even under visible light irradiation ($\lambda = 434$ nm).[11] In 2001, Asahi et al. reported that N-doped TiO_2 have narrower bandgap and significant enhancement of photocatalytic activities under visible light.[12] Since this report, N-doped TiO_2 has attracted considerable attention until now. Various types of TiO_2 doped with non-metal elements such as N,[12] sulfur (S),[13] carbon (C),[14] boron (B),[15] iodine (I)[16] and oxyhalide[17] have been considerably studied as visible-light-driven photocatalysts. The doping of non-metal elements into TiO_2 leads to a reduction in the bandgap of TiO_2 and extends the absorption edge into the visible light region. The electronic structure of doped TiO_2 has been studied by ab initio calculations.[18] This consists of nonbonding of O 2p orbital at the top of the valence bands (VBM : valence band maximum) and the nonbonding of Ti 3d orbital at the bottom of the conduction bands (CBM : conduction band minimum). As shown in **Figure 2**, the VB and CB of TiO_2, therefore, consists of O 2p orbital and Ti 3d orbital, respectively. When doping nonmetal elements into TiO_2, the atomic p level of doping species is formed above the O 2p VBM. The newly formed bandgap between Ti 3d states and doping species p states therefore contribute to the bandgap narrowing of TiO_2 and shows photocatalytic activity under visible light. These doped catalysts, however, suffer from low quantum yields for the photocatalytic reactions because of lattice defect formed by doping. When nonmetal elements are doped into TiO_2, doping species are replaced with O in the TiO_2 lattice. This creates a large number of lattice defects that behave act as recombination centers of electron and hole generated by photoexcitation of TiO_2.[19] In addition, these

catalysts are oxidized during photocataytic reaction because these non-metal elements are oxidized easily.
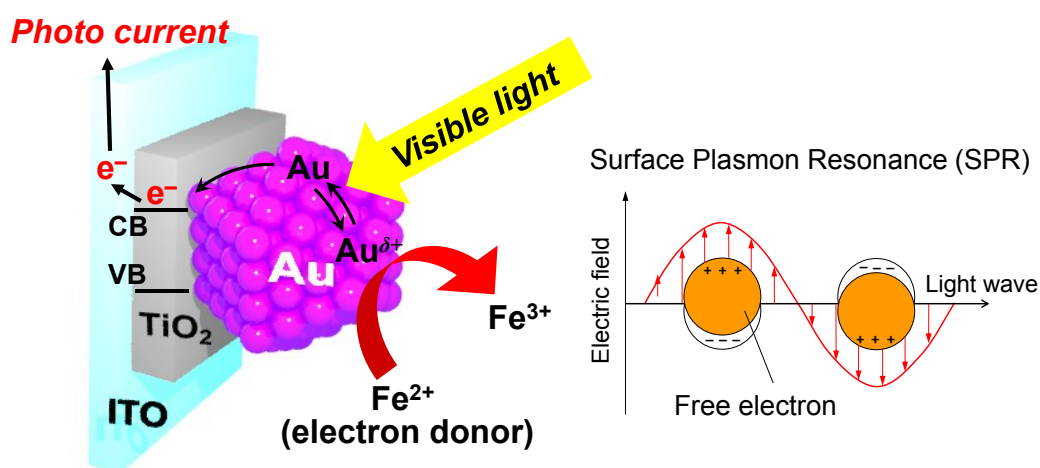

Figure 3. Schematic representation for the mechanism for photocatalytic reaction with dye sensitized TiO_2 photocatalyst.

Second approach is the use of dye sensitization. Photosensitization of TiO_2 by dyes has been widely studied to extend the photoresponse of TiO_2 into the visible region. Spitler reported that photosensitized-dye-modified TiO_2 electrodes exhibit photocatalytic activity for reduction of O_2 under visible light irradiation.[20] Clark et al. reported that TiO_2 electrodes sensitized by ruthenium (Ru) complexes promotes photocatalytic reactions such as H_2 generation from H_2O or redox reaction of I^- under visible light.[21] Kisch et al. reported that platinum(IV) chloride ($PtCl_4$) modified TiO_2 promotes photodecomposition of 4-chlorophenol under visible light.[22] The mechanism for photocatalytic reaction on the dye-sensitized TiO_2 is illustrated in **Figure 3**.[23] Under irradiation of visible light, the attached sensitizer is photoexcited by absorbing visible light and produces excited electrons (a). The formed electrons are injected from excited sensitizer to the CB of TiO_2 (b). The injected electrons on the TiO_2 CB reduce substrates (c), while the sensitizer is regenerated by oxidizing electron donors (d). The sensitized TiO_2 photocatalysts, however, suffer from low quantum yield due to the low efficiency of charge transfer from photoexcited sensitizer to TiO_2. In addition, these catalysts cannot be used for long time operation due to the desorption of sensitizer from TiO_2 during photocatalytic reactions.[24]

The other approach is the use of localized surface plasmon resonance (LSPR) of noble metal nanoparticles. Nanosized noble metals such as gold (Au), silver (Ag) and copper (Cu) can absorb light in the visible region (400–800 nm) because of resonant oscillation of free electrons interacted with particular frequency of the light, known as LSPR.[25] The photoabsorbed noble metals produce hot electrons (e_{hot}^-) due to the intraband transition of free electrons from the sp band to the sp-conduction band.[26] In 2004, Tian et

al. found that LSPR of Au or Ag nanoparticles are able to promote photocatalysis for the first time.[27] Visible light irradiation to Au or Ag nanoparticles loaded on TiO_2 film that is coated on an indium tin oxide (ITO) electrode generates an anodic photocurrent in the presence of iron cation (Fe^{2+}) under visible light irradiation ($\lambda > 420$ nm). The mechanism of this photoelectrocatalytic system is similar to the dye sensitized TiO_2 (**Figure 3**): the e_{hot}^- are produced by LSPR of Au or Ag nanoparticles by absorbing visible light and are transferred to the TiO_2 CB. Simultaneously, the positively charged metal nanoparticles receive electrons from the electron donors (Fe^{2+}), thus completing the photocatalytic cycles (**Figure 4**).[28] Since this report, plasmonic metal–supported photocatalysts have been studied extensively as a new class of visible-light-driven photocatalysts. Rodríguez-González et al. reported that Au nanoparticles supported on TiO_2 promote photodecomposition of organic substrates under visible light ($\lambda = 495$ nm).[29] Kowalska et al. reported that Au nanoparticles loaded on TiO_2 photocatalysts promote photooxidation of 2-propanol under visible light.[30] Silva et al. reported that Au nanoparticles supported on TiO_2 exhibit photocatalytic activity for the generaton of H_2 from H_2O in the presence of methanol as a sacrificial agent under visible light irradiation ($\lambda > 400$ nm).[31]

Figure 4. Schematic representation of photoelectrocatalysis on Au nanoparticles loaded on TiO_2 under visible light irradiation.

The mechanism for supported plasmonic metal nanoparticles photocatalysts is explained by an electron transfer mechanism. Under irradiation of visible light, the e_{hot}^- produced by LSPR of metal nanoparticles are injected into the semiconductor CB, leading to charge separation. The contact of metal with semiconductor leads to an electron transfer between semiconductor and metals due to the difference of their Fermi level.[32] In the case of the metal and n-type semiconductor such as TiO_2, the metal work function (W_{metal}) is higher than that of semiconductor (W_{semi}). In this case, as shown in **Figure 5**, the semiconductor

electrons are therefore transferred to the metal until the Fermi levels of metal ($E_{F,metal}$) and semiconductor ($E_{F,semi}$) are aligned. As a result of this, the metal is charged negatively, and the semiconductor is charged positively at the interface due to the electrostatic induction. The positively charged semiconductor surface therefore creates a depletion layer. In that, the energy band edges in the semiconductor are shifted continuously due to the electric field between the semiconductor and metal, which is called band bending, and the energy bands bend upward toward the interface. The energy barrier, called Schottky barrier (ϕ_B), is therefore created at the interface (**Figure 5**).[33] Therefore, in the Au nanoparticles loaded on TiO$_2$ (Au/TiO$_2$) system, Schottky barrier is created at the interface between Au and TiO$_2$. As shown in **Figure 6**, visible light irradiation of the Au/TiO$_2$ system produces e_{hot}^- due to LSPR of Au nanoparticles by absorbing visible light. The e_{hot}^- is injected into the TiO$_2$ CB by overcoming the Schottky barrier, leaving the positive charges (hot holes, δ^+) on the Au particles. The recombination of the CB electrons (e_{CB}^-) and hot holes is suppressed by the Schottky barrier and, hence, the charges are separated efficiently. The hot holes promotes oxidization, while the e_{CB}^- promotes reduction (**Figure 6**),[34] thus exhibiting photocatalytic activity under visible light. The quantum yields for the photocatalytic reactions are, however, low although much higher than those obtained by the doped TiO$_2$ and the dye sensitized TiO$_2$ catalysts. In the Au/TiO$_2$ system, the injection of e_{hot}^- into TiO$_2$ CB is the rate-determining step for the plasmonic photocatalysis, but the step is very slow.[35] Development of the system that efficiently promotes the e_{hot}^- injection is necessary. Pt particles can also absorb visible light, although the absorption band of LSPR of Pt exist in the UV region.[26] In the visible region, Pt particles exhibit absorption band assigned to the interband transition of 5d electrons from 5d band to 6sp-CB because Pt has 5d band around the Fermi energy (**Figure 7**). Pt nanoparticles loaded on TiO$_2$ catalysts is therefore one of the possible ways to promote photocatalytic reaction under visible light irradiation as with Au/TiO$_2$, although there is no report of photocatalytic system based on visible light absorption of Pt nanoparticles. In addition, Pt nanoparticles strongly adsorb on the TiO$_2$ surface rather than Au nanoparticles.[35] In that, the strong Pt–TiO$_2$ interaction may efficiently promote e_{hot}^- injection to TiO$_2$, and would exhibit much higher photocatalytic activity than those on Au/TiO$_2$.
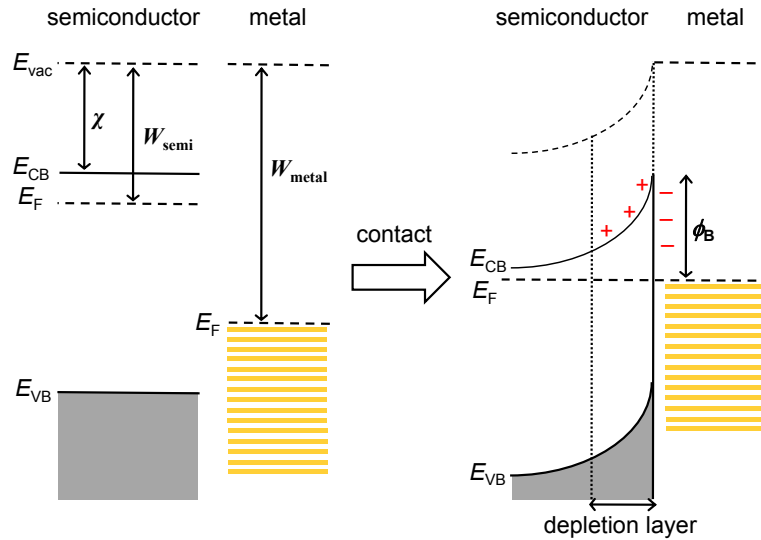
Figure5. Energy band diagrams of metal and n-type semiconductor contacts.
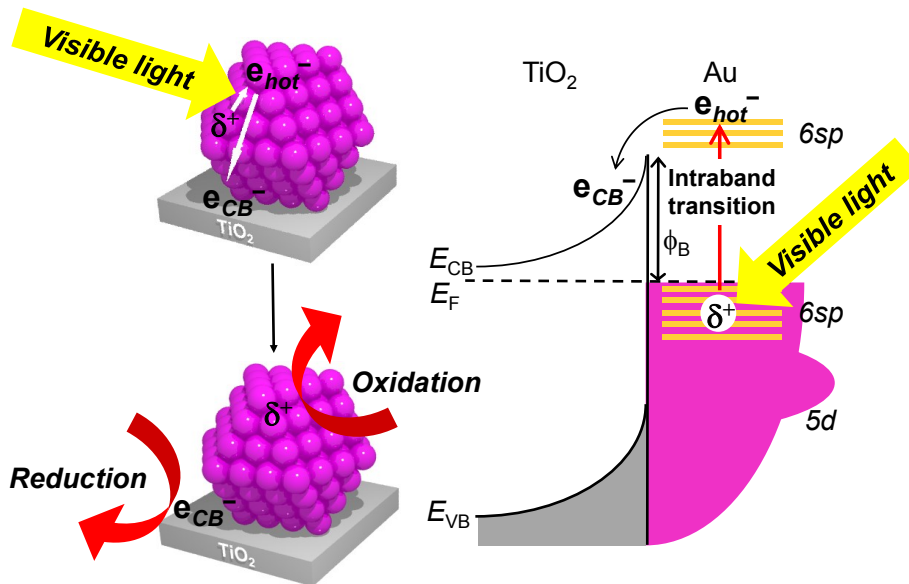
Figure 6. Schematic representation for photocatalytic reaction with Au–TiO₂ heterojunction system under visible light irradiation.

In the metal–semiconductor heterojunction, the e_{hot}^- injection into semiconductor occurs via overcoming the Schottky barrier and is the rate-determining step for photocatalysis. Further improvement of the photocatalytic activity, creation of the system that promotes efficient e_{hot}^- injection to semiconductor CB or promotes redox reactions on the metal nanoparticles without e_{hot}^- injection into semiconductor (non e_{hot}^- injection mechanism) is one of the possible way. The former approach is to decrease the Schottky barrier height. The Schotkky barrier is defined as the difference between W_{metal} and the electron affinity of the semiconductor CB (χ):[33]

$$\phi_B = W_{metal} - \chi \qquad (1)$$

This suggests that the decrease in W_{metal} may decrease the height of Schottky barrier, and would promote photocatalysis under visible light irradiation. In contrast, the use of a semiconductor with small χ creates high Schottky barrier, resulting in suppression of e_{hot}^- injection, which is the latter approach for the activity enhancement. Therefore, increasing electron density of metal may promote photocatalysis under visible light irradiation due to generating a large number of e_{hot}^-. As mentioned before, the contact of metal with semiconductor leads to an electron transfer between semiconductor and metals due to the difference of their Fermi level. In that, strong metal–semiconductor interaction may promote electron donation from semiconductor to metal, and increase electron density of metal. In the case of reducible metal oxide semiconductor, metal oxide strongly interacts with metal by high temperature H_2 treatment, known as strong metal–support interaction (SMSI).[36] The oxygen vacancies of the metal oxide adjacent to the reduced metal cations facilitate strong adhesion of metal, resulting in forming strong metal–metal cation bonding. This thus induces efficiently electron transfer from metal oxide to metal, and increases the electron density of metal. This suggests that a large number of e_{hot}^- generated on the metal may directly promote redox reactions, and would promote photocatalysis under visible light irradiation.
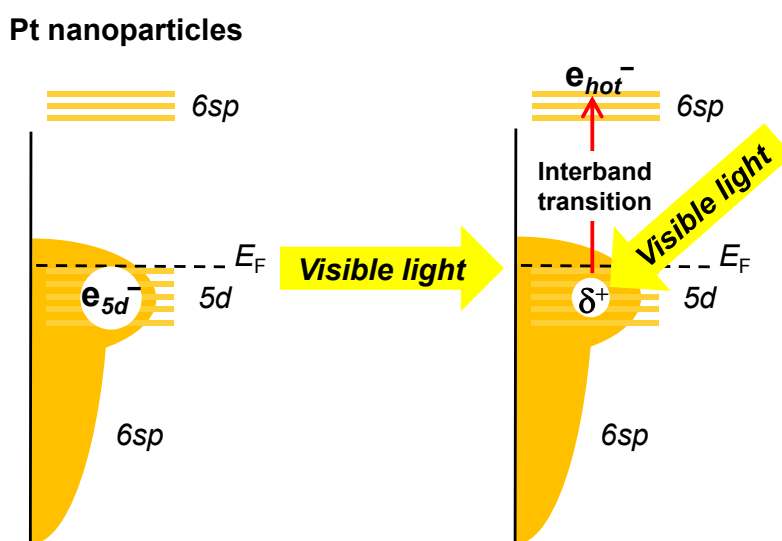
Figure 7. Schematic representation of hot electrons generation by interband transition of Pt nanoparticles from 5d band to 6sp band under visible light irradiation.

The purpose of this thesis is to design highly efficient visible-light-driven photocatalysts based on Pt nanoparticles/semiconductor heterojunction. The main objective of this thesis is the creation of Pt

nanoparticles/semiconductor heterojunction that exhibits higher photocatalytic activity than Au nanoparticles/semiconductor systems. The framework of the present study is shown in **Figure 8**.
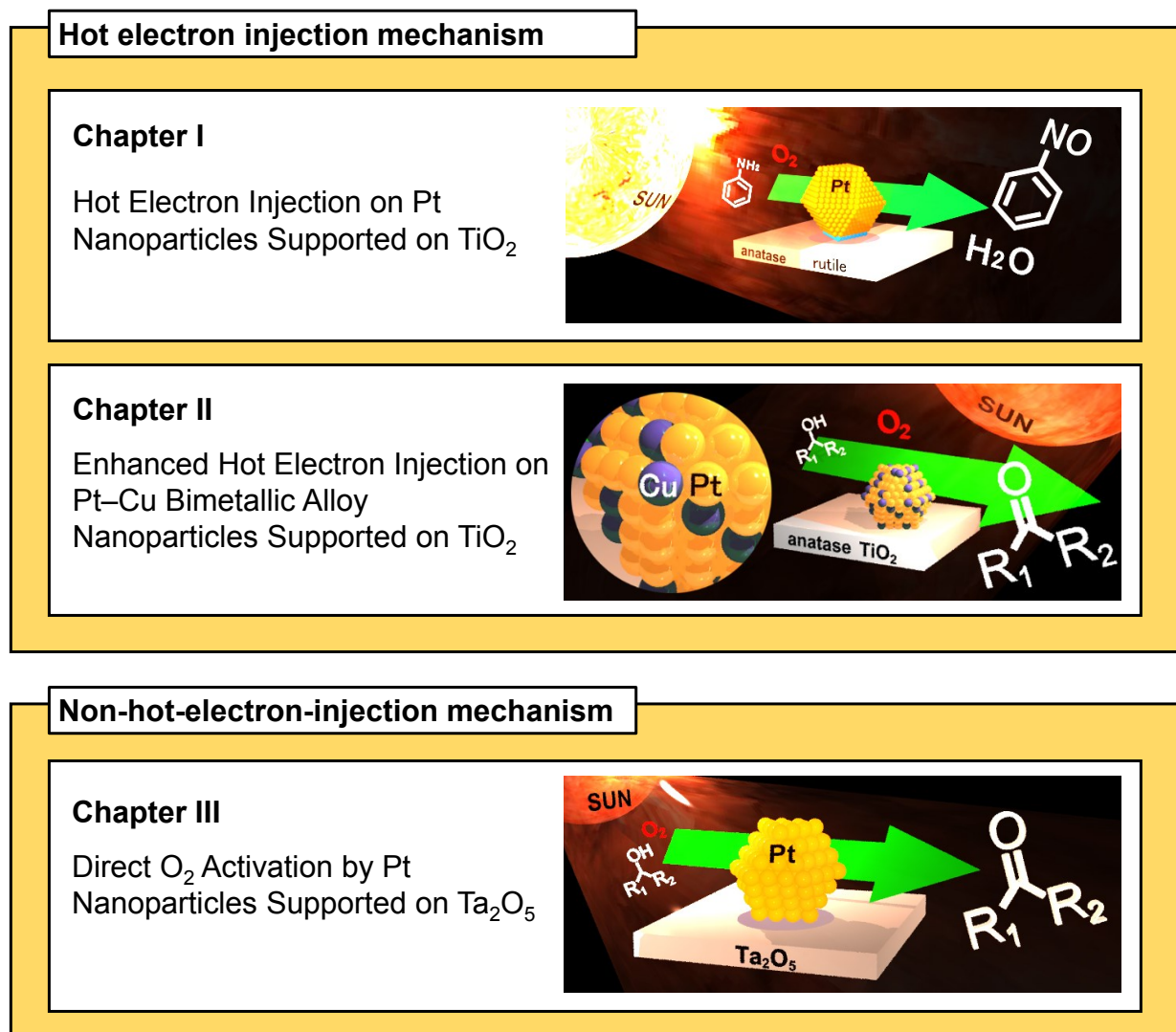
Figure 8. Framework of the present study.

This thesis consists of three chapters. Chapter I described that Pt nanoparticles supported on TiO_2 (Pt/TiO_2) efficiently promote aerobic oxidation of aniline under visible light with much higher activity and selectivity for nitrosobenzene production than those on Au/TiO_2. Chapter II described that Pt–Cu bimetallic alloy nanoparticles supported on TiO_2 (PtCu/TiO_2) promote aerobic oxidation of alcohols with higher activity than Pt/TiO_2. In that, the decreased Schottky barrier by the Cu alloying efficiently promotes the e_{hot}^- injection to TiO_2. Chapter III described that Pt nanoparticles supported on tantalum oxide (Ta_2O_5) (Pt/Ta_2O_5) promote aerobic oxidation of alcohols with significantly high activity. In that, the e_{hot}^- directly activate O_2 on the Pt surface due to the high Schottky barrier and efficiently produce active oxygen species, thus

promoting efficient aerobic oxidation.

In Chapter I, photocatalytic activity of Pt nanoparticles/TiO$_2$ heterojunction was studied. The author synthesized Pt/P25 catalysts, which is Pt nanoparticles supported on Degussa P25 TiO$_2$, a mixture of anatase and rutile TiO$_2$, and found that the obtained Pt/P25 catalysts efficiently promote aerobic oxidation of aniline under visible light (λ >450 nm), and produce nitrosobenzene with high selectivity (~90 %). In that, Pt nanoparticles produce e$_{hot}^-$ by absorbing of visible light. The formed e$_{hot}^-$ are injected into P25 TiO$_2$ CB by overcoming the Schottky barrier created at the Pt–TiO$_2$ interface, resulting in the charge separation. The CB electrons reduce O$_2$, while the positive charge formed on Pt nanoparticles oxidizes aniline. The high activity of Pt/P25 is due to the high electron density of Pt nanoparticles. They behave as Lewis base sites for reductive deprotonation of aniline, promoting efficient aniline oxidation. The nitrosobenzene selectivity strongly depends on the reaction temperature. At high temperature, azobenzene is produced as byproduct, which is formed by subsequent condensation of aniline and the formed nitrosobenzene. Pt/P25 catalysts promotes aerobic oxidation of aniline under visible light at a low temperature (~283 K), and successfully produce nitrosobenzene with a very high selectivity by suppressing the condensation of aniline and nitrosobenzene.

In Chapter II, Pt–Cu bimetallic alloy nanoparticles were supported on TiO$_2$ (PtCu/TiO$_2$) for the activity improvement of the Pt/TiO$_2$ system. The author found that PtCu/TiO$_2$ promote aerobic oxidation under visible light irradiation with high quantum yields (17 %, 550 nm), which is much higher than that obtained on the Pt/TiO$_2$ (~7 %). Cu alloying with Pt decreases the work function of nanoparticles due to the lower work function of Cu, and decreases the height of Schottky barrier created at the metal nanoparticles/TiO$_2$ interface. This thus efficiently promotes the e$_{hot}^-$ injection from photoactivated Pt to TiO$_2$ CB, resulting in enhanced photocatalytic activity. The mole fraction of Cu in the alloy and the size of metal nanoparticles strongly depend on the photocatalytic activity. The catalyst loaded with alloy nanoparticles, consisting of 80 mol % of Pt and 20 mol % Cu with 3–5 nm diameter, exhibits the highest activity.

In Chapter III, Pt nanoparticles were loaded on tantalum oxide (Ta$_2$O$_5$) and used for photocatalytic reactions. The author found that the Pt/Ta$_2$O$_5$ catalyst promotes aerobic oxidation under visible light with significant high quantum yields (25 % at 550 nm). In the Pt/TiO$_2$ system, the e$_{hot}^-$ formed on the Pt are injected into the TiO$_2$ CB by overcoming the Schottky barrier. The e$_{hot}^-$ injection is the rate-determining step, and the Pt/TiO$_2$ system exhibits low photocatalytic activity. However, in the Pt/Ta$_2$O$_5$ system, the e$_{hot}^-$ are not injected into Ta$_2$O$_5$ conduction band due to the high Schottky barrier. Strong Pt–Ta$_2$O$_5$ interaction increases the electron density of Pt nanoparticles by promoting electron transfer from Ta$_2$O$_5$ to Pt nanoparticles. A large number of e$_{hot}^-$ are therefore produced on the photoactivated Pt nanoparticles by the

enhanced interband transition of Pt electrons. These e_{hot}^- directly activate O_2 on the Pt surface and efficiently produce active oxygen species, thus promoting efficient aerobic oxidation. There has been no report of photocatalytic system without e_{hot}^- injection from metal nanoparticles to semiconductor. This new concept may contribute to the creation of highly efficient photocatalytic system driven under visible light.

The results obtained in this work are summarized in general conclusions. Suggestions for future work are described as an extension of the present work.

References

[1] REN21, *Global Status Report 2016*, June 8, **2016**.

[2] Heidari, N.; Pearce, J. M. *Renew. Sus. Energy Rev.* **2016**, *55*, 899–908.

[3] (a) Omar, E.; Haitham, A.-R.; Frede, B. *Renew. Sus. Energy Rev.* **2014**, *39*, 748–764. (b) Jacobson, M. Z.; Delucchi, M. A.; Bazouin, G.; Bauer, Z. A. F.; Heavey, C. C.; Fisher, E.; Morris, S. B.; Piekutowski, D. J. Y.; Vencill, T. A.; Yeskoo, T. W. *Energy Environ. Sci.* **2015**, *8*, 2093–2117.

[4] Levinson, R.; Akbari, H. *Energy Efficiency*, **2010**, *3*, 53–109.

[5] Fujishima, A.; Honda, K. *Nature* **1972**, *238*, 37–38.

[6] Schrauzer, G. N.; Guth, T. D. *J. Am. Chem. Soc.* **1977**, *99*, 7189–7193.

[7] Frank, S. N.; Bard, A. J. *J. Phys. Chem.* **1977**, *81*, 1484–1488.

[8] Kraeutler, B.; Bard, A. J. *J. Am. Chem. Soc.* **1978**, *100*, 2239–2240.

[9] Inoue, T.; Fujishima, A.; Konishi, S.; Honda, K. *Nature* **1979**, *277*, 637–638.

[10] (a) Gerischer, H. *Electroanal. Chem. Interfacial Electrochem.* **1975**, *58*, 263–274. (b) Herrmann, J.-M. *Topics Catal.* **2005**, *34*, 49–65. (c) Shiraishi, Y.; Hirai, T. *J. Photochem. Photobiol. C: Photochem. Rev.* **2008**, *9*, 157–170.

[11] Sato, S. *Chem. Phys. Lett.* **1986**, *123*, 126–128.

[12] (a) Ashahi, R.; Morikawa, T.; Ohwaki, T.; Aok, K.; Taga, Y. *Science*, **2001**, *293*, 269–271. (b) Miyauchi, M.; Ikezawa, A.; Tobimatsu, H.; Irie, H.; Hashimoto, K. *Phys. Chem. Chem. Phys.* **2004**, *6*, 865−870.

[13] (a) Umebayashi, T.; Yamaki, T.; Itoh, H.; Asai, K. *Appl. Phys. Lett.* **2002**, *81*, 454–456. (b) Yan, X.; Ohno, T.; Nishijima, K.; Abe, R.; Ohtani, B. *Chem. Phys. Lett.* **2006**, *429*, 606−610.

[14] (a) Sakthivel, S.; Kisch, H. *Angew. Chem., Int. Ed.* **2003**, *42*, 4908–4911. (b) Irie, H.; Watanabe, Y.; Hashimoto, K. *Chem. Lett.* **2003**, *32*, 772−773.

[15] (a) Zhao,W.; Ma, W.; Chen, C.; Zhao, J.; Shuai, Z.; *J. Am. Chem. Soc.* **2004**, *126*, 4782–4783. (b) Zaleska, A.; Sobczak, J. W.; Grabowska, E.; Hupka, *J. Appl. Catal., B* **2008**, *78*, 92−100.

[16] (a) Hong, X.; Wang, Z.; Cai, W.; Lu, F.; Zhang, J.; Yang, Y.; Ma, N.; Liu, Y. *Chem. Mater.* **2005**, *17*, 1548–1552. (b) Liu, G.; Chen, Z. G.; Dong, C. L.; Zhao, Y. N.; Li, F.; Lu, G. Q.; Cheng, H. M. *J. Phys. Chem. B* **2006**, *110*, 20823.

[17] (a) Zhang, K. L.; Liu, C. M.; Huang, F. Q.; Zheng, C.; Wang, W. D. *Appl. Catal., B* **2006**, *68*, 125–129. (b) Lin, X. P.; Huang, T.; Huang, F. Q.; Wang, W. D.; Shi, J. L. *J. Phys. Chem. B* **2006**, *110*, 24629–24634.

[18] Asahi, R.; Taga, Y.; Mannstadt, W.; Freeman, A. J. *Phys. Rev. B* **2000**, *61*, 7459–7465.

[19] Nakano, Y.; Morikawa, T.; Ohwaki, T.; Taga, Y. *Appl. Phys. Lett.* **2005**, *86*, 132104.

[20] Spitler, M. T.; Calvin, M. *J. Chem. Phys.* **1977**, *66*, 4294–4305.

[21] (a) Clark, W. D. K.; Sutin, N. *J. Am. Chem. Soc.* **1977**, *99*, 4676–4682. (b) Nazeeruddin, M. K.; Kay, A.; Rodicio, I.; Humphry-Baker, R.; Müller, Liska, P.; Vlachopoulos, N.; Grätzel, M. *J. Am. Chem. Soc.* **1993**, *115*, 6382–6390.

[22] (a) Kisch, H.; Zang, L.; Lange, C.; Maier, W. F.; Antonius, C.; Meissner, D. *Angew. Chem., Int. Ed.* **1998**, *37*, 3034–3036. (b) Zhang, L.; Macyk, W.; Lange, C.; Maier, W. F.; Antonius, C.; Meissner, D.; Kish, H. *Chem.–Eur. J.* **2000**, *6*, 379–384.

[23] Cho, Y.; Choi, W.; Lee, C.-H.; Hyeon, T.; Lee, H.-I. *Environ. Sci. Tech.* **2001**, *35*, 966–970.

[24] Desilvestro, J.; Grätzel, M.; Kavan, L.; Moser, J. *J. Am. Chem. Soc.* **1985**, *107*, 2988–2990.

[25] Jain, P. K.; Huang, X.; El-Sayed, I. H.; El-Sayed, M. A. *Acc. Chem. Res.* **2008**, *41*, 1578–1586.

[26] Hao, Q.; Juluri, B. K.; Zheng, Y. B.; Wang, B.; Chiang, I-K.; Jensen, L.; Crespi, V.; Eklund, P. C.; Huang, T. J. *J. Phys. Chem. C.* **2010**, *114*, 18059–18066.

[27] Tian, Y.; Tatsuma, T. *Chem. Commun.* **2004**, 1810–1811.

[28] Tian, Y.; Tatsuma, T. *J. Am. Chem. Soc.* **2005**, *127*, 7632–7637.

[29] González, V. R.; Zanella, R.; Angel, G.; Gómez, R. *J. Mole. Catal. A: Chem.* **2008**, *281*, 93–98.

[30] Kowalska, E.; Abe, R.; Ohtani, B. *Chem. Commun.* **2009**, 241–243.

[31] Silva, C. G.; Juárez, R.; Marino, T.; Molinari, R.; García, H. *J. Am. Chem. Soc.* **2011**, *133*, 595–602.

[32] Zhang, Z.; Yates, J. T., Jr.; *Chem. Rev.* **2012**, *112*, 5520–5551.

[33] (a) Schottky, W. *Eur. Phys. J. A.* **1939**, *113*, 367–414. (b) Bardeen, J. *Phys. Rev.* **1947**, *71*, 717–727.

[34] Linic, S.; Christopher, P.; Ingram, D. B. *Nat. Mater.* **2011**, *10*, 911–921.

[35] Gong, X.-Q.; Selloni, A.; Dulub, O.; Jacobson, P.; Diebold, U. *J. Am. Chem. Soc.* **2008**, *130*, 370–381.

[36] (a) Tauster, S. J.; Fung, S. C.; Garten, R. L. *J. Am. Chem. Soc.* **1978**, *100*, 170–175. (b) Tauster, S. J.; Fung, S. C.; Baker, R. T. K.; Horsley, J. A. *Science*, **1981**, *211*, 1121–1125.

Chapter I

Hot Electron Injection on Pt Nanoparticles Supported on TiO$_2$

1. Introduction

Nitrosobenzene is a versatile intermediate for organic synthesis in several reactions such as aldol,[1] ene,[2] and Diels–Alder reactions.[3] Traditionally, this compound has been synthesized by oxidation of aniline with excess amount of unstable peracids such as peracetic acid and perbenzoic acid.[4–6] Catalytic oxidation processes with a phosphotungstate or phosphomolybdate catalyst have also been proposed;[7–9] however, all of these methods require expensive hydrogen peroxide as an oxidant. Aerobic oxidation of aniline with molecular oxygen (O$_2$) as an oxidant is therefore an ideal process from the view point of green chemistry (eq. 1). Some catalytic systems have been proposed;[10–12] however, all of these reactions require high temperature (>373 K). The high temperature systems inevitably promote subsequent condensation of aniline and the formed nitrosobenzene,[13,14] producing azobenzene as a main product (eq. 2). A new catalytic system that promotes aerobic oxidation of aniline at low temperature is necessary for selective production of nitrosobenzene.

$$\text{(1)}$$

$$\text{(2)}$$
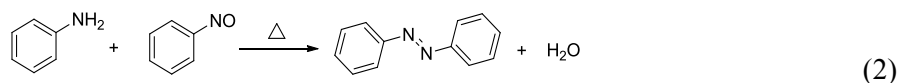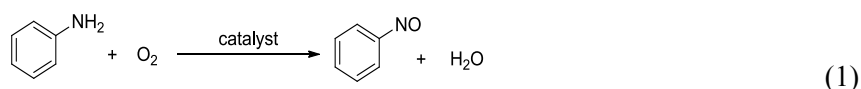
Photocatalytic oxidation on semiconductor materials with O$_2$ is one of the possible methods that can serve this purpose because the reaction proceeds under photoirradiation even at room temperature.[15–18] There have been three reports of photocatalytic oxidation of aniline with O$_2$.[19–21] These systems employed a titanium dioxide (TiO$_2$), zinc oxide (ZnO), or zirconium dioxide (ZrO$_2$) semiconductor catalyst under UV irradiation. All of these systems, however, produce azobenzene as a major product, where nitrosobenzene is scarcely detected during the reactions.

Earlier, we reported that gold (Au)[22,23] or platinum (Pt)[24.25] nanoparticles loaded on semiconductor titanium dioxide (TiO$_2$) successfully promote aerobic oxidation of alcohols to aldehydes under visible light irradiation (λ >450 nm). **Figure 1-1** summarizes the mechanism for photoreaction occurring in the Pt/TiO$_2$ system. Visible light absorption of Pt particles promotes an interband transition of 5d band electrons (e$^-$). The e$^-$ overcome the Schottky barrier (ϕ_B) created at the Pt–TiO$_2$ heterojunction[26] and are transferred to the TiO$_2$ conduction band.[27] The positive charges formed on the surface of Pt particles oxidize the substrate,

while the e⁻ on TiO_2 are consumed by the reduction of O_2. This catalytic cycle successfully promotes aerobic oxidation of alcohols even at room temperature.
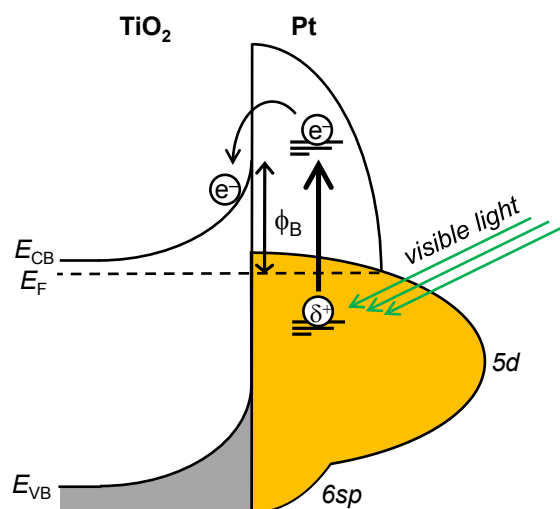
Figure 1-1. Proposed Mechanism for Electron Transfer from Photoactivated Pt Particles to TiO_2. Where E_{CB}, E_{VB}, E_F, and ϕ_B denote the conduction band potential, valence band potential, Fermi level, and the height of Schottky barrier, respectively.

Here, Pt particles supported on TiO_2 (Pt/TiO_2 catalysts) were used for photocatalytic oxidation of aniline with O_2 under visible light irradiation (> 450 nm). The author found that Pt particles supported on Degussa P25 TiO_2, a mixture of anatase and rutile particles,[28–30] promote efficient nitrosobenzene production. X-ray photoelectron spectroscopy (XPS) and diffuse-reflectance infrared Fourier transform (DRIFT) analysis revealed that the high activity of the Pt/P25 catalyst is due to the high electron density of the Pt particles. They behave as Lewis base sites for reductive deprotonation of aniline, thus promoting efficient aniline oxidation. The Pt/P25 catalyst, when photoirradiated at a low temperature (~283 K), produces nitrosobenzene with a very high selectivity (90 %).

2. Experimental Section

2-1. Materials

All reagents used were purchased from Wako, Tokyo Kasei, and Sigma–Aldrich and used without further purification. Water was purified by the Milli-Q system. Anatase TiO_2 (JRC–TIO–1), P25 (JRC–TIO–4), and rutile TiO_2 (JRC–TIO–6; 15 nm; 104 m² g⁻¹) were kindly supplied from the Catalyst Society of Japan.

2-2. Synthesis of catalysts

2-2-1. Pt$_x$/TiO$_2$

The catalysts with different Pt loadings [x (wt %) = 0.5, 1, 2, 3, or 4] were prepared as follows: TiO$_2$ (1 g) was added to water (40 mL) containing H$_2$PtCl$_6$·6H$_2$O (13.3, 26.8, 54.2, 82.1, or 110.6 mg). The solvents were removed by evaporation at 353 K with vigorous stirring for 12 h. The obtained powders were clacined under air flow and then reduced under H$_2$ flow at the identical temperature. Unless otherwise noted, these treatments were carried out at 673 K. The heating rate was 2 K min^{-1} and the holding time at the designated temperature was 2 h, respectively.

2-2-2. M$_2$/P25

The catalysts with 2 wt% metal particles (M = Ag, Pd) were prepared as follows: P25 TiO$_2$ (1 g) was added to water (40 mL) containing AgNO$_3$ (32.1 mg) or PdNO$_3$ (44.2 mg). The solvents were removed by evaporation with vigorous stirring at 353 K for 12 h. The resulting powders were calcined at 673 K for 2 h under air flow and reduced at 673 K for 2 h under H$_2$ flow. Au$_2$/P25 catalyst was prepared by deposition-precipitation method.[22] P25 TiO$_2$ (1 g) was added to water (50 mL) containing HAuCl$_4$·4H$_2$O (45.8 mg). The pH of solution was adjusted to about 7 with 1 mM NaOH, and the solution was stirred at 353 K for 3 h. The particles were recovered by centrifugation, washed with water, and dried at 353 K for 12 h. The powder were calcined under air flow, where the heating rate was 2 K min^{-1} and the holding time at 673 K was 2 h, respectively.

2-3. Photoreaction

The catalyst (20 mg) was added to toluene (5 mL) containing aniline within a Pyrex glass tube (φ 12 mm; capacity, 20 mL). The tube was sealed with a rubber septum cap. The catalyst was dispersed by ultrasonication for 5 min, and O$_2$ was bubbled through the solution for 5 min. The tube was immersed in a temperature-controlled water bath (298 ± 0.5 K). The tube was photoirradiated with magnetic stirring using a 2 kW Xe lamp (Ushio Inc.).[31] The light was filtered through a glass filter (CS3-72; Kopp Glass Inc.) to give λ >450 nm light, where the light intensity at 450–800 nm was 16.8 mW cm^{-2}. After the reaction, the catalyst was recovered by centrifugation. The liquid-phase products were analyzed by GC and free induction decay (Shimadzu, GC-1700).

2-4. ESR Measurement

The spectra were recorded at the X-band using a Bruker EMX–10/12 spectrimeter with a 100 kHz magnetic field modulation at a microwave power level of 10.0 mW, where microwave power saturation of the signal does not occur.[32] The magnetic field was calibrated with 1,1′-diphenyl-2-picryl-hydrazyl (DPPH). The catalyst (20 mg) was placed in a quartz ESR tube and the tube evacuated at 423 K for 3 h. After the tube had been cooled to room temperature, O_2 (20 Torr) was introduced into the tube and the tube kept 3 h at 298 K. The tube was photoirradiated for 3 h at 298 K. The tube was then evacuated for 10 min to remove the excess of O_2 and subjected to analysis at 77 K.

2-5. DRIFT Analysis

The spectra were measured on a FTIR 610 system equipped with a DR–600B *in situ* cell (Jasco Corp.).[33] The catalyst (50 mg) was placed in a DR cell and evacuated (6.8×10^{-3} Torr) at 423 K for 3 h. Aniline (7.5 $\times 10^{-2}$ Torr) was introduced to the cell at 298 K, and measurement was started.

2-6. Other Analysis

TEM observations were made using a JEOL Tecnai G2 20ST analytical electron microscope operated at 200 kV.[34] XPS analysis was performed using a JEOL JPS9000MX spectrometer with Mg Kα radiation as the energy source. Diffuse reflectance UV-vis spectra were measured on an UV-vis spectrometer (Jasco Corp.; V-550 with Integrated Sphere Apparatus ISV-469) with $BaSO_4$ as a reference. IR spectra were recorded at room temperature using a FTIR-610 spectrometer (Jasco Corp.) with a liquid sample cell with a CaF_2 window.
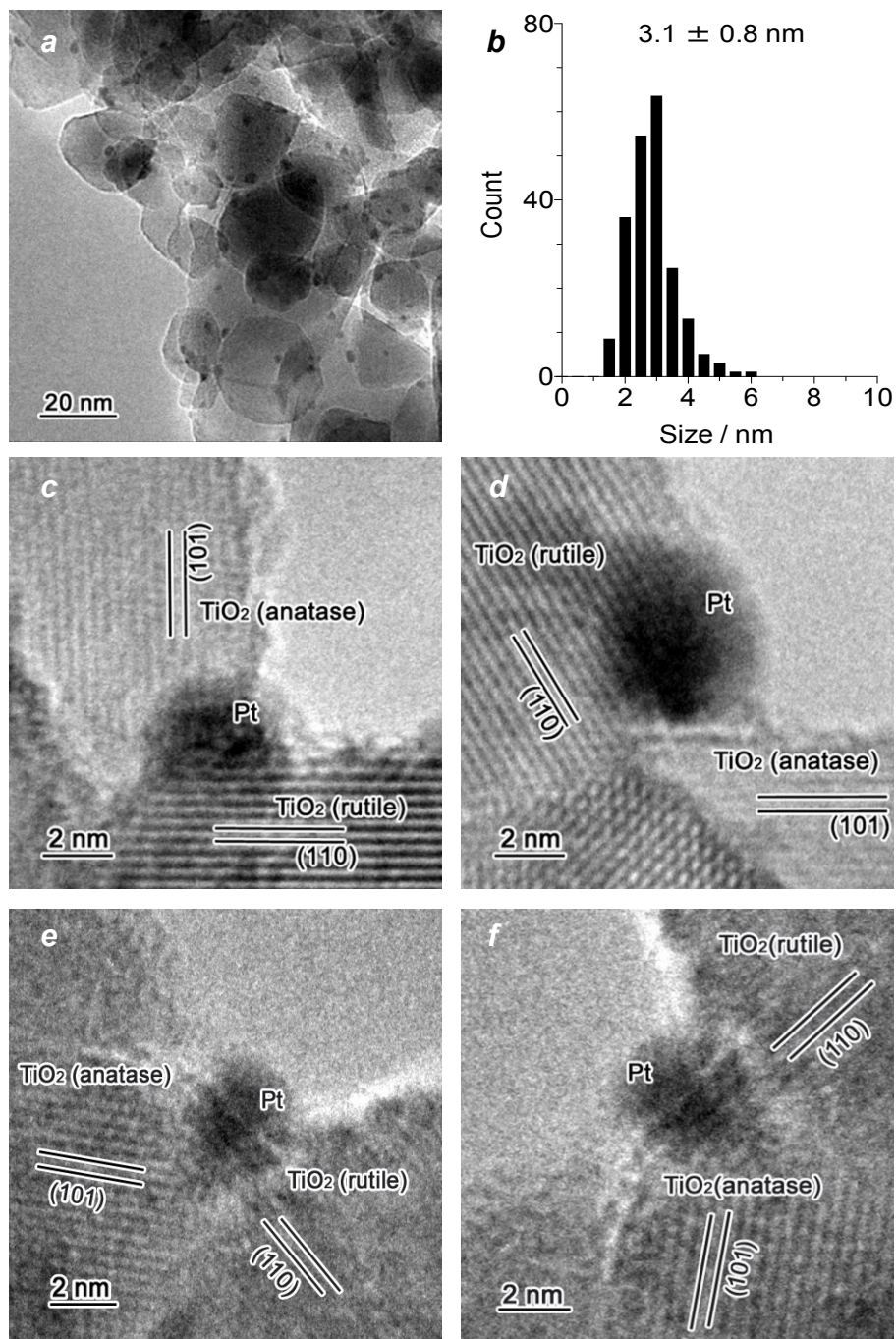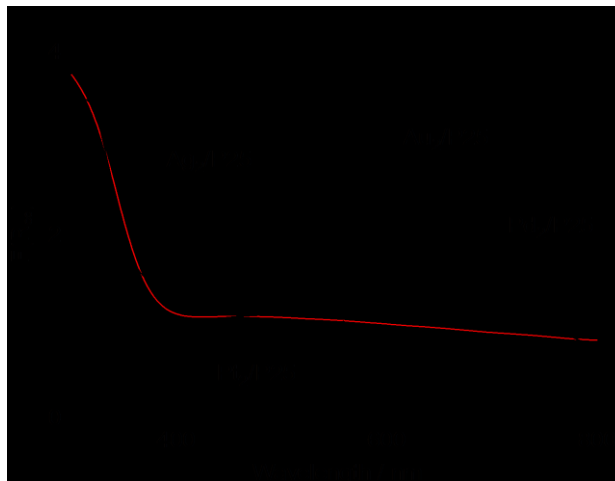
Figure 1-2. (a) Typical TEM image of Pt_2/P25 catalyst and (b) the size distribution of metal particles. (c–f) High-resolution TEM images of the catalyst. Anatase (101) and rutile (110) phases were identified by their lattice spacings (0.352 and 0.325 nm, respectively).
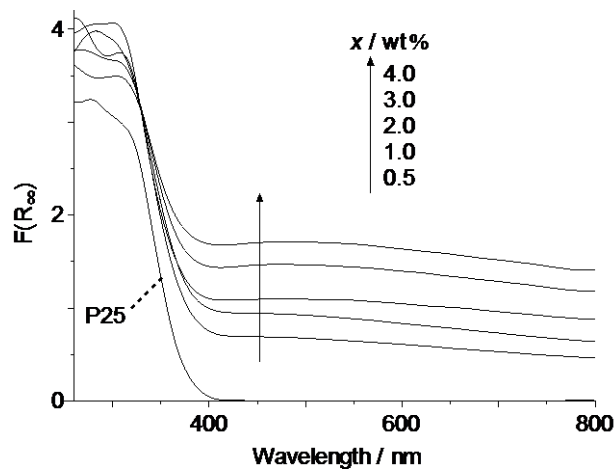
Figure 1-3. Diffuse-reflectance UV-vis spectra of the supports and catalysts.
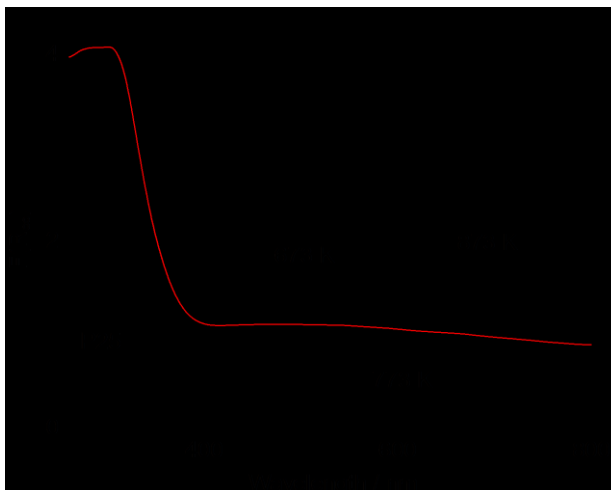
M/P25 (M = Au, Ag, Pd, Pt)

Pt$_x$/P25 (x = 0.5, 1, 2, 3, 4 wt %)

Pt$_2$/P25 prepared at different temperatures (673, 773, 873 K)

Figure 1-4. Diffuse-reflectance UV-vis spectra of catalysts.

3. Results and Discussion

3-1. Preparation and properties of catalyst

The Pt/P25 catalyst was prepared by impregnation of Pt precursors followed by reduction with H$_2$.[36,37] P25 TiO$_2$ particles (particle size, 24 nm; BET surface area, 57 m^2 g^{-1}; anatase/rutile ratio, 82/18) were added to water containing H$_2$PtCl$_6$, and the solvents were removed by evaporation with vigorous stirring. The resultant was calcined in air and reduced under a H$_2$ flow at 673 K, affording Pt$_x$/P25 as brown powders, where x denotes the amount of Pt loaded [x (weight percent) = Pt / (Pt + TiO$_2$) × 100]. **Figure 1-2a** shows a typical transmission electron microscopy (TEM) image of the Pt$_2$/P25 catalyst. Pt nanoparticles are highly dispersed on the support. The average diameter of the Pt particles was determined to be 3.1 nm (**Figure 1-2b**). As shown in **Figure 1-3**, the diffuse-reflectance UV-vis spectrum of Pt$_2$/P25 exhibits a broad absorption band at λ >400 nm, assigned to the interband transition of Pt particles.[38]

3-2. Photocatalytic activity

We performed photocatalytic oxidation of aniline by stirring a toluene solution (5 mL) containing aniline (1 mmol) and catalyst (20 mg) with O$_2$ (1 atm) under photoirradiation at λ > 450 nm by a Xe lamp. The temperature of the solution was kept rigorously at 298 ± 0.5 K by a digitally controlled water bath. **Figure 1-5** summarizes the amount of products formed by a 12 h photoreaction. It must be noted that gas chromatography (GC) analysis of the resulting solution for all of the systems detected only nitrosobenzene and azobenzene. With bare P25 TiO$_2$, almost no reaction occurs. In contrast, the Pt$_2$/P25 catalyst produces nitrosobenzene (9.7 μmol) with a minor amount of azobenzene (2.5 μmol). Although Pt nanoparticles exhibit

catalytic activity for aerobic oxidation even under the dark condition,[39,40] the $Pt_2/P25$ catalyst, when reacted under the dark condition, give only a minor amount of products. An increase in temperature enhances the reaction even under the dark condition, but azobenzene is produced as a main product because of the condensation of aniline with the formed nitrosobenzene enhanced at higher temperature.[13] These data suggest that visible light irradiation of the Pt/P25 catalyst at room temperature successfully promotes aerobic oxidation of aniline and selectively produces nitrosobenzene.
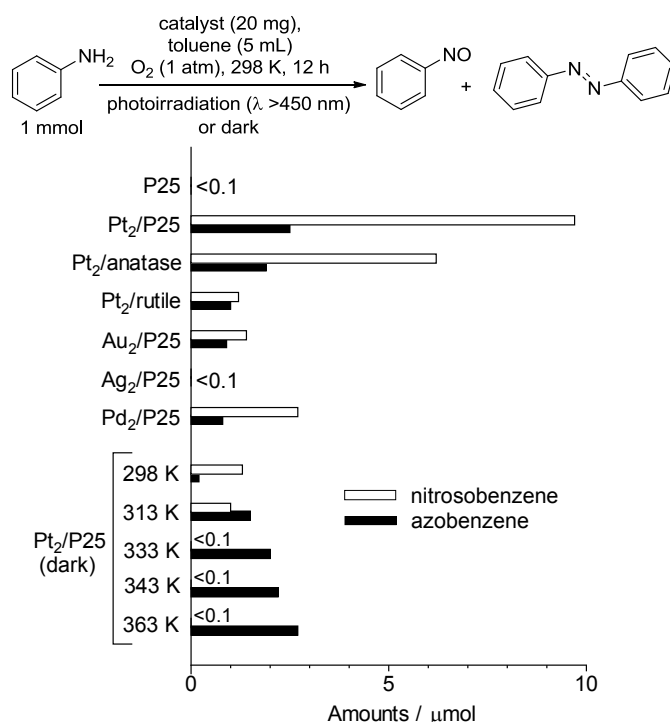

Figure 1-5. Amounts of (white) nitrosobenzene and (black) azobenzene produced by aerobic oxidation of aniline with respective catalysts in the dark or under visible light irradiation (λ >450 nm; light intensity at 450–800 nm, 16.8 mW cm^{-2}). Diffuse-reflectance UV-vis spectra for Au, Pd, and Ag catalysts are summarized in **Figure 1-3**.

To clarify the effect of TiO$_2$ support, Pt particles were loaded on anatase TiO$_2$ (Japan Reference Catalyst JRC–TIO–1; average particle size, 21.1 nm; BET surface area, 81 m^2 g^{-1}) and rutile TiO$_2$ (Japan Reference Catalyst JRC–TIO–6; 15 nm; 104 m^2 g^{-1}). As shown in **Figure 1-6**, the sizes of Pt particles on these supports were determined to be 3.4 and 2.9 nm, respectively, both of which are similar to those of $Pt_2/P25$ [3.1 nm (**Figure 1-2b**)]. As shown in **Figure 1-5**, both Pt_2/anatase and Pt_2/rutile catalysts, however, show photocatalytic activity lower than that of $Pt_2/P25$. In addition, as shown **Figure 1-7**, Pt particles supported on other anatase and rutile TiO$_2$ particles with different particle sizes and surface areas also exhibit catalytic activity lower than that of $Pt_2/P25$. These data suggest that P25 TiO$_2$ is the support exhibiting the best

20

photocatalytic performance. It is also noted that, as shown in **Figure 1-5**, Au, Ag, and Pd particles, when loaded on P25, exhibit activity much lower than that of Pt_2/P25, although these metal particles are also activated by visible light absorption via the intraband (Au[41,42] and Ag[43,44]) or interband (Pd[45,46]) transitions. These findings suggest that Pt particles loaded on P25 TiO_2 promote efficient aerobic oxidation of aniline under visible light irradiation. In addition, as shown in **Figure 1-8**, Pt_2/P25 maintains its activity even after prolonged photoirradiation (~48 h), suggesting that the catalyst scarcely loses its activity during the photoreaction.
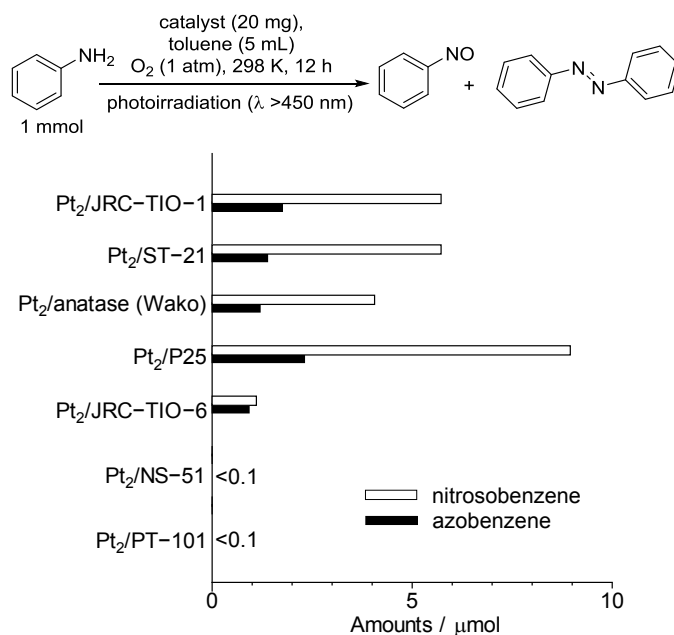
Pt_2/anatase
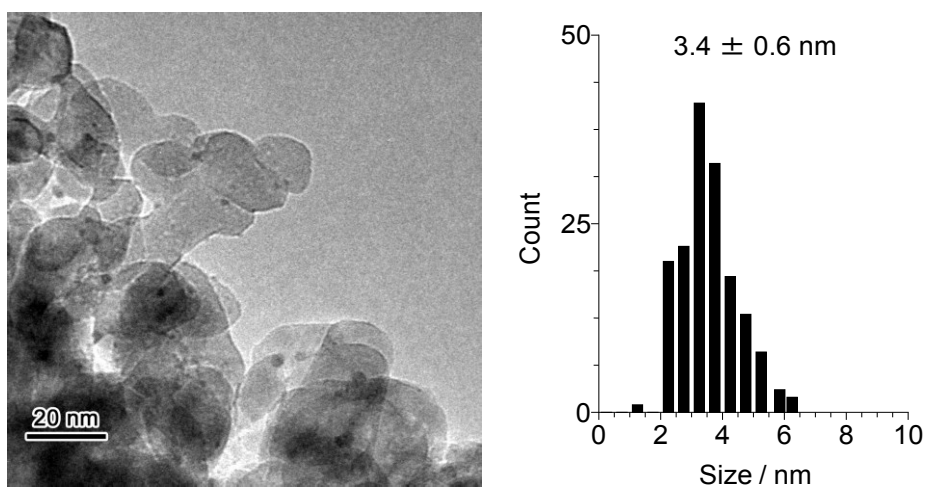
Pt_2/rutile
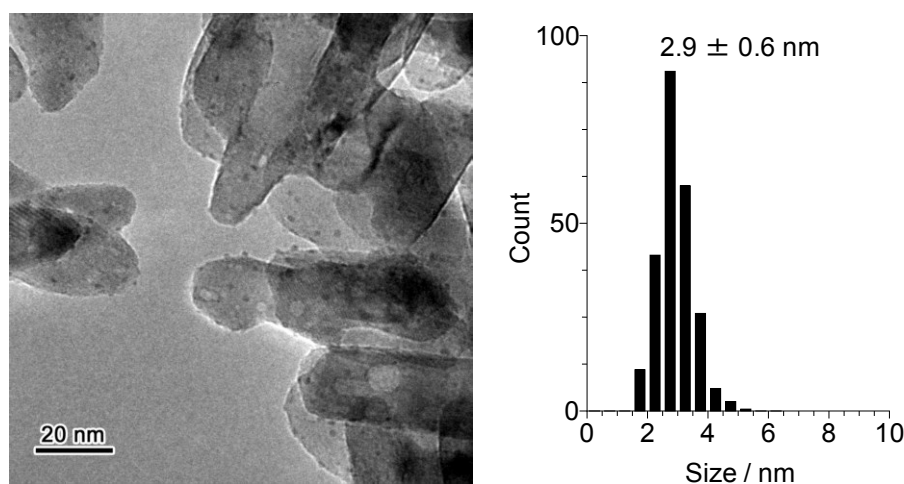
**Figure 1-6.** Typical TEM images of catalysts and size distribution of Pt particles.

Properties of the supports used

Catalyst	Supplier	crystalline phase	particle size / nm [a]	S_{BET} / m^2 g^{-1} [b]
JRC–TIO–1	Catalysis Society of Japan	anatase	21	81
ST–21	Ishihara Sangyo Co., Ltd.	anatase	25	69
anatase (Wako)	Wako	anatase	29	59
P25	Catalysis Society of Japan	anatase/rutile (83/17)	24	57
JRC–TIO–6	Catalysis Society of Japan	rutile	15	104
NS–51	Toho Titanium Co., Ltd.	rutile	220	7
PT–101	Ishihara Sangyo Co., Ltd.	rutile	71	25

[a] Hydrodynamic diameter of particles determined by a Horiba LB–500 dynamic light–scattering particle size analyzer. [b] BET surface area determined by N_2 adsorption/desorption measurements at 77 K using an AUTOSORB–1–C/TCD analyzer (Yuasa Ionics Co., Ltd.).

Figure 1-7. Amounts of (white) nitrosobenzene and (black) azobenzene produced by aerobic oxidation of aniline on anatase or rutile TiO$_2$ loaded with Pt particles under visible light irradiation (λ >450 nm). The reaction conditions are identical to those in **Figure 1-5**.
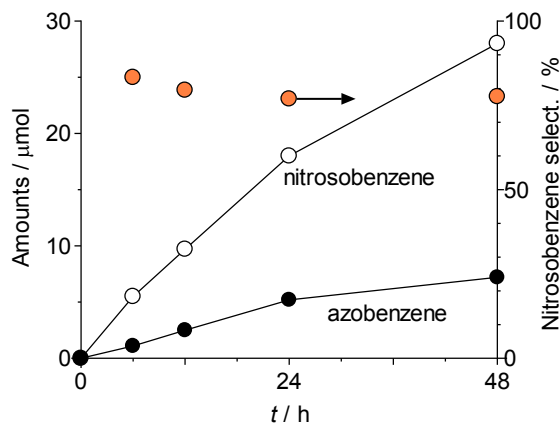
Figure 1-8. Time-dependent change in the amount of products and the nitrosobenzene selectivity during photocatalytic reaction of aniline with Pt_2/P25. The reaction conditions are identical to those in **Figure 1-5**.

3-3. Transfer of an Electron from Photoactivated Pt Particles to TiO$_2$

As shown in **Figure 1-1**, in the Pt/P25 system, photoactivated Pt particles transfer their e^- to TiO$_2$, and the e^- reduces O$_2$ on its surface. This is confirmed by electron spin resonance (ESR) analysis of the catalysts measured at 77 after treatment of the sample with O$_2$ at 298 K under visible light irradiation ($\lambda > 450$ nm; 3 h) according to the procedure described previously ($\lambda > 450$ nm; 1 h).[24] As shown in **Figure 1-9a** (black), the Pt$_2$/P25 catalyst treated with O$_2$ in the dark shows almost no signal. Visible light irradiation of this sample (blue), however, creates distinctive signals assigned to a superoxide-type oxygen anion (O$_2^-$; $g_{xx} = 2.002$, $g_{yy} = 2.009$, $g_{zz} = 2.028$) stabilized on the TiO$_2$ surface.[47] This suggests that photoactivated Pt particles indeed transfer e^- reduces O$_2$ on its surface. As shown in spectra b and c of **Figure 1-9** (blue), photoirradiation of Pt$_2$/anatase creates much stronger O$_2^-$ signals, whereas Pt$_2$/rutile shows very weak signals, as also observed in our previous work.[24] The weak O$_2^-$ signals on the Pt/rutile catalyst exist because, as reported,[24,48] the transfer of an electron from photoactivated Pt particles to rutile TiO$_2$ is difficult and the rutile surface is inactive for O$_2$ reduction. The signal intensity of Pt/P25 is weaker than that of Pt/anatase because the Pt particles on P25 TiO$_2$ are located at the interface between anatase and rutile particles. This is confirmed by a high-resolution TEM image of the Pt/P25 catalyst. As shown in **Figure 1-2c-f**, Pt particles are indeed located at the anatase–rutile interface and show well-defined contact surfaces consisting of Pt/anatase/rutile phases. As a result of this, the smooth transfer of e^- from photoactivated Pt particles to anatase is suppressed, resulting in inefficient O$_2$ reduction.[49–52] The obtained ESR results suggest that the efficiency for photoinduced charge separation on Pt/P25 is lower than that on Pt/anatase. However, as shown in **Figure 1-5**, the photocatalytic activity of Pt/P25 is much higher.

23
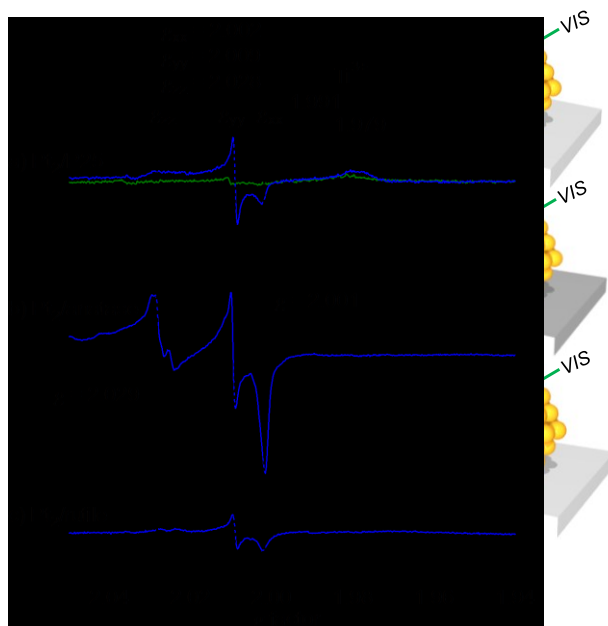
Figure 1-9. ESR spectra of respective catalysts measured at 77 K. The catalysts were treated at 298 K with 20 Torr of O_2 (black) in the dark or (blue) under visible light irradiation for 3 h. After evacuation, the samples were measured at 77 K. The green spectrum in panel a was obtained as follows. Aniline (7.5×10^{-2} Torr) was added at 298 K to the sample treated with O_2 under visible light irradiation and left for 10 min. After evacuation, the sample was measured at 77 K. The signals observed for the Pt/anatase sample (b) under the dark condition ($g = 2.029$ and 2.001) are assigned to O^- formed via a dissociative adsorption of O_2 onto the oxygen vacancy sites of the anatase TiO_2 surface, which was also observed for bare anatase TiO_2.[24] The broad $g = 1.980$ signal (spectrum a) is assigned to the Ti^{3+} species formed on rutile TiO_2.[50]
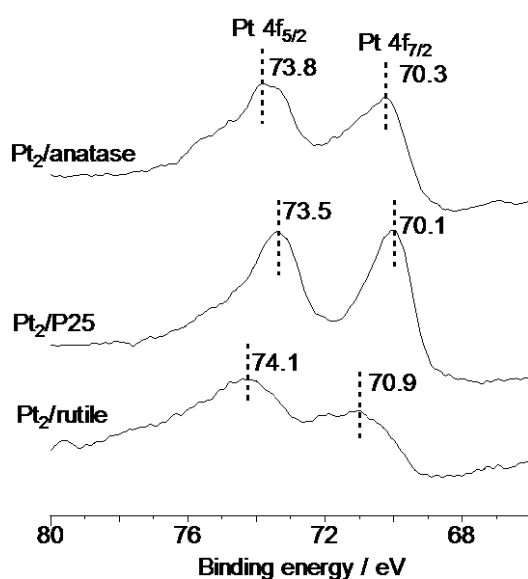

Figure 1-10. XPS chart (Pt 4f level) for catalysts. The data for other anatase and rutile catalysts are summarized in **Figure 1-11**.

24

3-4. High Electron Density of Pt Particles on Pt/P25

During the oxidation of aniline, deprotonation of aniline is the rate-determining step. The aniline formed via the deprotonation by the Lewis base is oxidized very efficiently.[53] As shown in **Figure 1-5**, photoreaction of aniline with Pt_2/Panatase catalyst produces 6.2 μmol of nitrosobenzene with 1.9 μmol of azobenzene. Addition of triethylamine (1 mmol), which behave as a base or a sacrificantly enhances the reaction (producing 34 μmol of nitrosobenzene with 2.0 μmol of azobenzene). In contrast, addition of 2-propanol (1 mmol), which does not behave as a base but acts as a sacrificial reagent, scarcely enhances the reaction (9.5 μmol of nitrosobenzene with 0.4 μmol of azobenzene). This clearly suggests that deprotonation of aniline by the base is indeed the rate-determining step for aniline photooxidation.

In the Pt/P25 system, Pt nanoparticles located at the interface between anatase and rutile phases possess high electron density and behave as the Lewis base site for reductive deprotonation of aniline. This thus promotes efficient photooxidation of aniline. The high electron density of Pt particles on P25 TiO_2 is confirmed by XPS analysis. As shown in **Figure 1-10**, the XPS chart of Pt/P25 shows Pt 4f 5/2 and 7/2 peaks at 73.5 and 70.1 eV, respectively. In contrast, both Pt/anatase and Pt/rutile catalysts exhibit these peaks at higher binding energies. This suggests that Pt particles on P25 TiO_2 indeed possess higher electron density.
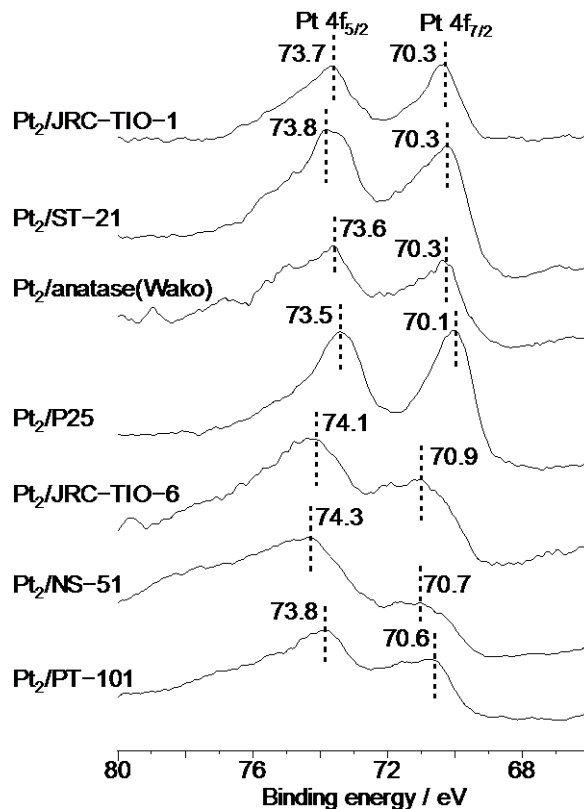
**Figure 1-11.** XPS results for respective catalysts.

The high electron density of Pt particles on P25 TiO_2 is due to the strong Pt–support interaction. As shown in **Figure 1-2b** and **Figure 1-6**, Pt_2/P25, Pt_2/anatase, and $Pt_{/2}$/rutile catalysts contain Pt particles with similar diameters (3.1, 3.4, and 2.9 nm, respectively), suggesting that the size of Pt peaks of Pt/P25 at lower binding energies (**Figure 1-10**) therefore exist because a larger number of electrons on P25 TiO_2 are transferred to Pt at the interface. The position of Pt peaks usually depends on the Fermi level of the semiconductor; a semiconductor with a more negative Fermi level transfers its electrons to Pt more efficiently and shows Pt XPS peaks at lower binding energies.[54,55] Rutile TiO_2 has a Fermi level more negative than that of anatase.[56] However, as shown in **Figure 1-10** and **Figure 1-11**, the Pt peaks for Pt/rutile catalysts appear at a binding energy higher than that of the Pt/anatase catalyst because the anatase surface is strongly associated with Pt particles, as supported by DFT calculations,[57] and transfers the electrons to Pt more efficiently.[57] In contrast, Pt/P25 shows Pt peaks at a binding energy lower than that of Pt/anatase (**Figure 1-10**). As reported, [22,59] metal nanoparticles such as Au are highly stabilized when they are located at the anatase–rutile interface. The strong Pt–support interaction of Pt/P25 therefore probably enhances the transfer of the electron from the support to Pt. This thus increases the electron density of Pt nanoparticles.

## 3-5. Lewis Base Activity of Pt Particles on Pt/P25 Catalyst

The deprotonation of aniline promoted by Pt particles on the P25 support is confirmed by DRIFT analysis. **Figure 1-12** shows the DRIFT apectra of aniline adsorbed onto the respective catalysts in the gas phase at 298 K. As shown in Figure 11a, the aniline adsorbed onto bare P25 shows two adsorption bands at 3292 and 3245 cm^{-1}, which are assigned to the antisymmetric stretching vibration (v_{anti}) and the symmetric stretching vibration (v_{sym}) of the $-NH_2$ group, respectively.[60] As shown in spectra c and d of **Figure 1-12**, aniline when adsorbed onto the Pt/anatase and Pt/rutile catalysts also shows similar signals. However, in the case of Pt/P25 (**Figure 1-12b**), a new band appears at a higher wavenumber (3323 cm^{-1}). This indicates that some of the aniline molecules adsorbed onto the Pt particles on P25 are transformed to the species with a stronger (shorter) N−H bond.[61] **Figure 1-13** shows the IR spectra of aniline measured in a CCl_4 solution. Distinctive v_{anti} and v_{sym} bands for $-NH_2$ groups appear at 3478 and 3395 cm^{-1}, respectively. In contrast, addition of 30 equiv of triethylamine to this solution creates a new band at a higher wavenumber (3511 cm^{-1}), which is assigned to the N−H vibrational band strengthened via deprotonation by the base.[62] The obtained band is similar to that obtained on the Pt/P25 catalyst (**Figure 1-12b**). These data clearly suggest that Pt particles on the P25 support indeed behave as Lewis base sites and promote reductive deprotonation of aniline.

On the basis of the findings described above, the mechanism for aerobic oxidation of aniline on the

Pt/P25 catalyst is explained in **Figure 1-14**. The reaction is initiated by deprotonation of aniline on the Lewis base site on Pt nanoparticles (a), producing anilino anion. Visible light absorption of Pt particles transfers their e^- to anatase (b). The e^- reduces O_2 and produces a superoxide anion (O_2^-) on the anatase surface (c). The O_2^- attracts the removed H atom of aniline and produces a hydroperoxide species (d), as is observed in related systems for oxidation of alcohols.[63,64] As shown in **Figure 1-12a** (blue), the ESR spectrum of Pt/P25 obtained by visible light irradiation with O_2 shows distinctive signals assigned to O_2^-. However, as shown by the green spectrum, addition of aniline to this sample completely quenches the O_2^- signal. This suggests that, as shown in **Figure 1-14** (c $\rightarrow$ d), the H atom removed by deprotonation of aniline on the Pt particles reacts with O_2^- and produces a hydroperoxide species. Subsequent reaction between the anilino anion and hydroperoxide species[63,64] gives rise to nitrosobenzene and water and completes the photocatalytic cycle.
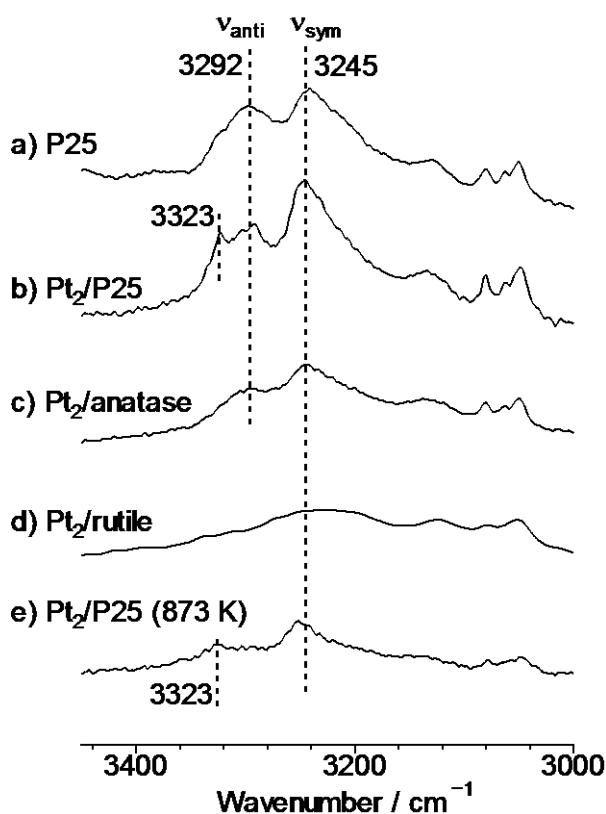
Figure 1-12. DRIFT spectra of aniline adsorbed on (a) bare P25, (b) Pt$_2$/P25, (c) Pt$_2$/anatase, (d) Pt$_2$/rutile, and (e) Pt$_2$/P25 prepared at 873 K, in gas phase at 298 K.
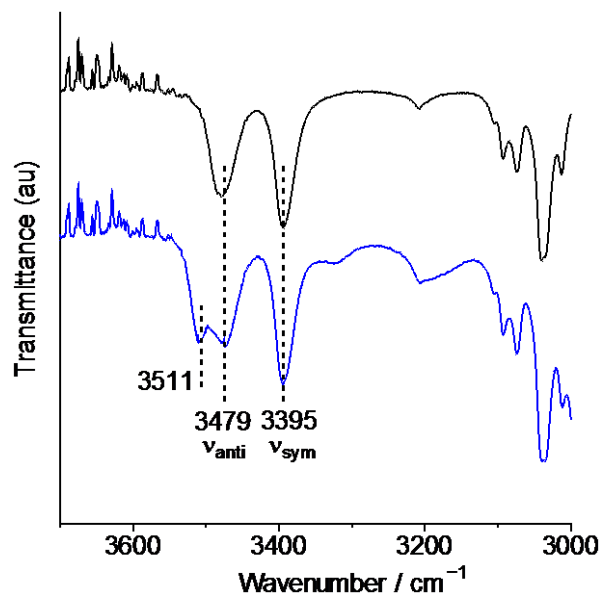
Figure 1-13. IR spectra of aniline (20 mM) measured in the (black) absence and (blue) presence of triethylamine (30 equiv) in CCl_4.
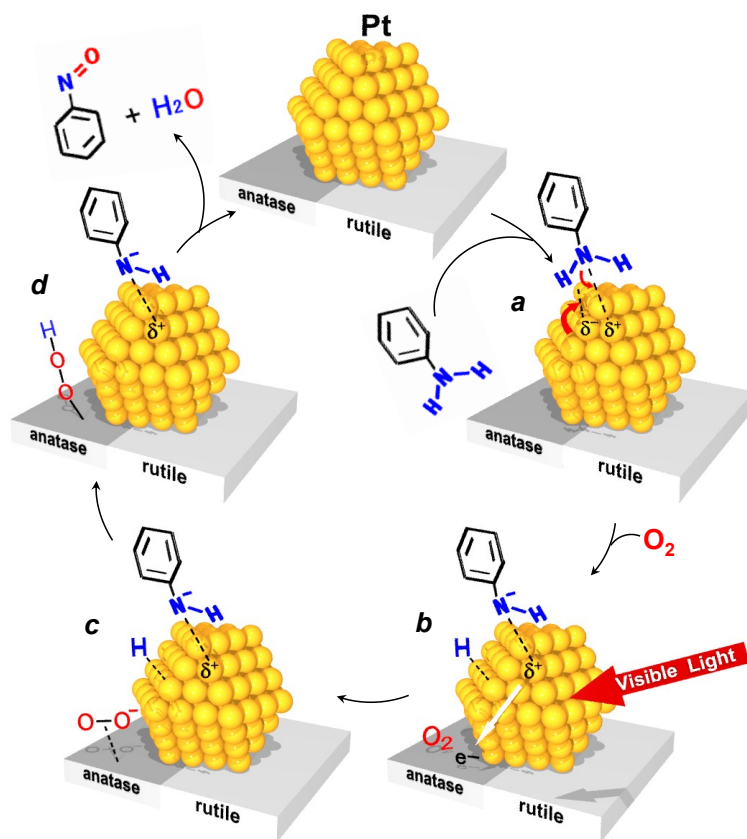

Figure 1-14. Proposed Mechanism for Aerobic Oxidation of Aniline on the Pt/P25 Catalyst under Visible Light Irradiation
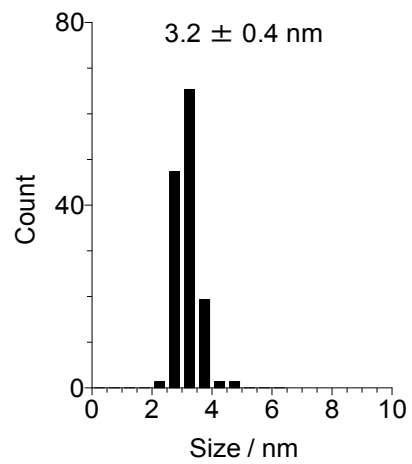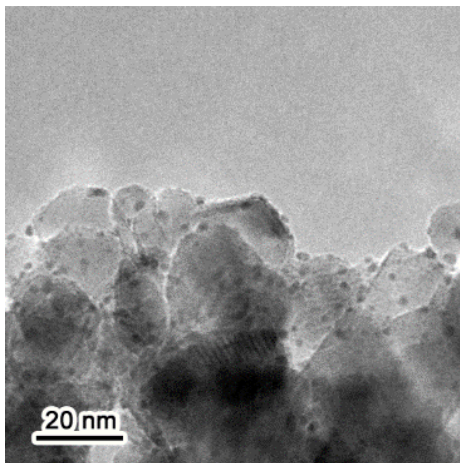
3-6. Effects of the Amount of Pt and Particle Size

The catalytic activity for aerobic oxidation of aniline on Pt/P25 depends on the amount of Pt loaded. We prepared Pt_x/P25 catalysts with different Pt loadings [x (weight percent) = Pt/(Pt + P25) × 100 = 0.5, 1, 3, and 4]. As shown in **Figure 1-15**, the sizes of Pt particles on the $Pt_{0.5}$/P25 and Pt_4/P25 catalysts were determined by TEM observations to be 3.0 and 3.2 nm, respectively, which are similar to those on Pt_2/P25 (3.1 nm). This indicates that the amount of Pt loaded scarcely affects the Pt particle sizes. **Figure 1-16a** (bars) summarizes the amounts of nitrosobenzene and azobenzene produced by a 12 h photoreaction with respective catalysts. As shown by the orange symbols, the nitrosobenzene selectivities for the catalysts are similar (~80%). The amount of nitrosobenzene formed, however, depends on the amount of Pt loaded; the activity increases with Pt loadings (0.5−2 wt %) because the increase in the number of surface Pt atoms promotes efficient transfer of e^- to anatase and deprotonation of aniline. The activity, however, decreases with >2 wt % Pt loadings. As reported previously,[65] the increase in the amount of Pt loaded onto the semiconductor surface leads to an increase in the Schottky barrier height (ϕ_B), because of the decrease in the Fermi level of the semiconductor. The increased ϕ_B probably suppresses the transfer of e^- from photoactivated Pt particles to anatase, resulting in decreased photocatalytic activity.

The Pt particle size also affects catalytic activity. The Pt_2/P25 catalysts were prepared at different calcination and reduction temperatures (673, 773, and 873 K) while maintaining a 2 wt % Pt loading. As shown in **Figure 1-15**, the size of Pt particles on the Pt/P25 catalyst prepared at 873 K is determined to be 6.7 nm, which is much larger than that prepared at 673 K (3.1 nm). This is due to the sintering of Pt particles by a high-temperature treatment.[24,25] **Figure 1-16b** shows the results obtained via a 12 h photoreaction with respective catalysts. Although the nitrosobenzene selectivities are similar, the activity significantly decreases with an increase in the size of Pt particles because the number of surface Pt atoms decreases with an increase in the size of Pt particles.[66] This suppresses the transfer of e^- from photoactivated Pt atoms to anatase[24] as well as deprotonation of aniline, resulting in decreased photocatalytic activity. **Figure 1-12e** shows the DRIFT spectrum of aniline adsorbed onto the Pt_2/P25 catalyst prepared at 873 K. The signal intensity at 3323 cm^{-1}, assigned to the anilino anion, is much weaker than the catalyst prepared at 673 K (**Figure 1-12b**). This suggests that the catalyst with larger Pt particles is less active for deprotonation of aniline. The findings described above clearly indicate that the Pt/P25 catalyst containing 2 wt % Pt particles with ~3 nm diameters exhibits the best catalytic performance for aerobic oxidation of aniline.

Pt$_{0.5}$/P25
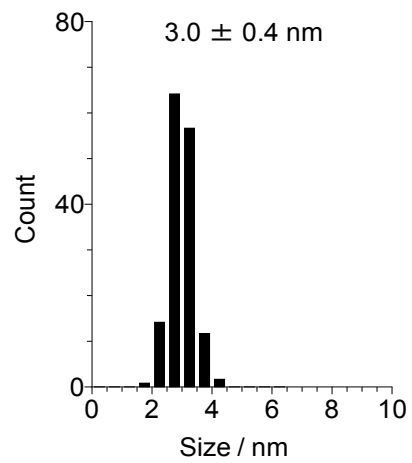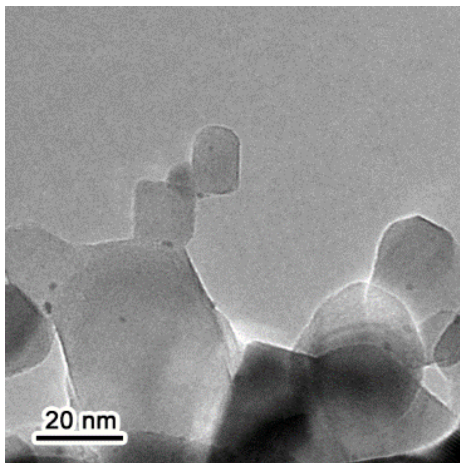
Pt$_4$/P25

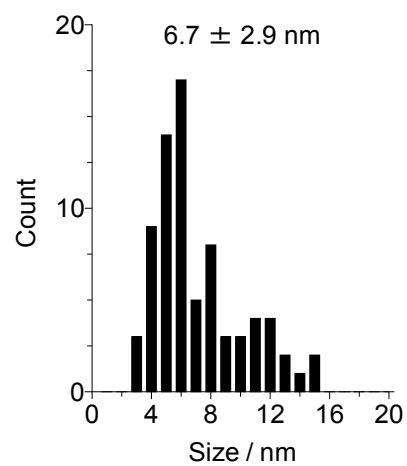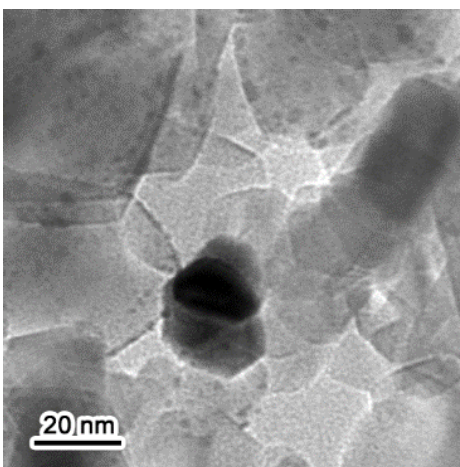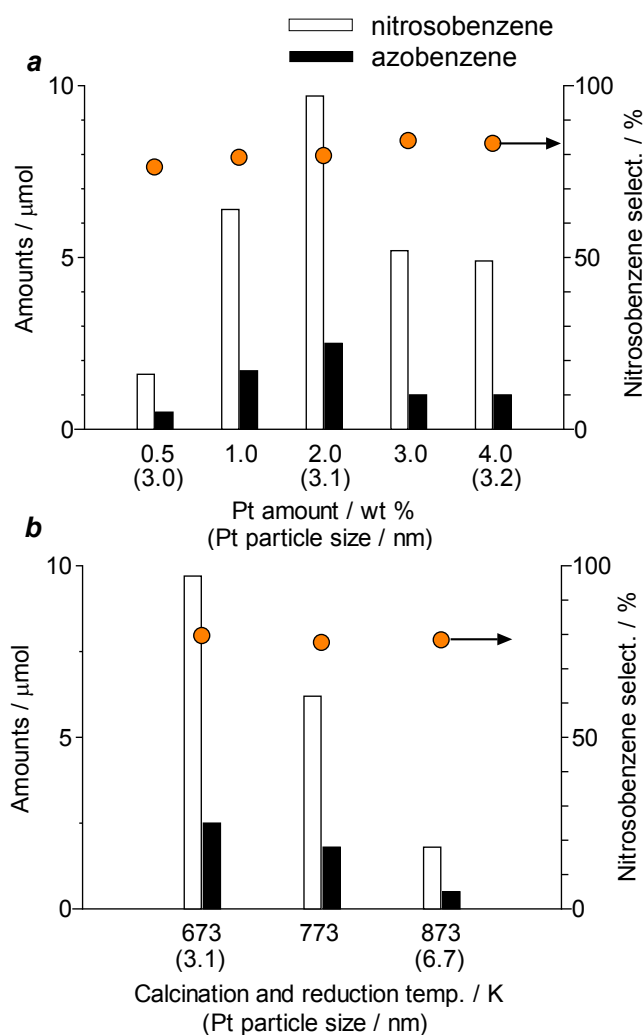
Pt$_2$/P25 prepared at 873 K

Figure 1-15. Typical TEM images of Pt/P25 catalysts and size distribution of Pt particles.
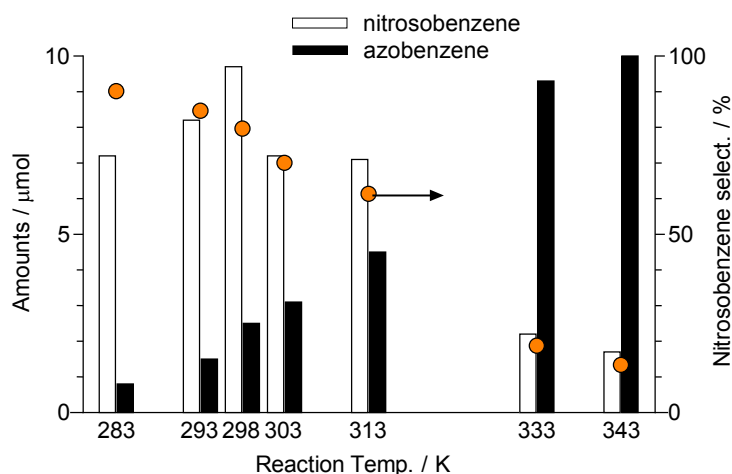
Figure 1-16. Effect of (a) the amount of Pt loaded and (b) calcination and reduction temperature on the amounts of (white) nitrosobenzene and (black) azobenzene produced during photocatalytic oxidation of aniline with Pt/P25. Orange symbols denote the nitrosobenzene selectivity. The calcination and reduction temperature employed for the preparation of catalysts (a) is 673 K, and the Pt loading of the catalysts (b) is 2 wt %. Reaction conditions are identical to those described in the legend of **Figure 1-5**.

## 3-7. Effect of Reaction Temperature on Selectivity

Photocatalytic oxidation of aniline on the Pt/P25 catalyst produces azobenzene as a byproduct, which is formed by subsequent condensation of aniline and the formed nitrosobenzene.[13] The formation of azobenzene strongly depends on the reaction temperature. **Figure 1-17** summarizes the amounts of nitrosobenzene and azobenzene produced by a 12 h photoreaction at different temperatures. An increase in reaction temperature significantly decreases the amount of nitrosobenzene formed, along with an increase in the level of azobenzene formation, because of the enhanced condensation of aniline and the formed nitrosobenzene. The nitrosobenzene selectivity at 343 K is only 13%. In contrast, at lower temperatures

(<298 K), nitrosobenzene is selectively produced; the selectivity at 283 K is increased to 90%. These data suggest that photoreaction at low temperatures suppresses the condensation of aniline with the product nitrosobenzene, thus facilitating selective nitrosobenzene formation.

Figure 1-17. Effect of reaction temperature on the amounts of (white) nitrosobenzene and (black) azobenzene produced during photocatalytic oxidation of aniline. Orange symbols denote the nitrosobenzene selectivity. Reaction conditions are identical to those described in the legend of **Figure 1-5**.
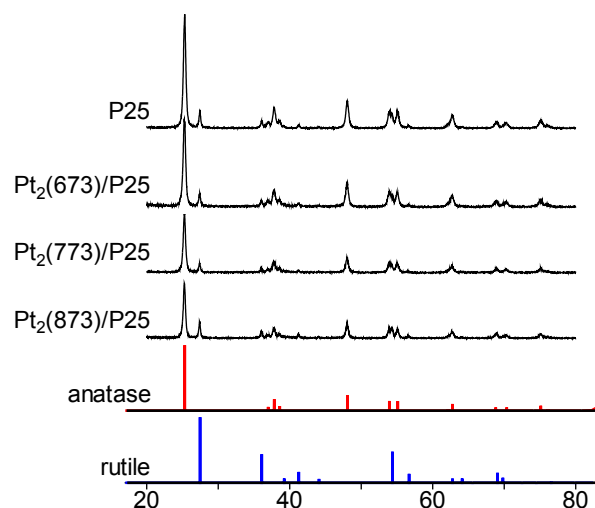
Figure 1-18. XRD patterns of Pt_2/P25 catalysts prepared at different calcination temperature. The anatase (A) and rutile (R) contents were determined with the equation; A (%) $= I_A(101) / [I_A(101) + 1.4I_R(110)] \times 100$ (Ramis, G.; Busca, G.; Cristiani, C.; Lietti, L.; Forzatti, P.; Bregani, F. *Langmuir* **1992**, *8*, 1744–1749).

4. Conclusion

The author found that the Pt/P25 catalyst promotes efficient aerobic oxidation of aniline to nitrosobenzene under visible light irradiation (>450 nm). Pt nanoparticles activated by visible light transfer their e^- to the TiO_2 conduction band. The positive charge that remained on the Pt surface oxidizes aniline, and the e^- on TiO_2 reduces O_2, promoting aerobic oxidation of aniline. The high activity of Pt/P25 is ascribed to the high Lewis basicity of Pt particles due to the strong Pt−support interaction at the anatase−rutile interfaces. These Pt particles promote reductive deprotonation of aniline, resulting in the efficient photooxidation of aniline. The catalytic activity of Pt/P25 strongly depends on the amount and size of Pt particles. The catalyst containing 2 wt % Pt particles with ~3 nm diameters exhibits the best catalytic performance. The selectivity for nitrosobenzene formation also depends on the reaction temperature; reaction at low temperatures suppresses condensation of aniline with the formed nitrosobenzene and produces nitrosobenzene with a very high selectivity (~90%).

5. References

[1] Yamamoto, H.; Momiyama, N. *Chem. Commun.*, **2005**, 3514–3525.

[2] Adam, W.; Krebs, O. *Chem. Rev.,* **2003**, *103*, 4131–4146.

[3] Zhao, D.; Johansson, M.; Backvall, Jan-E. *Eur. J. Org. Chem.*, **2007**, 4431–4436.

[4] Defoin, A. *Synthesis*, **2004**, *5*, 706–710.

[5] Gowenlock, B. G.; Richer-Addo, G. B. *Chem. Rev.* **2004**, *104*, 3315–3340.

[6] Meenakshisundaram, S.; Selvaraju, M.; Gowda, N. M. M.; Rangappa, K. S. *J. Chem. Kinet*, **2005**, *37*, 649–657.

[7] Priewish B.; Braun, K. R. *J. Org. Chem.* **2005**, *70*, 2350–2352.

[8] Moller, E. R.; Jorgensen, K. A. *J. Am. Chem. Soc.* **1993**, *115*, 11814–11822.

[9] Sakaue, S.; Tsubakino, T.; Nishiyama, Y.; Ishii, Y. *J. Org. Chem.* **1993**, *58*, 3633–3638.

[10] Grirrane, A.; Corma, A.; Garcia, H. *Science* **2008**, *322*, 1661–1664.

[11] Kus, N. S. *Moatsh Chem.* **2010**, *141*, 1089–1091.

[12] Perez, Y.; Aprile, C.; Corma, A. *Catal. Lett.* **2010**, *134*, 204–209.

[13] Biradar, A. V.; Kotbagi, T. V.; Dongare, M. K.; Umbarkar, S. B. *Tetra. Lett.* **2008**, *49*, 3616–3619.

[14] Porta, F.; Pizzotti, M.; Cenini, S. *J. Org. Chem.* **1981**, *222*, 279–284.

[15] Fox, M. A. *Acc. Chem. Res.* **1983***, 16*, 314–321.

[16] Fox, M. A.; Dulay, M. T. *Chem. Rev.* **1993**, *93*, 341–357.

[17] Plamisano, G.; Augugliaro, V.; Pagliaro, M.; Plamisano, L. *Chem. Commun.* **2007**, 3425–3437.

[18] Shiraishi, Y.; Hirai, T. *J. Photochem. Photobiol., C* **2008**, *9*, 157–170.

[19] Karunakaran, C.; Senthilvelan, S.; Karuthapandian, S. *J. Photochem. Photobiol., A* **2005**, *172*, 207–213.

[20] Karunakaran, C.; Senthilvelan, S.; Karuthapandian, S. *Sol. Energy Mater. Sol. Cells* **2005**, *89*, 391–402.

[21] Karunakaran, C.; Senthilivelan, S. *J. Mol. Catal. A: Chem.* **2005**, *233*, 1–8.

[22] Tsukamoto, D.; Shiraishi, Y.; Sugano, Y.; Ichikawa, S.; Tanaka, S.; Hirai, T. *J. Am. Chem. Soc.* **2012**, *134*, 6309–6315.

[23] Sugano, Y.; Shiraishi, Y.; Tsukamoto, D.; Ichikawa, S.; Tanaka, S.; Hirai, T. *Angew. Chem. Int. Ed.,* **2013**, *52*, 5295–5299

[24] Shiraishi, Y.; Tsukamoto, D.; Sugano, Y.; Shiro, A.; Ichikawa, S.; Tanaka, S.; Hirai, T. *ACS Catal.,* **2012**, *2,* 1984–1992.

[25] Shiraishi, Y.; Sakamoto, H.; Sugano, Y.; Ichikawa, S.; Hirai, T. *ACS Nano,* **2013**, *7,* 9287–9297.

[26] Schottky, W. *Z. Phys.* **1939**, *113*, 367–414.

[27] Hao, Q.; Juluri, B. K.; Zheng, Y. B.; Wang, B.; Chiang, I–Kao; Jensen, L.; Crespi, V.; Eklund, P. C.; Huang, T. J. *J. Phys. Chem.* **2010**, *114*, 18059–18066.

[28] *Sachtleben Chemie GmbH*, June 24, **1994**.

[29] Otani, B.; Prieto-Mahaney, O. O.; Li, D.; Abe, P. *J. Photochem. Photobiol. A.* **2010**, *226*, 179–182.

[30] Shiraishi, Y.; Hirakawa, H.; Togawa, Y.; Sugano. Y.; Ichikawa, S.; Hirai, T.; *ACS Catal.* **2013**, *3*, 2318–2326.

[31] Shiraishi, Y.; Sugano, Y.; Tanaka, S.; Hirai, T. *Angew. Chem. Int. Ed.* **2010**, *49*, 1656–1660.

[32] Shiraishi, Y.; Saito, N.; Hirai, T. *J. Am. Chem. Soc.* **2005**, *127*, 12820–12822.

[33] Shiraishi, Y.; Togawa, Y.; Tsukamoto, D.; Tanaka, S.; Hirai, T. *ACS Catal.* **2012***, 2*, 2475–2481.

[34] Shiraishi, Y.; Tanaka, K.; Shirakawa, E.; Sugano, Y.; Ichikawa, S.; Tanaka, S.; Hirai, T. *Angew. Chem., Int. Ed.* **2013**, *52*, 8304–8308.

[35] Shiraishi, Y.; Matsunaga, Y.; Hirai, T. *Chem. Commun.* **2012**, *48*, 5485–5487.

[36] Shiraishi, Y.; Ikeda, M.; Tsukamoto, D.; Tanaka, S.; Hirai, T. *Chem. Commun.* **2011**, *47*, 4811–4813.

[37] Shiraishi, Y.; Takeda, Y.; Sugano. Y.; Ichikawa, S.; Tanaka, S.; Hirai, T. *Chem. Commun,* **2011**, *47*, 7863–7865.

[38] Bigall, N. C.; Hartling, T.; Klose, M.; Simon, P.; Eng, L. M.; Eychmuller, A. *Nano Lett.* **2008**, *8*, 4588–4592.

[39] Proch, S.; Herrmannsdörfer, J.; Kempe, R.; Kern, C.; Jess, A.; Seyfarth, L.; Senker, J.; *Chem.- Eur. J.* **2028**, *14*, 8204–8212.

[40] Hong, H.; Hu, L.; Li, M.; Zheng, J.; Sun, X.; Lu, X.; Cao, X.; Lu, J.; Gu, H. *Chem.- Eur. J.* **2011**, *17*, 8726–8730.

[41] He, Y.; Zeng, T. *J. Phys. Chem. C*, **2010**, *114*, 18023–18030.

[42] Fatti, N. D.; Voisin, C.; Achermann, M.; Tzortzakis, S.; Christofilos, D.; Vallee, F. *Phys. Rev. B*, **2000**, *61,* 16956–16966.

[43] Mendoza, B. S. *Phys. Rev. B*, **1999**, *60*, 14334–14340.

[44] Link, S.; Burda, C.; Wang, Z. L.; El-Sayed, M. A. *J. Chem. Phys.* **1999**, *111*, 1255–1264.

[45] Kirillova, M. M.; Makhnev, A. A.; Shreder, E. I.; Dyakina, V. P.; Gorina, N. B. *Phys. stat. sol.* **1995**, *187*, 231–240.

[46] Morkel, M.; Unterhalt, H.; Kluner, T.; Rupprechter, G.; Freund, H. J. *Sur. Sci.* **2005**, *586,* 146–156.

[47] Anpo, M.; Che, M.; Fubini, B.; Garrone, E.; Giamello, E.; Paganini, M. C. *Top. Catal.* **1999**, *8*, 189–198.

[48] Ohno, T.; Sarukawa, K.; Matsumura, M. *J. Phys. Chem. B* **2001**, *105*, 2417–2420.

[49] As shown in **Figure 1-8a** (black), the Pt/P25 catalyst when left in the dark with O_2 shows almost no signal at g values of <1.99. Visible light irradiation of the catalyst (blue), however, creates signals assigned to Ti^{3+} species formed on rutile TiO_2.[50] This suggests that visible light absorption by Pt particles transfers their e^- to the TiO_2 support. In contrast, visible light irradiation of the Pt/anatase catalyst (**Figure 1-9b**) shows almost no Ti^{3+} signal. This is probably because the e^- transferred from photoactivated Pt particles to anatase are efficiently consumed by the reduction of O_2. This agrees well with the strong O_2^- signals. Visible light irradiation of the Pt/rutile catalyst (**Figure 1-9c**) also shows almost no Ti^{3+} signal, but the intensity of the O_2^- signal is much weaker. This suggests that, in the Pt/rutile system, the transfer of e^- from photoactivated Pt to rutile is difficult. In contrast, visible light irradiation of the Pt/P25 catalyst (**Figure 1-9a**) creates Ti^{3+} species formed on the rutile TiO_2, although the transfer of e^- from photoactivated Pt to rutile is difficult. This can be rationalized by the transfer of e^- from anatase to rutile, as is often observed for related P25 systems (for example, refs 52 and 53). As reported previously,[48] the e^- on the rutile surface are inactive for O_2 reduction; therefore, the Ti^{3+} species on rutile TiO_2 remain even in the presence of O_2.

[50] Okumura, M.; Coronado, J. M.; Soria, J.; Haruta, M.; Conesa J. C. *J. Catal.* **2001**, *203*, 168–174.

[51] Ohno, T.; Tokieda, K.; Higashida, S.; Matsumura, M. *Appl. Catal., A* **2003**, *244*, 383–391.

[52] Komaguchi, K.; Nakano, H.; Araki, A.; Harima, Y.; *Chem. Phys. Lett.* **2006**, *428*, 338–342.

[53] Zhou, C.; Han, J.; Song, G.; Guo, R. *Eur. Polym. J.,* **2008**, *44*, 2850–2858.

[54] Horsley, J. A. *J. Am. Chem. Soc.* **1979**, *101*, 2870–2874.

[55] Sexton, B. A.; Hughes, A. E.; Foger, K. *J. Catal.* **1982**, *77*, 85–93.

[56] Zhang, X.; Lin, Y.; He, D.; Zhang, J.; Fan, Z.; Xie, T. *Chem. Phys. Lett.* **2011**, *504*, 71–75.

[57] Gong, X.-Q.; Selloni, A.; Dulub, O.; Jacobson, P.; Diebold, U. *J. Am. Chem. Soc.* **2008**, *130*, 370–381.

[58] Bu, Y.; Chen, Z.; Li, W. *App. Catal. B: Env.* **2014**, *144*, 622–630.

[59] Akita, T.; Lu, P.; Ichikawa, S.; Tanaka, K.; Haruta, M. *Surf. Interface Anal.* **2001**, *31*, 73–78.

[60] Evans, J. C. *Spec. Acta,* **1960**, *16*, 428–442.

[61] Brown, E. V.; Kipp, W. H.; *J. Org. Chem.,* **1971***, 36*, 170–173.

[62] Maeda, Y.; Higuchi, T.; Ikeda, I. *Langmuir,* **2000**, *16*, 7503–7509.

[63] Fukuto, J. M.; Di Stefano, E. W.; Burstyn, J. N.; Valentine, J. S.; Cho, A. K. *Biochemistry* **1985**, *24*, 4161–4167.

[64] Ishida, T.; Nagaoka, M.; Akita, T.; Haruta, M. *Chem.–Eur. J.* **2008**, *14*, 8456–8460.

[65] Uchihara, T.; Matsumura, M.; Yamamoto, A.; Tsubomura, H.; *J. Phys. Chem.* **1989**, *93*, 5870–5874.

[66] The anatase-to-rutile phase transition of P25 TiO_2 upon calcination at higher temperatures is not the major factor for decreased photocatalytic activity. As shown in **Figure 1-18**, XRD patterns indicated the anatase/rutile ratios of both Pt_2/P25 catalysts prepared by calcination at 673 and 773 K to be 81/19, which is similar to that of pure P25 TiO_2 (82/18), although calcination at 873 K increases the ratio to 75/25 by the thermal phase transition. As shown in **Figure 1-9b**, the catalyst prepared at 773 K showed activity lower than the activity of that prepared at 673 K, even though their anatase/rutile ratios are similar. This indicates that the phase transition of the P25 support is not the major factor in the decreased activity of the catalysts prepared at higher calcination temperatures.

Chapter II

Enhanced Hot Electron Injection on Pt–Cu Bimetallic Alloy Nanoparticles Supported on TiO$_2$

1. Introduction

Aerobic oxidation by heterogeneous catalysts with molecular oxygen (O$_2$) is an indispensable process for the synthesis of chemicals from the viewpoint of green chemistry.[1] Photocatalytic oxidation with O$_2$ has also been studied extensively with semiconductor titanium dioxide (TiO$_2$);[2–6] several types of substrates such as alcohols, amines, hydrocarbons, and sulfides are successfully oxidized at atmospheric pressure and room temperature. One of the critical issues for practical application of the photocatalytic processes is the low catalytic activity under irradiation of visible light ($\lambda > 400$ nm), the main component of solar irradiance. Several TiO$_2$ materials doped with nitrogen,[7,8] sulfur,[9,10] carbon,[11,12] or boron atoms[13,14] have been proposed to extend the absorption edge into the visible region. These doped catalysts, however, suffer from low quantum yields for reaction (<0.5%) because they inherently contain a large number of crystalline lattices that behave as charge recombination centers.[15] Design of visible-light-driven catalysts that promote efficient aerobic oxidation is still a challenge.

Metal nanoparticle/semiconductor heterojunction is one powerful system for the creation of photocatalysts activated by visible light.[16] Earlier, we reported that gold (Au) nanoparticles loaded on TiO$_2$ promote aerobic oxidation under visible light.[17] The reaction is promoted via the absorption of visible light by the Au nanoparticles due to the resonant oscillation of free electrons coupled by light, known as localized surface plasmon resonance.[16] Collective oscillation of 6sp band electrons (e$^-$) on the surface Au atoms promotes intraband transition to the sp conduction band. The e$^-$ is transferred to the TiO$_2$ conduction band. The positive charge formed on the surface of Au particles oxidizes the substrate, while the e$^-$ on the TiO$_2$ conduction band is consumed by the reduction of O$_2$. This catalytic cycle successfully promotes aerobic oxidation of substrates even at room temperature. The apparent quantum yield for oxidation of alcohol determined by the irradiation of 550 nm monochromatic light is 3.8 %, which is much higher than that obtained with the doped catalysts (<0.5 %).[7–14] The metal/semiconductor system is chemically stable even under aerated conditions as compared to the doped catalysts and shows a potential as a visible-light-driven catalyst.

Platinum (Pt) nanoparticles also absorb light in the visible region due to the interband transition of 5d band e$^-$ to the sp conduction band,[18] as schematically shown in **Figure 2-1**. Very recently, we found that Pt

nanoparticles loaded on anatase TiO_2 (Pt/anatase) efficiently promote aerobic oxidation under visible light irradiation.[19] The apparent quantum yield for the reaction is 7.1% (550 nm), which is much higher than that obtained with the Au catalyst (3.8%). The very high activity is due to the strong affinity between Pt nanoparticles and the anatase surface.[20] This facilitates efficient e⁻ transfer from the photoactivated Pt particles to anatase.

We then explored further activity improvement of the Pt/anatase system. The rate-determining step for this system is the e⁻ transfer from photoactivated nanoparticles to anatase. As shown in **Figure 2-1**, the metal/semiconductor heterojunction creates a Schottky barrier (ϕ_B) at the interface.[21] Photoactivated e⁻ on the Pt particles must therefore overcome this barrier and is transferred to anatase. This implies that the height of ϕ_B strongly affects the efficiency for e⁻ transfer. The ϕ_B is defined as the difference between the work function of metal (W) and the electron affinity of the semiconductor conduction band (χ):[22]

$$\phi_B = W - \chi \tag{1}$$

It is well-known that the work function of metal decreases by the alloying of other metal components with a lower work function.[23,24] This suggests that alloying of other metal with Pt would decrease the work function of Pt nanoparticles. This may decrease ϕ_B and promote efficient e⁻ transfer from nanoparticles to anatase.
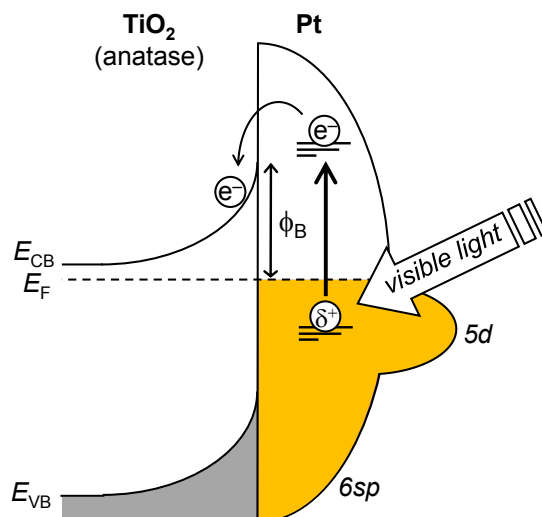
Figure 2-1. Proposed mechanism for electron transfer from photoactivated Pt particles to anatase. E_F and ϕ_B denote the Fermi level and the height of the Schottky barrier, respectively.

Here the author reports that bimetallic alloy nanoparticles consisting of Pt and copper (Cu), supported on anataseTiO$_2$, significantly enhance aerobic oxidation under visible light. The apparent quantum yield for the reaction, 17% (550 nm), is more than double that obtained with monometallic Pt catalyst (7.1%).[19] The activity of this alloy system depends strongly on the mole ratio of Pt and Cu and the size of alloy particles.

The catalyst loaded with alloy nanoparticles, consisting of 80 mol % of Pt and 20 mol % of Cu with 3–5 nm diameter, exhibits the highest activity. The catalyst is successfully activated by sunlight and enables efficient and selective aerobic oxidation of alcohols at ambient temperature.

2. Experimental Section

2-1. Materials

All reagents used were purchased from Wako, Tokyo Kasei, and Sigma-Aldrich and used without further purification. Water was purified by the Milli-Q system. Anatase TiO_2 (JRC-TIO-1), P25 (JRC-TIO-4; average particle size, 24 nm; BET surface area, 57 m^2 g^{-1} ; anatase/rutile = ~83/17), and rutile TiO_2 (JRC-TIO-6; 15 nm; 104 m^2 g^{-1}) were kindly supplied from the Catalyst Society of Japan.

2-2. Preparation of catalysts

2-2-1. $Pt_{1-x}Cu_x/TiO_2$

These catalysts with 0.4 mol % of metal loading [x {= Cu/(Pt + Cu)} = 0, 0.1, 0.2, 0.3, 0.4, 0.5, 0.6, and 1] were prepared as follows. TiO_2 (1.0 g) and $H_2PtCl_6 \cdot 6H_2O$ / $Cu(NO_3)_2 \cdot 3H_2O$ (26.8/0, 24.2/1.2, 21.4/2.4, 9.4/3.6, 8.1/4.8, 6.7/ 6.1, 5.3/7.2, and 0/12.2 mg) were added to water (40 mL), and the solvent was evaporated with vigorous stirring at 353 K for 12 h. The resultant mixture was calcined under air flow and reduced with H_2 flow at the identical temperature. The temperature employed for calcination and reduction was 673 K unless otherwise noted. The heating rate and holding time for these treatments were 2 K min^{-1} and 2 h, respectively.

2-2-2. $Pt_{0.8}$ + $Cu_{0.2}$/Anatase

The catalyst with 0.4 mol % of metal loading was prepared by a step-by-step method as follows: Anatase TiO_2 (1.0 g) and $H_2PtCl_6 \cdot 6H_2O$ (21.4 mg) were added to water (40 mL), and the solvent was evaporated with vigorous stirring at 353 K for 3 h. The particles were recovered by centrifugation, washed with water, and dried at 353 K for 12 h. The powders were calcined at 673 K for 2 h under air flow and reduced at 673 K for 2 h under H_2 flow. The obtained powder and $Cu(NO_3)_2 \cdot 3H_2O$ (2.4 mg) were added to water (40 mL), and solvent was evaporated with vigorous stirring at 353 K for 12 h. The resultant mixture was calcined at 673 K for 2 h under air flow and reduced at 673 K for 2 h under H_2 flow.

2-2-3. $Pt_{0.8}M_{0.2}$/Anatase (M = Au, Ag, Pd)

These catalysts with 0.4 mol % of metal loading were prepared as follows: Anatase TiO_2 (1.0 g) and

$H_2PtCl_6 \cdot 6H_2O$ / $HAuCl_4 \cdot 4H_2O$ (21.4/4.2 mg), $H_2PtCl_6 \cdot 6H_2O$ / $AgNO_3$ (21.4/1.7 mg), or $H_2PtCl_6 \cdot 6H_2O$ / $Pd(NO_3)_2$ (21.4/2.3 mg) were added to water (40 mL), and solvent was evaporated with vigorous stirring at 353 K for 12 h. The resultant mixture was calcined at 673 K for 2 h in air and reduced at 673 K for 2 h with H_2.

2-2-4. $Au_{0.8}Cu_{0.2}$/Anatase

This catalyst with 0.4 mol % metal loading was prepared according to the procedure described previously.[25] Anatase TiO_2 (1.0 g) was added to water (100 mL) containing $HAuCl_4 \cdot 4H_2O$ (16.8 mg) and $Cu(NO_3)_2 \cdot 3H_2O$ (2.6 mg). The pH of solution was adjusted to ~7 with 1mM NaOH, and the solution was stirred at 353 K for 3 h. The particles were recovered by centrifugation, washed thoroughly with water, and dried at 353 K for 12 h. The obtained powders were reduced at 673 K under H_2 flow. The heating rate was 2 K min^{-1}, and the temperature was kept at 673 K for 2 h.

2-3. Reaction Procedure

Catalyst (5 mg) was added to toluene (5 mL) containing an alcohol within a Pyrex glass tube (φ12 mm; capacity, 20 mL). The tube was sealed with a rubber septum cap. The catalyst was dispersed well by ultrasonication for 5 min, and O_2 was bubbled through the solution for 5 min. The tube was immersed in a temperature-controlled water bath (298 ± 0.5 K). The tube was photoirradiated with magnetic stirring using a 2 kW Xe lamp (USHIO Inc.) and filtered through a glass filter (CS3-72; Kopp Glass Inc.) to give light wavelength of $\lambda > 450$ nm, where the light intensity at 450–800 nm was 16.8 mW cm^{-2}. Sunlight reactions were performed on December, 4, 2012 at 10:00–14:00 at the top of the laboratory building (latitude 34.7 north, longitude 135.5 east). The light intensity at 300–800 nm was 4.6 mW cm^{-2}. The highest temperature during reaction was 293 K, and the dark reactions were performed at 293 K. After the reaction, the catalyst was recovered by centrifugation. The liquid-phase products were analyzed by GC-FID (Shimadzu, GC-2040).

2-4. Action Spectrum Analysis

Catalyst (8 mg) was suspended in toluene (2 mL) containing benzyl alcohol (0.4 mmol) within a Pyrex glass tube (φ12 mm; capacity, 20 mL). The tube was sealed with a rubber septum cap. The catalyst was dispersed well by ultrasonication for 5 min, and O_2 was bubbled through the solution for 5 min. The solution was photoirradiated with 2 kW Xe lamp (USHIO Inc.), where the incident light was monochromated by band-pass glass filters (Asahi Techno Glass Co.). The full width at half-maximum (fwhm) of the

monochromatic light was 11–16 nm. The temperature of solution during photoirradiation was kept at 298 ± 0.5 K with a temperaturecontrolled water bath. The photon number entered into the reaction vessel was determined with a spectroradiometer USR-40 (USHIO Inc.).

2-5. ESR Measurement

The spectra were recorded at the X-band using a Bruker EMX-10/12 spectrometer with a 100 kHz magnetic field modulation at a microwave power level of 10.0 mW,[17] where microwave power saturation of the signal does not occur. The magnetic field was calibrated with 1,1'-diphenyl-2-picrylhydrazyl (DPPH). Catalyst (20 mg) was placed in a quartz ESR tube and evacuated at 423 K for 3 h. After cooling the sample tube to room temperature, O_2 (20 Torr) was introduced to the tube and kept for 3 h at 298 K. The tube was photoirradiated for 1 h at 298 K using a Xe lamp (2 kW; USHIO Inc.) at $\lambda > 450$ nm (with CS3-72; Kopp Glass Inc.). The ESR tube was then evacuated for 10 min to remove the excess amount of O_2 and subjected to analysis at 77 K.

2-6. Analysis

Total amounts of Pt and Cu in the catalysts were analyzed by an inductively coupled argon plasma atomic emission spectrometer (Sekio Instruments, Inc.; SPS7800), after dissolution of the catalysts in an aqua regia. Diffuse-reflectance UV–vis spectra were measured on an UV–vis spectrophotometer (Jasco Corp.; V-550 with Integrated Sphere Apparatus ISV-469) with $BaSO_4$ as a reference. TEM observations were carried out using an FEI Tecnai G2 20ST analytical electron microscope operated at 200 kV, equipped with an energy dispersive X-ray spectroscopy (EDX) detector.[26] EDX spectra from a metallic particle were taken under scanning transmission electron microscopy (STEM) mode. XPS measurements were performed using a JEOL JPS-9000MX spectrometer using Mg Kα radiation as the energy source. XRD patterns were obtained on a Philips XXX diffractometer with Cu Kα radiation. Hydrodynamic diameter of the catalysts was measured by a dynamic laser scattering spectrometer (LB-500, HORIBA).[26]
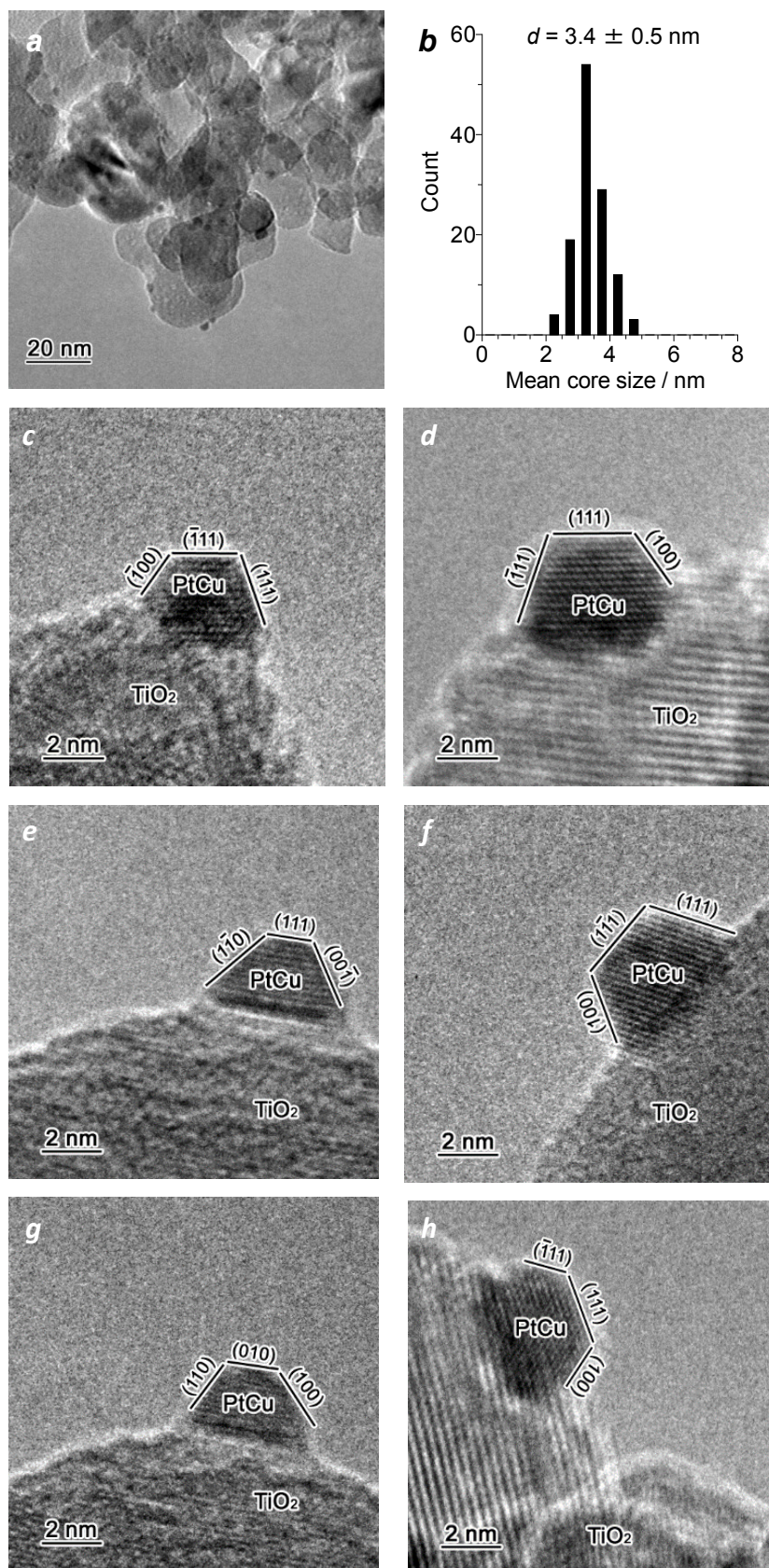
Figure 2-2. (a) Typical TEM image of $Pt_{0.8}Cu_{0.2}$/anatase catalyst (0.4 mol % of metal loading) and (b) size distribution of metal particles. (c–h) High-resolution TEM images.

3. Results and Discussion

3-1. Preparation and Properties of Bimetallic Catalysts

Pt–Cu bimetallic alloy particles were loaded on anatase TiO_2 (Japan Reference Catalyst, JRC-TIO-1; average particle size, 21.1 nm; Brunauer–Emmett–Teller (BET) surface area, 81 $m^2 g^{-1}$) by the impregnation of Pt and Cu precursors followed by reduction with H_2:[27,28] Anatase particles were added to water containing H_2PtCl_6 and $Cu(NO_3)_2$, and the water was evaporated with stirring. The resultant mixture was calcined in air for 2 h and reduced with H_2 for 2 h at 673 K, affording $Pt_{1-x}Cu_x$/anatase catalysts as brown powders. The total metal loading on the support is set at 0.4 mol % [= (Pt + Cu)/anatase × 100], and x denotes the mole fraction of Cu in the alloy [x = Cu/(Pt + Cu)].

Figure 2-2a shows a typical transmission electron microscopy (TEM) image of $Pt_{0.8}Cu_{0.2}$/anatase. Small nanoparticles were highly dispersed on the support. As shown in **Figure 2-2c–h**, high-resolution TEM images showed metal particles indexed as face-centered cubic (*fcc*) cuboctahedron structures. The average diameter of the particles (d) was calculated to be 3.4 nm (**Figure 2-2b**). As shown in **Figure2-3**, Pt_1/anatase, $Pt_{0.4}Cu_{0.6}$/anatase, and Cu_1/anatase catalysts contain metal particles with similar diameters (3.3, 3.4, and 3.3 nm, respectively), indicating that Cu alloying scarcely affects the size of metal particles.

Pt_1/anatase
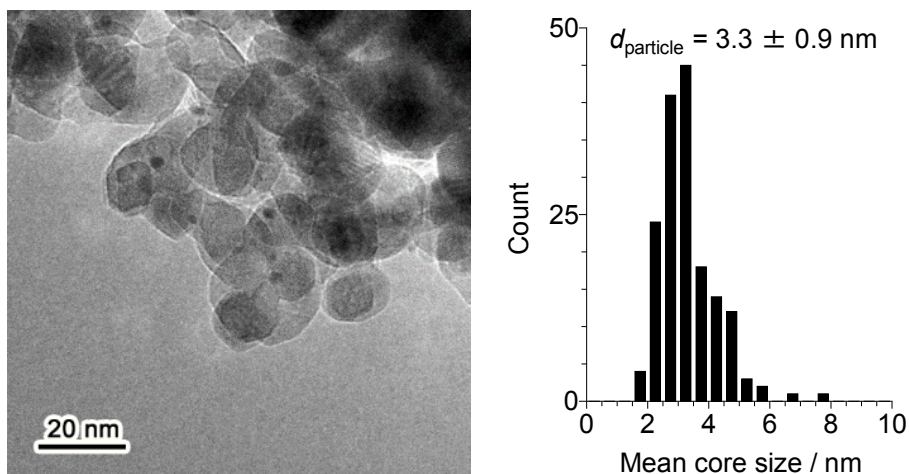
Pt$_{0.4}$Cu$_{0.6}$/anatase
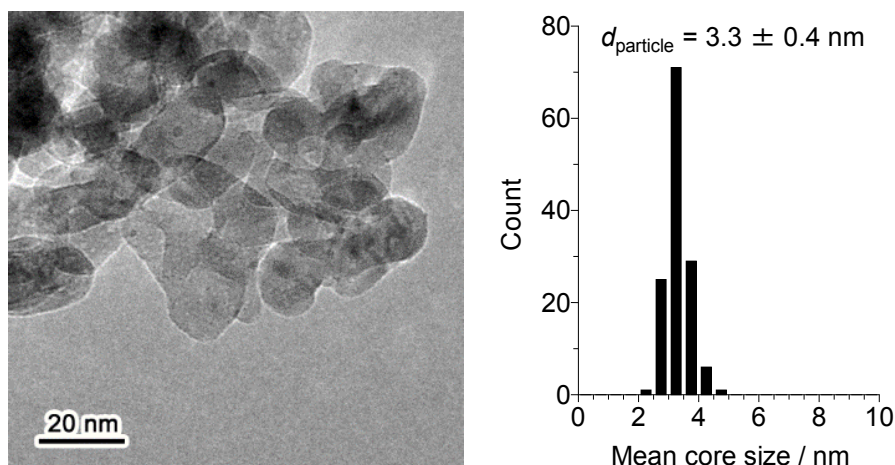
Cu$_1$/anatase
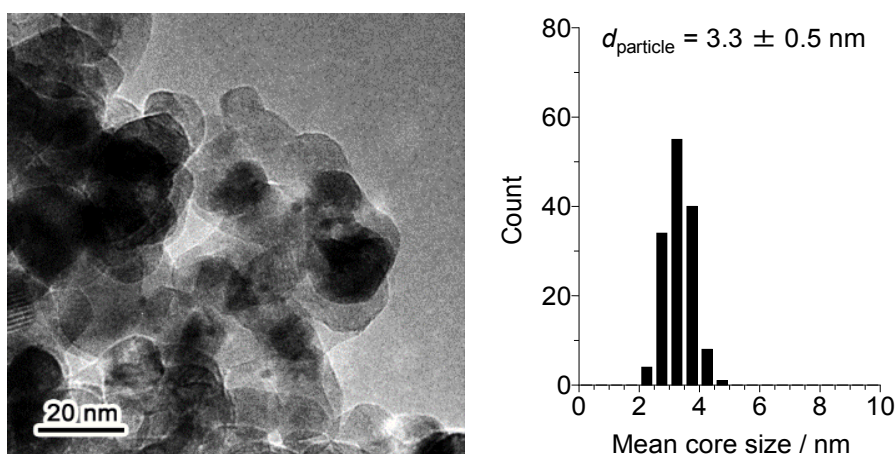
Figure 2-3. Typical TEM images of Pt$_1$/anatase, Pt$_{0.4}$Cu$_{0.6}$/anatase and Cu$_1$/anatase catalysts, and size distribution of metal particles.

X-ray photoelectron spectroscopy (XPS) of the alloy catalysts (**Figure 2-4**) shows Pt 4f peaks (70 and 74 eV) and a Cu 2p peak (~932 eV).[29] As observed for related Pt–Cu alloy systems,[30–32] the increase in Cu amount shifts the Cu peak to lower binding energy due to the expansion of atomic distance, although the Pt peak scarcely shifts. The surface Pt/Cu ratio of metal particles on Pt$_{0.8}$Cu$_{0.2}$/anatase determined by XPS analysis is 4.02 mol/mol. This is similar to the ratio of the total amount of Pt and Cu (3.95 mol/mol) in the catalysts determined by the inductively coupled plasma (ICP) analysis and the average Pt/Cu ratio (3.90 mol/mol) determined by the energy-dispersive X-ray spectroscopy (EDX) of some metal particles (**Figure 2-6**).

In addition, as shown in **Figure 2-2c–h**, the lattice spacing of alloy particles (111) determined by TEM observation (0.223 nm) is between the lattice spacing for standard Pt(111) (JCPDS 04-0802, 0.226 nm) and

44

Cu(111) (JCPDS 04-0836, 0.209 nm) and is the same as the value calculated based on Vegard's law (0.223 nm). These data suggest that Pt and Cu components in the alloy particles are mixed homogeneously. As shown in **Figure 2-5**, diffuse-reflectance UV–vis spectrum of Pt_1/anatase shows a broad absorption band at $\lambda > 400$ nm, assigned to the interband transition of Pt particles.[33] Cu_1/anatase shows similar absorption at $\lambda > 400$ nm, assigned to the light scattering by the Cu particles.[34,35] As a result of this, Pt–Cu alloy catalysts exhibit similar absorption spectra independent of their Pt/Cu ratio.
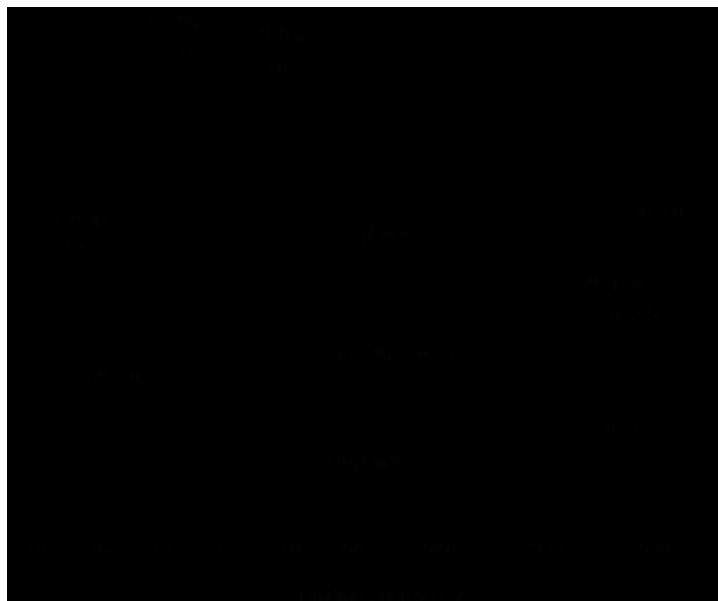
Figure 2-4. XPS results for respective catalysts.
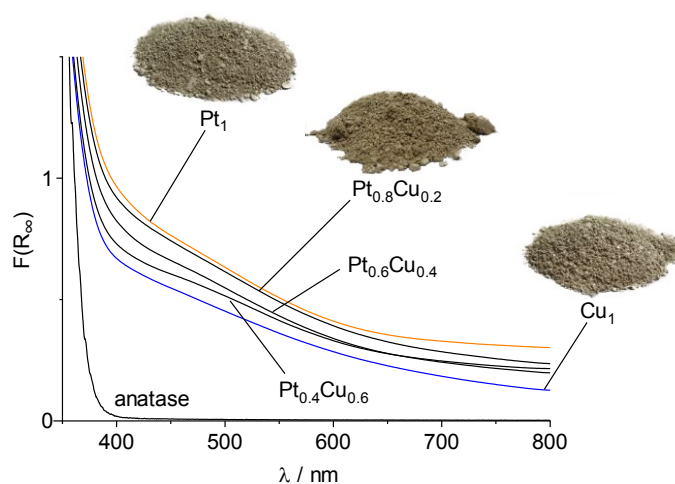
Figure 2-5. Diffuse-reflectance UV–vis spectra of $Pt_{1-x}Cu_x$/anatase (0.4 mol % of metal loading).
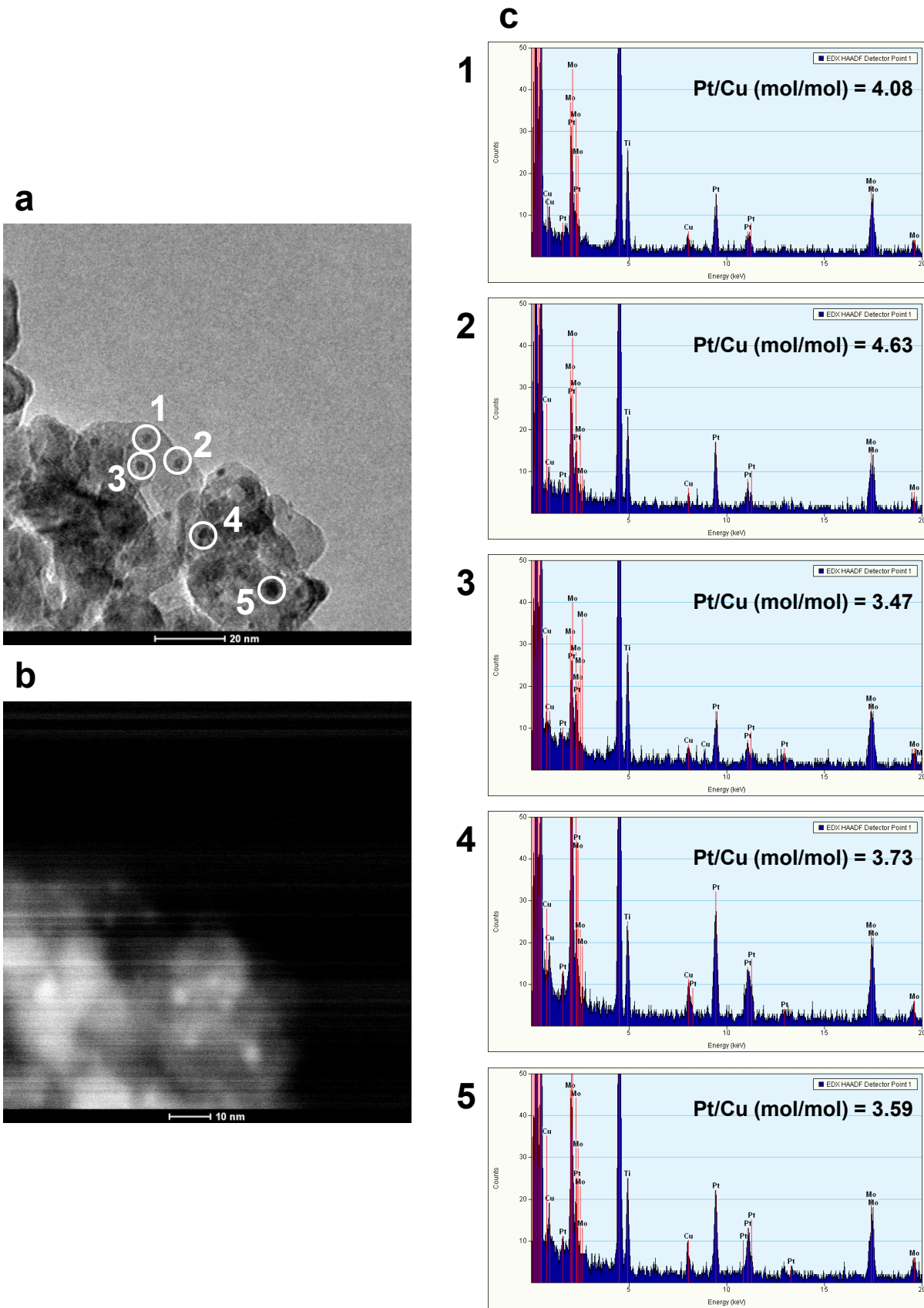
Figure 2-6. (a) TEM and (b) HAADF-STEM images of $Pt_{0.8}Cu_{0.2}$/anatase, and (c) EDX results for some of the metal nanoparticles.

3-2. Photocatalytic Activity of Alloy Catalysts

The activity of alloy catalysts was tested by oxidation of benzyl alcohol, a typical aerobic oxidation.[36] The reactions were performed by stirring a toluene solution (5 mL) containing benzyl alcohol (0.1 mmol) and catalys (5 mg) with O_2 (1 atm). The temperature of the solution was kept continuously at 298 ± 0.5 K by a digitally controlled water bath. **Figure 2-7** summarizes the amount of benzaldehyde produced by 4 h reaction with respective catalysts in the dark or visible light irradiation by a Xe lamp ($\lambda > 450$ nm). It is noted that both reactions selectively produce benzaldehyde (mass balance: >99%). In the dark (black), bare anatase promotes almost no reaction, but Pt_1/anatase produces 3 μmol of benzaldehyde due to the catalytic activity of Pt particles.[37,38] The increase in Cu amount decreases the activity, and Cu_1/anatase promotes almost no reaction. Visible light irradiation enhances the activity (white): Pt_1/anatase produces 9 μmol of benzaldehyde, which is 3 times that obtained in the dark. Alloy catalysts further enhance activity; $Pt_{0.8}Cu_{0.2}$/anatase produces the largest amount of benzaldehyde (18 μmol), which is twice that obtained with Pt_1/anatase (9 μmol). Further Cu alloying, however, decreases the activity, and Cu_1/anatase shows almost no activity. These data suggest that the alloy catalyst with a small amount of Cu promotes efficient aerobic oxidation under visible light irradiation. In addition, as shown in **Figure 2-8**, the $Pt_{0.8}Cu_{0.2}$/anatase catalyst maintains its activity even after prolonged photoirradiation (~24 h), indicating that the catalyst is stable under photoirradiation.

Anatase TiO_2 is necessary as the support. As shown in **Figure 2-7** ($Pt_{0.8}Cu_{0.2}$/P25), visible light irradiation of the $Pt_{0.8}Cu_{0.2}$ alloy loaded on P25 (a mixture of anatase and rutile TiO_2) also enhances activity, but the enhancement is lower than that of $Pt_{0.8}Cu_{0.2}$/anatase. In addition, $Pt_{0.8}Cu_{0.2}$/rutile shows much lower activity. These data suggest that Pt–Cu alloy particles loaded on anatase TiO_2 exhibit very high activity, as also observed for monometallic Pt/anatase system.[19] It must also be noted that (**Figure 2-7**) Pt–Au,[39] Pt–Ag,[40] Pt–Pd,[41] and Au–Cu[25] alloy particles, often used for aerobic oxidation, show activity much lower than that of the Pt–Cu alloy. In addition, the $Pt_{0.8}$ + $Cu_{0.2}$/anatase catalyst, prepared by a step-by-step deposition of respective Pt and Cu metals onto the anatase surface, scarcely exhibits reaction enhancement by visible light irradiation. These data clearly suggest that homogeneously mixed Pt–Cu alloy particles loaded on anatase TiO_2 are necessary for efficient aerobic oxidation under visible light.
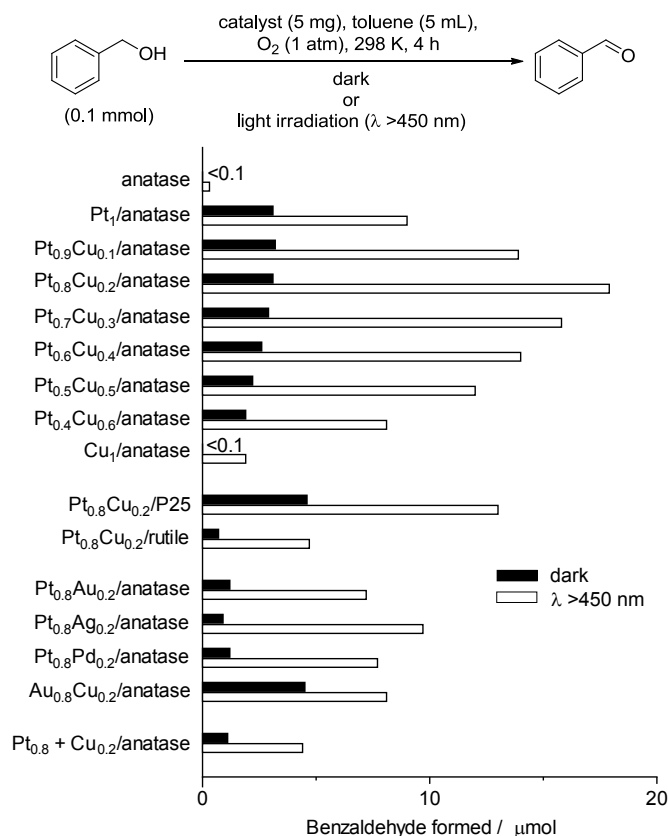
Figure 2-7. Amount of benzaldehyde formed by aerobic oxidation of benzyl alcohol with respective catalysts (0.4 mol % of metal loading), (black) in the dark, or (white) under irradiation of visible light ($\lambda >$ 450 nm; light intensity at 450–800 nm, 16.8 mW cm^{-2}).
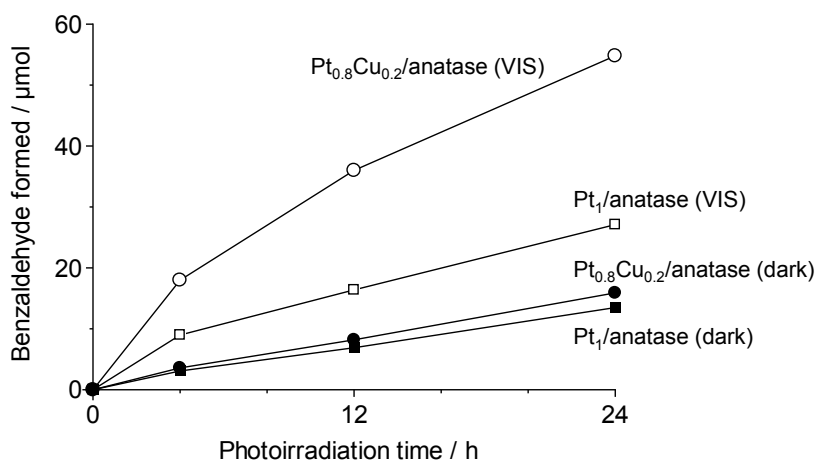

Figure 2-8. Time-dependent change in the amount of benzaldehyde formed during aerobic oxidation of benzyl alcohol with Pt$_1$/anatase and Pt$_{0.8}$Cu$_{0.2}$/anatase catalysts in the dark or under visible light irradiation ($\lambda >$450 nm). Reaction conditions are identical to those in **Figure 2-7**.

3-3. Mechanism for Reaction Enhancement

In the PtCu/anatase system, photoactivated alloy particles efficiently transfer e^- to anatase. This enhances the reduction of O_2 by e^- on the anatase surface, resulting in enhanced aerobic oxidation. The enhanced e^- transfer from the alloy particles to anatase is confirmed by electron spin resonance (ESR) analysis of the catalysts. **Figure 2-9a** (black) shows the ESR spectra of $Pt_{0.8}Cu_{0.2}$/anatase measured in the dark at 77 K after exposure to O_2. Two signals observed at $g = 2.001$ and 2.029 are assigned to O^- produced by dissociative adsorption of O_2 onto the oxygen vacancy sites of the TiO_2 surface.[42] As shown by the blue line in **Figure 2-9a**, visible light irradiation of the sample creates strong signals assigned to superoxide anion stabilized on the TiO_2 surface (O_2^-; $g_{xx} = 2.002$, $g_{yy} = 2.009$, $g_{zzI} = 2.028$, $g_{zzII} = 2.033$, $g_{zzIII} = 2.038$, and $g_{zzIV} = 2.052$).[43] This indicates that visible light irradiation of alloy nanoparticles indeed transfers their e^- to anatase, and the e^- reduces O_2 on the anatase surface. As shown in **Figure 2-9b**, Pt_1/anatase catalyst also exhibits an O_2^- signal by visible light irradiation, but the signal intensity is much lower than that obtained on the alloy catalyst. These data suggest that photoactivated PtCu alloy particles transfer their e^- to anatase more efficiently than the monometallic Pt particles.

The efficiency for e^- transfer from photoactivated nanoparticles to anatase depends on the Pt/Cu ratio of alloy particles. As shown in **Figure 2-9c**, visible light irradiation of $Pt_{0.4}Cu_{0.6}$/anatase with O_2 shows O_2^- signals much weaker than that formed on $Pt_{0.8}Cu_{0.2}$/anatase (**Figure 2-9a**). In addition, as shown in **Figure 2-9d**, Cu_1/anatase shows almost no O_2^- signal. The intensity of the O_2^- signal on the respective catalysts (**Figure 2-9a–d**) is consistent with the catalytic activity under visible light irradiation (**Figure 2-7**). These data suggest that the e^- transfer from photoactivated nanoparticles to anatase is the crucial factor controlling the photocatalytic activity. The $Pt_{0.8}Cu_{0.2}$/anatase catalyst efficiently promotes e^- transfer and exhibits very high activity.
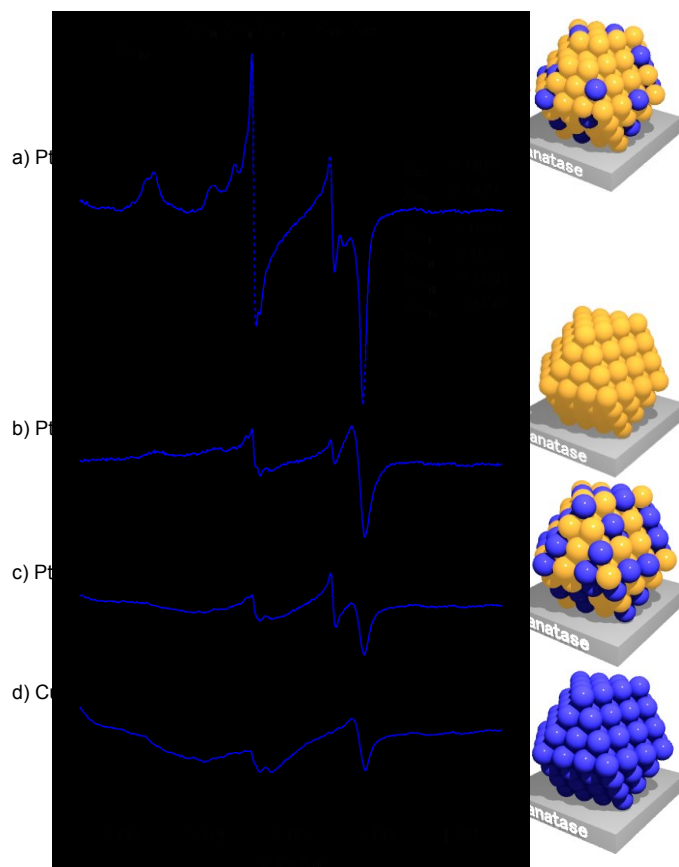
Figure 2-9. ESR spectra of (a) $Pt_{0.8}Cu_{0.2}$/anatase, (b) Pt_1/anatase, (c) $Pt_{0.4}Cu_{0.6}$/anatase, and (d) Cu_1/anatase measured at 77 K. The respective samples were treated with O_2 (20 Torr) for 3 h in the dark at 298 K (black). The samples were irradiated by visible light for 3 h at 298 K (blue). The metal loading of the catalysts is 0.4 mol %.
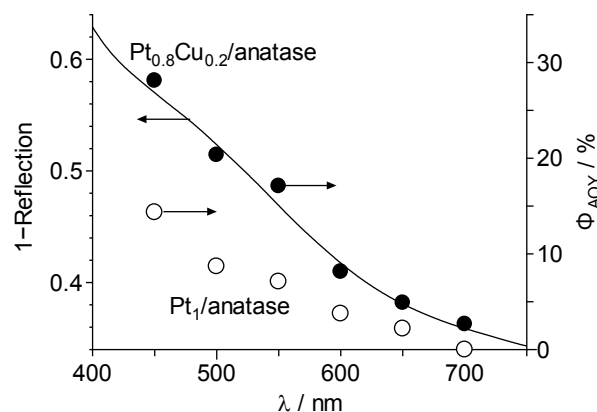
Figure 2-10. Action spectrum for aerobic oxidation of benzyl alcohol on $Pt_{0.8}Cu_{0.2}$/anatase and Pt_1/anatase catalysts (0.4 mol % of metal loading). The apparent quantum yield for benzaldehyde formation (Φ_{AQY}) was calculated with the equation; Φ_{AQY} (%) = [{$(Y_{vis} - Y_{dark}) \times 2$}/(photon number entered into the reaction vessel)] × 100, where Y_{vis} and Y_{dark} are the amounts of benzaldehyde formed (μmol) under light irradiation and dark conditions, respectively.

Figure 2-10 (black) shows the action spectrum for aerobic oxidation of benzyl alcohol with Pt$_{0.8}$Cu$_{0.2}$/anatase obtained by irradiation of monochromatic light. A good correlation is observed between the interband absorption of the catalyst and the apparent quantum yield for benzaldehyde formation (Φ_{AQY}). This suggests that, as shown in **Figure 2-1**, the interband excitation of alloy particles by visible light indeed promotes aerobic oxidation. It is also noted that Φ_{AQY} for Pt$_{0.8}$Cu$_{0.2}$/anatase is much higher than that for Pt$_1$/anatase (white); the Φ_{AQY} for Pt$_{0.8}$Cu$_{0.2}$/anatase determined at 550 nm (17%) is more than twice that for Pt$_1$/anatase (7.1%).

As shown in **Figure 2-1**, visible light absorption of Pt promotes interband transition of e$^-$ from the 5d band to the sp conduction band.[18] The e$^-$ is transferred to the anatase conduction band, where the e$^-$ overcomes the Schottky barrier (ϕ_B) created at the heterojunction.[21] The enhanced e$^-$ transfer from photoactivated alloy particles to anatase is due to the decrease in the height of ϕ_B by Cu alloying. As shown by eq 1, ϕ_B is defined as the difference between the work function of alloy particles and the electron affinity of the anatase conduction band.[22] The work function of the bimetallic alloy is expressed by the sum of the work functions of two metal components.[23,24] The work function of bulk Pt$_{1-x}$Cu$_x$ alloy ($W_{alloy\infty}$) is expressed as follows:

$$W_{alloy\infty} \text{ (eV)} = (1-x) \times W_{Pt\infty} + x \times W_{Cu\infty} \qquad (2)$$

$W_{Pt\infty}$ and $W_{Cu\infty}$ are the work functions of bulk Pt (5.65 eV) and Cu (4.65 eV),[44] respectively. $W_{alloy\infty}$ for the bulk Pt$_{0.8}$Cu$_{0.2}$ alloy is therefore calculated to be 5.45 eV. As reported,[45] the work function of metal particles depends on their size (d). The work function of alloy particles (W_{alloy}) is expressed as follows:

$$W_{alloy} \text{ (eV)} = W_{alloy\infty} + \frac{1.08}{d} \qquad (3)$$

The average diameters of nanoparticles on Pt$_1$/anatase and Pt$_{0.8}$Cu$_{0.2}$/anatase are determined by TEM observations to be 3.3 and 3.4 nm, respectively. The W_{alloy} values for the nanoparticles on these catalysts are therefore calculated to be 5.98 and 5.77 eV, respectively. Smaller work function of the alloy particles indicates that alloying of Cu possessing a smaller work function decreases the height of ϕ_B. This thus promotes efficient e$^-$ transfer to anatase and results in higher photocatalytic activity of Pt$_{0.8}$Cu$_{0.2}$/anatase. At the metal/semiconductor heterojunction, Fermi level pinning usually occurs and makes the Schottky barrier height less sensitive to the work function of metal loaded.[46] It is, however, well-known that the pinning effect depends on the type and size of semiconductors. In particular, the size of TiO$_2$ particles strongly affects the pinning effect:[47,48] the effect scarcely occurs on the TiO$_2$ particles with small diameter (~60 nm) due to the high electronegativity of the Ti–O bond. The TiO$_2$ particles used in the present work are very small (average diameter, 21.1 nm). This implies that the Fermi level pinning may scarcely occur on the

present system. This therefore results in a decrease in the height of ϕ_B by the Cu alloying, thus facilitating the enhanced e$^-$ transfer from photoactivated alloy nanoparticles to anatase on the Pt$_{0.8}$Cu$_{0.2}$/anatase catalyst. In contrast, further increase in the Cu amount of nanoparticles would decrease the height of ϕ_B more significantly. In this case, interband excitation of 5d e$^-$ of Pt atoms is suppressed due to the decrease in Pt amount. This results in decreased efficiency for e$^-$ transfer to anatase (**Figure 2-9d**) and decreases photocatalytic activity (**Figure 2-7**).

The reaction mechanism on the PtCu/anatase catalyst is explained as **Figure 2-11**. As shown in **Figure 2-11A**, the dark reaction is initiated by activation of O$_2$ on the anionic Pt site (a).[49] The activated species removes the H atom from alcohol and produces hydroperoxide and alcoholate species on the surface (b).[50] Subsequent removal of the H atom from alcoholate species affords the product (c). Under irradiation of visible light (**Figure 2-11B**), photoactivated alloy particles transfer e$^-$ to anatase (d). In that, the height of the Schottky barrier created at the inter face is decreased by Cu alloying, thus promoting efficient e$^-$ transfer. The e$^-$ reduces O$_2$ and produces O$_2^-$ species on the anatase surface (e). The O$_2^-$ attracts the H atom from alcohol and produces the hydroperoxide and alcoholate species (f), giving rise to the product (g).
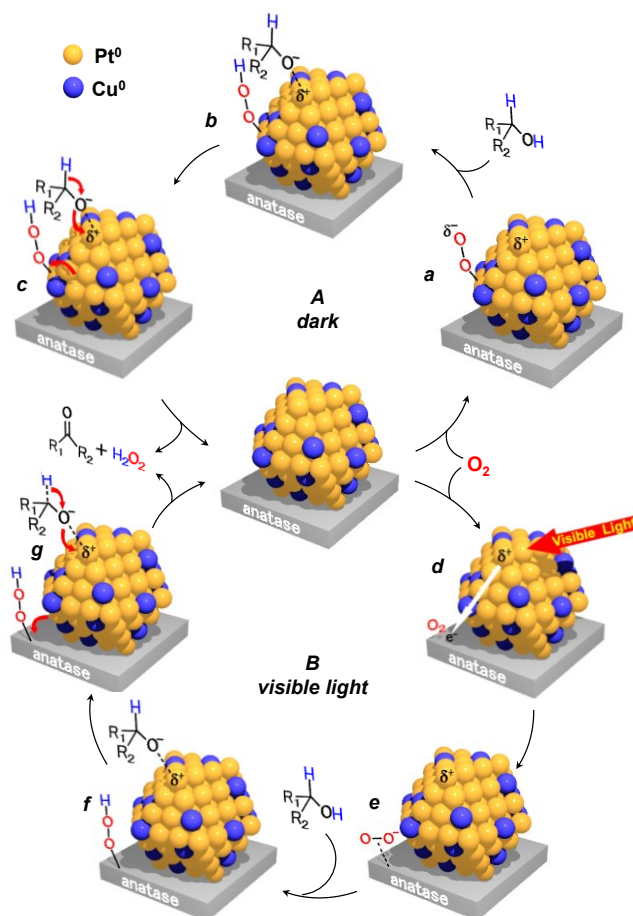
Figure 2-11. Proposed mechanism for aerobic oxidation of alcohol on the alloy catalyst (A) in the dark and (B) under visible light.
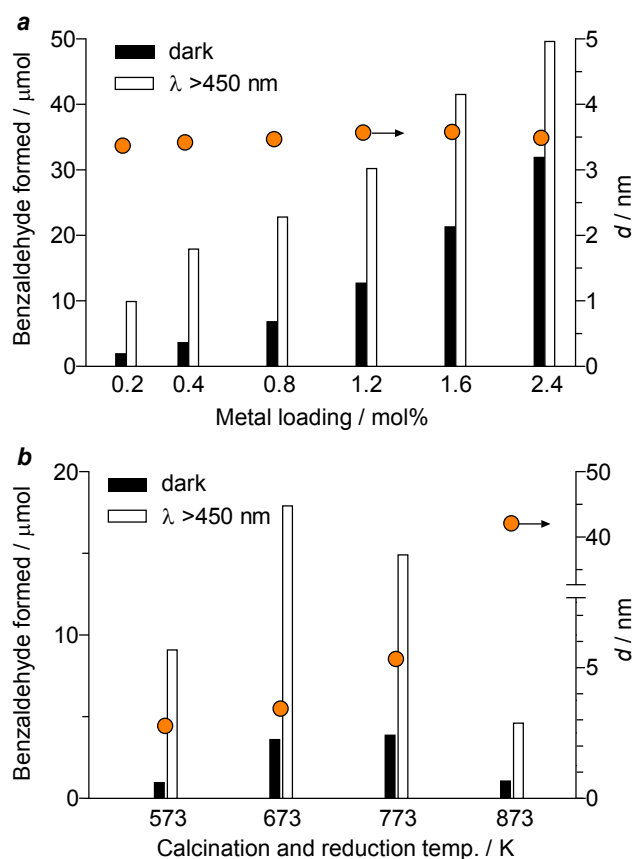
Figure 2-12. Effect of the (a) amount of $Pt_{0.8}Cu_{0.2}$ alloy particles loaded and (b) calcination and reduction temperature on the amount of benzaldehyde formed during aerobic oxidation of benzyl alcohol with $Pt_{0.8}Cu_{0.2}$/anatase catalysts, (black) in the dark and (white) under visible light irradiation. Orange keys denote the size of $Pt_{0.8}Cu_{0.2}$ alloy particles (d) on the catalysts. The calcination and reduction temperature employed for catalysts (a) is 673 K, and the metal loading of the catalysts (b) is 0.4 mol %. Reaction conditions are identical to those in **Figure 2-7**.

3-4. Effect of the Amount of Metal loaded

The activity of $Pt_{0.8}Cu_{0.2}$/anatase depends on the amount of metal loaded. This is confirmed by aerobic oxidation using the $Pt_{0.8}Cu_{0.2}$/anatase catalysts with different metal loadings [(Pt + Cu)/anatase × 100 = 0.2–2.4 mol %]. As shown in **Figure 2-12a** (orange), the particle sizes (d) of these catalysts are similar (3.4–3.6 nm), although the absorbance of catalysts in the visible region increases with the metal loadings (**Figure 2-13a**). The bar graphs in **Figure 2-12a** shows the results for aerobic oxidation of benzyl alcohol with respective catalysts. The dark activity (black) increases with the metal loadings due to the increase in the number of surface Pt atoms, active for aerobic oxidation.[51,52] Visible light irradiation (white) further enhances the reaction. The activity enhancement for the catalyst with 0.2 mol % of $Pt_{0.8}Cu_{0.2}$ alloy is low, but that for the catalysts with >0.4 mol % of $Pt_{0.8}Cu_{0.2}$ alloy is similar. This means that the >0.4 mol % of

metal loadings scarcely affects the activity enhancement by visible light irradiation, although a larger number of alloy nanoparticles are loaded on the surface. As reported,[53] the increase in the amount of metal loaded onto the semiconductor leads to an increase in ϕ_B, due to the decrease in the Fermi level of the semiconductor. The ϕ_B increase probably suppresses e$^-$ transfer from photoactivated nanoparticles to anatase, resulting in almost similar photocatalytic activity.
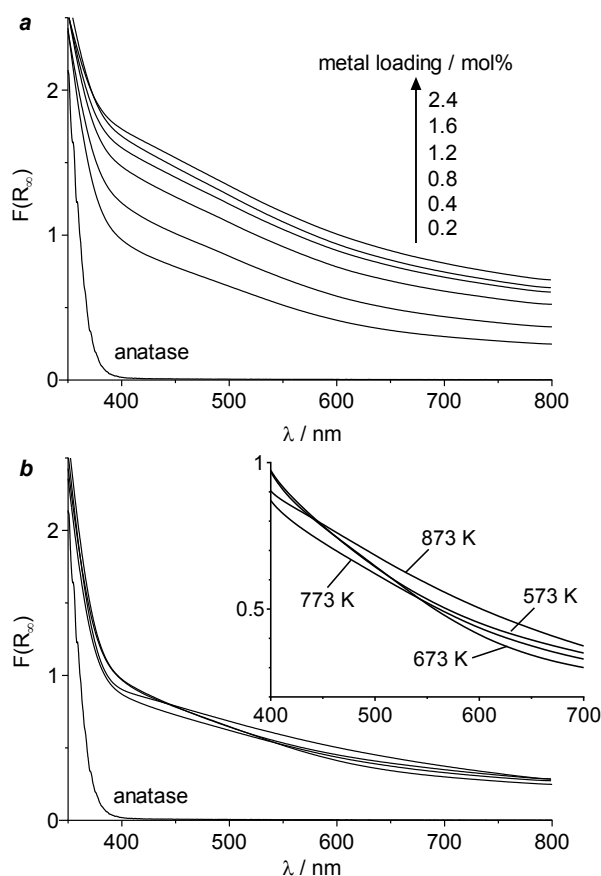
Figure 2-13. Diffuse-reflectance UV–vis spectra of (a) $Pt_{0.8}Cu_{0.2}$/anatase catalysts with different metal loadings prepared at 673 K and (b) $Pt_{0.8}Cu_{0.2}$/anatase catalysts with 0.4 mol % of metal loading prepared at different calcination and reduction temperature.

3-5. Effect of Particle Size

The size of $Pt_{0.8}Cu_{0.2}$ alloy particles (*d*) also affects the photocatalytic activity. The $Pt_{0.8}Cu_{0.2}$/anatase catalysts were prepared at different calcination and reduction temperatures (573–873 K) while maintaining 0.4 mol % of metal loading. As shown in **Figure 2-12b** (orange), *d* of the catalysts increases with a rise in temperature due to the sintering of nanoparticles; the treatment at 573, 673, 773, and 873 K creates metal particles with 2.8, 3.4, 5.3, and 42nmdiameters, respectively. X-ray diffraction (XRD) pattern of the

catalysts (**Figure 2-14**) indicates that the anatase-to-rutile phase transition scarcely occurs. In addition, dynamic laser scattering analysis of the catalysts revealed that the size of these catalysts is 22.4 nm (573 K), 23.8 nm (673 K), 23.9 nm (773 K), and 24.2 nm (873 K), respectively. This means that the size of anatase support is almost similar, although the size of alloy nanoparticles increases with a rise in temperature. As shown by the black bars in **Figure 2-12b**, in the dark conditions, the catalysts prepared at 673 and 773 K show relatively high activity, and the catalysts with smaller or larger particles show lower activity. The lower activity of smaller particles is due to the decreased density of low-coordination sites that are active for oxidation.[53] In contrast, larger particles contain a decreased number of surface Pt atoms and, hence, show decreased activity.

As shown by the white bars (**Figure 2-12b**), photocatalytic activity of $Pt_{0.8}Cu_{0.2}$/anatase prepared at different calcination and reduction temperature shows d dependence similar to the dark activity. The catalyst prepared at 673 K shows the highest activity, and the catalysts with smaller or larger particles show decreased activity. As shown in **Figure 2-13b**, absorbance of the catalysts in the visible region is similar, although their d values are different (**Figure 2-12b**). This indicates that the light absorption efficiencies for these catalysts are similar. The low activity of the catalysts with smaller Pt particles is due to the height of ϕ_B created at the nanoparticle/anatase interface. As shown by eq 3, the work function of metal particles increases with a decrease in their particle size. The d values for the catalysts prepared at 573, 673, 773, and 873 K are 2.8, 3.4, 5.3, and 42 nm, respectively, and their W_{alloy} values are calculated to be 5.84, 5.77, 5.65, and 5.48 eV, respectively. As summarized in **Figure 2-15**(black), the W_{alloy} values become more positive with a decrease in the particle size. This suggests that the catalysts with smaller Pt particles create higher ϕ_B. This may suppress smooth e⁻ transfer from photoactivated alloy particles to anatase, thus resulting in decreased photocatalytic activity (**Figure 2-12b**).
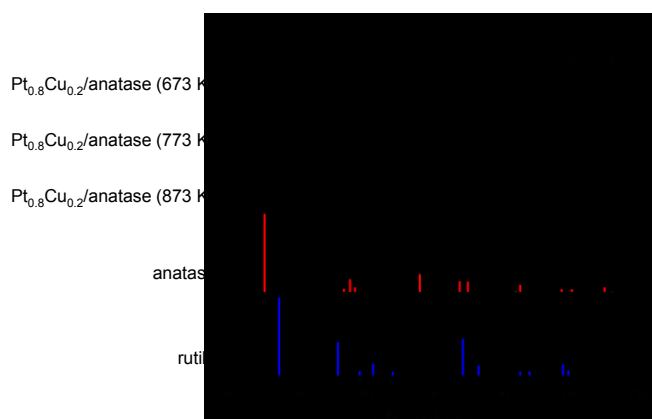
Figure 2-14. XRD patterns of respective catalysts and standard patterns for anatase (JCPDS 21-1272) and rutile (JCPDS 21-1276).
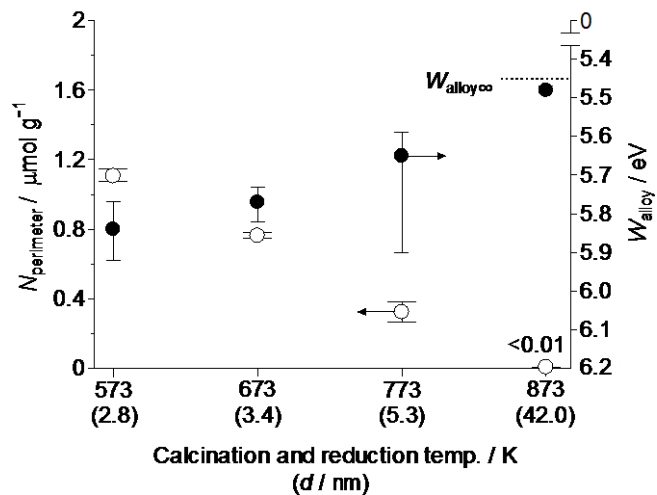
Figure 2-15. (Black) Work function of $Pt_{0.8}Cu_{0.2}$ alloy particles (W_{alloy}) and (white) the number of perimeter metal atoms ($N_{perimeter}$) for $Pt_{0.8}Cu_{0.2}$/anatase catalysts with 0.4 mol % of metal loading prepared at different calcination and reduction temperature. The detailed calculation results for $N_{perimeter}$ are summarized in **Table 2-1**.
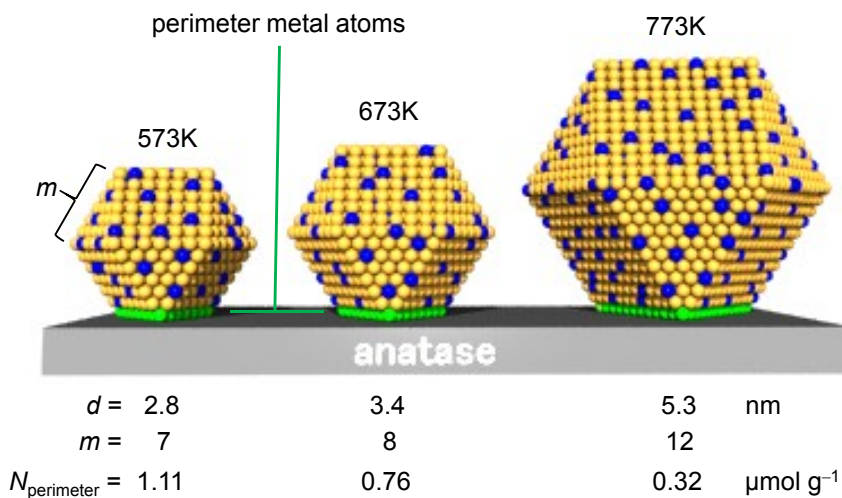
Figure 2-16. Rerationship between the size of metal particles and the number of perimeter metal atoms on $Pt_{0.8}Cu_{0.2}$/anatase catalysts prepared at different calcination and reduction temperature.

Table 2-1. Properties of $Pt_{0.8}Cu_{0.2}$/anatase catalysts prepared at different calcination and reduction temperature.

Temperature	d / nm [a]	N_{total} [b]	m [c]	$N_{perimeter}$* [d]	$N_{particle}$ / μmol g^{-1} [e]	$N_{perimeter}$ / μmol g^{-1} [f]
573 K	2.8 ± 0.5	$(7.94 \pm 0.50) \times 10^2$	6.68 ± 0.10	$(1.70 \pm 0.03) \times 10$	$(6.50 \pm 0.39) \times 10^{-2}$	1.11 ± 0.04
673 K	3.4 ± 0.5	$(1.42 \pm 0.06) \times 10^3$	8.01 ± 0.10	$(2.10 \pm 0.03) \times 10$	$(3.62 \pm 0.13) \times 10^{-2}$	$(7.62 \pm 0.18) \times 10^{-1}$
773 K	5.3 ± 2.9	$(5.39 \pm 1.61) \times 10^3$	$(1.22 \pm 0.06) \times 10$	$(3.37 \pm 0.17) \times 10$	$(9.57 \pm 5.74) \times 10^{-3}$	$(3.22 \pm 0.57) \times 10^{-1}$
873 K	42 ± 8.7	$(2.68 \pm 0.16) \times 10^6$	$(9.35 \pm 0.18) \times 10$	$(2.78 \pm 0.05) \times 10^2$	$(1.92 \pm 0.27) \times 10^{-5}$	$(5.33 \pm 0.35) \times 10^{-3}$

[a] Average diameter of metal particles determined by TEM observations. [b] The number of total metal atoms per particle. [c] The munber of shells. [d] The number of perimeter metal atoms per particle. [e] The number of metal particles per gram catalyst. [f] The number of perimeter metal atoms per gram catalyst.

In contrast, larger alloy particles create lower ϕ_B due to their lower work function; therefore, the e^- transfer to anatase would occur more easily. However, as shown in **Figure 2-12b**, photocatalytic activity of the catalysts with larger alloy particles is much lower than that prepared at 673 K. As shown in **Figure 2-16**, the e^- transfer from photoactivated metal particles to anatase occurs through the perimeter atoms indicated by the green spheres.[19] The number of perimeter metal atoms may therefore affect the e^- transfer efficiency. As shown in **Figure 2-2c–h**, the high-resolution TEM images of catalysts revealed that the shape of many alloy particles is a part of a cuboctahedron, which is surrounded by (111) and (100) surfaces. The PtCu alloy particles on the anatase surface therefore can simply be modeled as a *fcc* cuboctahedron,[55] as often used for related systems.[56,57] This thus allows rough determination of the number of perimeter metal atoms. Considering the full shell close-packing cuboctahedron for the PtCu alloy particle, where one atom is surrounded by 12 others, the number of total metal atoms per particle (N_{total}*) can be expressed by eq 4 using the number of shells (m). N_{total}* is rewritten with the average diameter of alloy particle (d) and the average atomic diameter of Pt and Cu [d_{atom} (= 0.274 nm) = 0.8 $\times$ $d_{atom,Pt}$ (=0.278 nm) + 0.2 $\times$ $d_{atom,Cu}$ (=0.256 nm)].[57] The number of perimeter atoms per particle ($N_{perimeter}$*) is expressed by eq 5.[55]

$$N_{total}*(-)=\frac{10m^3\text{-}15m^2+11m\text{-}3}{3}=\left(\frac{d}{1.105\times d_{atom}}\right)^3 \qquad (4)$$

$$N_{perimeter}*(-)=3m\text{-}3 \qquad (5)$$

The number of alloy particles per gram catalyst ($N_{particle}$) is expressed by eq 6, using the percent amount of metal loaded [0.87 wt % = (Pt + Cu)/(Pt + Cu + anatase) $\times$ 100], average molecular weight of Pt and Cu [M_W (= 168.8 g mol^{-1}) = 0.8 $\times$ M_{Pt} (= 195.1 g mol^{-1}) + 0.2 $\times$ M_{Cu} (= 63.5 g mol^{-1})], and N_{total}*. The number of perimeter metal atoms per gram catalyst ($N_{perimeter}$) is therefore expressed by eq 7.
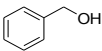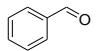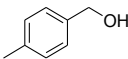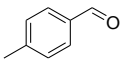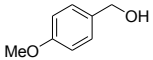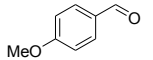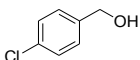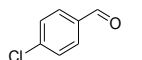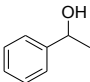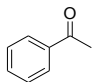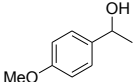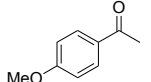
$$N_{particle}\,(\text{mol g}^{-1})=\frac{0.87}{100\times M_W\times N_{total}*} \qquad (6)$$

$$N_{perimeter}\,(\text{mol g}^{-1})=N_{perimeter}*\times N_{particle} \qquad (7)$$

The $N_{perimeter}$ values for respective $Pt_{0.8}Cu_{0.2}$/anatase catalysts prepared at different temperature can therefore be calculated using their d values determined by TEM observations (**Table 2-1**). As shown in **Figure 2-15** (white), $N_{perimeter}$ decreases with an increase in the particle size; the value for the catalyst prepared at 573 K is 1.1 μmol g^{-1}, but the value for the catalyst prepared at 873 K is only 5.3 $\times$ 10^{-3} μmol g^{-1}. This suggests that the particle size increase significantly decreases $N_{perimeter}$. This may suppress e^- transfer from photoactivated alloy particles to anatase, resulting in low photocatalytic activity. As shown in Figure 6b, the

catalysts prepared at 573, 673, and 773 K contain alloy particles with similar diameter (2–6 nm), but the catalyst prepared at 673 K shows the highest photocatalytic activity. This means that the particle size strongly affects W_{alloy} and $N_{perimeter}$ values, and this trade-off relationship is critical for activity. The 3–5 nm $Pt_{0.8}Cu_{0.2}$ alloy nanoparticles with shell number 7–11 create relatively low ϕ_B and large number of perimeter metal atoms at the nanoparticle/anatase heterojunction and, hence, exhibit high photocatalytic activity.

Table 2-2. Effect of Sunlight Exposure on Aerobic Oxidation of Alcohols with Respective Catalysts[a]

entry	substrate	catalyst	sunlight[b]	conversion / %[c]	product	yield / %[d]
1		$Pt_{0.8}Cu_{0.2}$/anatase	+	75		72
2		$Pt_{0.8}Cu_{0.2}$/anatase	–	13		12
3		Pt_1/anatase	+	37		35
4		$Pt_{0.8}Cu_{0.2}$/anatase	+	84		80
5		$Pt_{0.8}Cu_{0.2}$/anatase	–	9		9
6		Pt_1/anatase	+	60		59
7		$Pt_{0.8}Cu_{0.2}$/anatase	+	>99		99
8		$Pt_{0.8}Cu_{0.2}$/anatase	–	14		14
9		Pt_1/anatase	+	77		77
10		$Pt_{0.8}Cu_{0.2}$/anatase	+	73		73
11		$Pt_{0.8}Cu_{0.2}$/anatase	–	7		7
12		Pt_1/anatase	+	43		40
13		$Pt_{0.8}Cu_{0.2}$/anatase	+	72		72
14		$Pt_{0.8}Cu_{0.2}$/anatase	–	11		10
15		Pt_1/anatase	+	34		34
16		$Pt_{0.8}Cu_{0.2}$/anatase	+	85		84
17		$Pt_{0.8}Cu_{0.2}$/anatase	–	5		5
18		Pt_1/anatase	+	49		49

[a] Reaction conditions: toluene (5 mL), alcohol (25 μmol), catalyst (5 mg), O_2 (1 atm), exposure time (4 h). The average light intensity at 300–800 nm was 8.1 mW cm^{-2}, which involves λ <400 nm light with only ca. 2% (see **Figure 2-17**). The solution temperature during exposure was 288–293 K. [b] The dark reaction (−) was performed at 293 K. [c] = (alcohol converted) / (initial amount of alcohol) × 100. [d] = (product formed) / (initial amount of alcohol) × 100.

3-6. Effect of Sunlight as the Light Source

The $Pt_{0.8}Cu_{0.2}$/anatase catalyst prepared at 673 K successfully promotes aerobic oxidation of alcohols

under sunlight irradiation at ambient temperature. **Table 2-2** summarizes the results for oxidation of various alcohols obtained with $Pt_{0.8}Cu_{0.2}$/anatase under sunlight exposure, where the temperature of solution during exposure was 288–293 K. Sunlight irradiation selectively oxidizes alcohols to the corresponding carbonyl compounds with very high yields (75–99%).
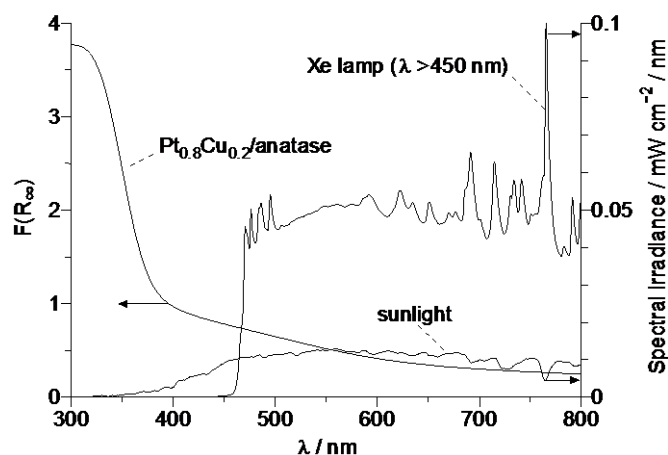
Figure 2-17. Light emission spectra for Xe lamp (λ >450 nm) and sunlight, and diffuse reflectance UV-vis spectra of $Pt_{0.8}Cu_{0.2(673)}$/anatase catalyst.

4. Conclusion

The author found that bimetallic alloy nanoparticles consisting of 80 mol % of Pt and 20 mol % of Cu, supported on anatase TiO_2, behave as highly efficient photocatalysts for aerobic oxidation under visible light irradiation. The activity of the alloy catalyst is much higher than that of the monometallic Pt catalyst. The enhanced activity is due to the decrease in the work function of nanoparticles by Cu alloying. This decreases the height of the Schottky barrier created at the nanoparticle/anatase heterojunction and promotes smooth e^- transfer from the photoactivated nanoparticles to anatase. The activity strongly depends on the size of alloy particles. Smaller particles (<3 nm diameter) have larger work function and create a larger Schottky barrier, resulting in decreased activity. In contrast, larger particles (>5 nm diameter) possess a smaller number of perimeter metal atoms. This thus suppresses smooth e^- transfer from photoactivated nanoparticles to anatase, resulting in decreased activity. As a result of this, alloy nanoparticles with 3–5 nm diameters exhibit the highest photocatalytic activity. Sunlight activation of the catalyst successfully promotes selective and efficient oxidation of alcohols. The efficient charge separation at the Pt–Cu alloy nanoparticle/anatase interface clarified here may contribute to the creation of more active photocatalysts driven by visible light and the design of photocatalytic systems for selective organic transformation by sunlight.

5. References

[1]   Sheldon, R. A.; Arends, I. W. C. E.; Dijksman, A. *Catal. Today* **2000**, *57*, 157–166.

[2]   Fox, M. A.; Dulay, M. T. *Chem. Rev.* **1993**, *93*, 341–357.

[3]   Maldotti, A.; Molinari, A.; Amadelli, R. *Chem. Rev.* **2002**, *102*, 3811–3836.

[4]   Palmisano, G.; Augugliaro, V.; Pagliano, M.; Palmisano, L. *Chem. Commun.* **2007**, 3425–3437.

[5]   Fagnoni, M.; Dondi, D.; Ravelli, D.; Albini, A. *Chem. Rev.* **2007**, *107*, 2725–2756.

[6]   Shiraishi, Y.; Hirai, T. *J. Photochem. Photobiol. C* **2008**, *9*, 157–170.

[7]   Asahi, R.; Morikawa, T.; Ohwaki, T.; Aoki, T.; Taga, K. Y. *Science* **2001**, *293*, 269-271.

[8]   Miyauchi, M.; Ikezawa, A.; Tobimatsu, H.; Irie, H.; Hashimoto, K. *Phys. Chem. Chem. Phys.* **2004**, *6*, 865-870.

[9]   Ohno, T.; Akiyoshi, M.; Umebayashi, T.; Asai, K.; Mitsui, T.; Matsumura, M. *Appl. Catal. A* **2004**, *265*, 115-121.

[10] Yan, X.; Ohno, T.; Nishijima, K.; Abe, R.; Ohtani, B. *Chem. Phys. Lett.* **2006**, *429*, 606-610.

[11] Sakthivel, S.; Kisch, H. *Angew. Chem., Int. Ed.* **2003**, *42*, 4908-4911.

[12] Irie, H.; Watanabe, Y.; Hashimoto, K. *Chem. Lett.* **2003**, *32*, 772-773.

[13] Zhao, W.; Ma, W.; Chen, C.; Zhao, J.; Shuai, Z. *J. Am. Chem. Soc.* **2004**, *126*, 4782-4783.

[14] Zaleska, A.; Sobczak, J. W.; Grabowska, E.; Hupka, J. *Appl. Catal. B* **2008**, *78*, 92-100.

[15] Chen, X.; Mao, S. S. *Chem. Rev.* **2007**, *107*, 2891-2959.

[16] Primo, A.; Corma, A.; García, H. *Phys. Chem. Chem. Phys.* **2011**, *13*, 886–910.

[17] Tsukamoto, D.; Shiraishi, Y.; Sugano, Y.; Ichikawa, S.; Tanaka, S.; Hirai, T. *J. Am. Chem. Soc.* **2012**, *134*, 6309–6315.

[18] Hao, Q.; Juluri, B. K.; Zheng, Y. B.; Wang, B.; Chiang, I.-K.; Jensen, L.; Crespi, V.; Eklund, P. C.; Huang, T. J. *J. Phys. Chem. C* **2010**, *114*, 18059–18066.

[19] Shiraishi, Y.; Tsukamoto, D.; Sugano, Y.; Shiro, A.; Ichikawa, S.; Tanaka, S.; Hirai, T. *ACS Catal.* **2012**, *2*, 1984-1992.

[20] Gong, X.-Q.; Slloni, A.; Dulub, O.; Jacobson, P.; Diebold, U. *J. Am. Chem. Soc.* **2008**, *130, 370-381*.

[21] Schottky, W. Z. *Phys.* **1939**, *113, 367-414*.

[22] Nakato, Y.; Ueda, K.; Yano, H.; Tsubomura, H. *J. Phys. Chem.* **1988**, *92*, 2316−2324.

[23] Pasti, I.; Mentus, S. *Mater. Chem. Phys.* **2009**, *116*, 94-101.

[24] Ishii, R.; Matsumura, K.; Sakai, A.; Sakata, T. *Appl. Surf. Sci.* **2001**, *169-170*, 658-661.

[25] Sugano, Y.; Shiraishi, Y.; Tsukamoto, D.; Ichikawa, S.; Tanaka, S.; Hirai, T. *Angew. Chem., Int. Ed.* **2013**, *52*, 5295-5299.

[26] Shiraishi, Y.; Tanaka, K.; Shirakawa, E.; Sugano, Y.; Ichikawa, S.; Tanaka, S.; Hirai, T. *Angew. Chem., Int. Ed.* **2013**, *52*, 8304-8308.

[27] Shiraishi, Y.; Ikeda, M.; Tsukamoto, D.; Tanaka, S.; Hirai, T. *Chem. Commun.* **2011**, *47*, 4811-4813.

[28] Shiraishi, Y.; Takeda, Y.; Sugano, Y.; Ichikawa, S.; Tanaka, S.; Hirai, T. *Chem. Commun.* **2011**, *47*, 7863-7865.

[29] Li, L.; Xu, Z.; Liu, F.; Shao, Y.; Wang, J.; Wan, H.; Zheng, S. *J. Photochem. Photobiol. A* **2010**, *212*, 113-121.

[30] Zhang, J.; Ma, J.; Wan, Y.; Jiang, J.; Zhao, X. S. *Meter. Chem. Phys.* **2012**, *132*, 244-247.

[31] Kleiman, G. G.; Sundaram, V. S.; Rogers, J. D.; Moraes, M. B. *Phys. Rev. B* **1981**, *23*, 3177-3185.

[32] Barrabés, N.; Frare, A.; Föttonger, K.; Urakawa, A.; Llorca, J.; Rupprechter, G.; Tichit, D. *Appl. Clay Sci.* **2012**, *69*, 1-10.

[33] Bigall, N. C.; Härtling, T.; Klose, M.; Simon, P.; Eng, L. M.; Eychmüller, A. *Nano Lett.* **2008**, *8*, 4588-4592.

[34] Desarkar, H. S.; Kumbhakar, P.; Mitra, A. K. *Appl. Nanosci.* **2012**, *2*, 285-291.

[35] Pileni, M. P.; Lisiecki, I.; *Colloids Surf. A* **1993**, *80, 63-68.*

[36] Abad, A.; Corma, A.; Garcia, H. *Chem. Eur. J.* **2008**, *14*, 212–222.

[37] Proch, S.; Herrmannsdörfer, J.; Kempe, R.; Kern, C.; Jess, A.; Seyfarth, L.; Senker, J. *Chem. Eur. J.* **2008**, *14*, 8204–8212.

[38] Ng, Y. H.; Ikeda, S.; Harada, T.; Morita, Y.; Matsumura, M. *Chem. Commun.* **2008**, 3181–3183.

[39] Zhang, H.; Toshima, N. *J. Colloid Interface Sci.* **2013**, *394*, 166-176.

[40] Hwang, B. J.; Kumar, S. M. S.; Chen, C.-H.; Chang, R.-W.; Liu, D.-G.; Lee, J.-F. *J. Phys. Chem. C* **2008**, *112*, 2370-2377.

[41] Lapisardi, G.; Urfels, L.; Gélin, P.; Primet, M.; Kaddouri, A.; Garbowski, E.; Toppi, S.; Tena, E. *Catal. Today* **2006**, *117*, 564-568.

[42] Coronado, J. M.; Soria, J. *Catal. Today* **2007**, *123*, 37–41.

[43] Anpo, M.; Che, M.; Fubini, B.; Garrone, E.; Giamello, E.; Paganini, M. C. *Top. Catal.* **1999**, *8*, 189–198.

[44] Eastman, D. E. *Phys. Rev. B.* **1970**, 2, 1-2.

[45] Wood, D. M. *Phys. Rev. Lett.* **1981**, *46*, 749–749.

[46] Bardeen, J. *Phys. Rev. B.* **1970**, *2*, 1–2.

[47] Malagu, C.; Guidi, V.; Stefancich, M.; Carotta, M. C.; Martinelli, G. *J. Appl. Phys.* **2002**, *91*, 808.

[48] Malagu, C.; Guidi, V.; Carotta, M. C.; Martinelli, G. *Appl. Phys. Lett.* **2004**, *84*, 4158.

[49] Ishida, T.; Nagaoka, M.; Akita, T.; Haruta, M. *Chem.–Eur. J.* **2008***, 14, 8456-8460.*

[50] Fukuto, J. M.; Di Stefano, E. W.; Burstyn, J. N.; Valentine, J. S.; Cho, A. K. *Biochemistry* **1985**, *24, 4161-4167.*

[51] Yamamoto, T. A.; Nakagawa, T.; Seino, S.; Nitani, H. *Appl. Catal. A* **2010**, *387*, 195-202.

[52] Liang, D.; Gao, J.; Wang, J.; Chen, P.; Wei, Y.; Hou, Z. *Catal. Commun.* **2011**, *12*, 1059-1062.

[53] Uchihara, T.; Matsumura, M.; Yamamoto, A.; Tsubomura, H. *J. Phys. Chem.* **1989**, *93*, 5870-5874.

[54] Liu, Y.; Tsunoyama, H.; Akita, T.; Xie, S.; Tsukuda, T. *ACS Catal.* **2011**, *1, 2-6.*

[55] Benfield, R. E. *J. Chem. Soc. Faraday Trans.* **1992**, *88, 1107-1110.*

[56] Arruda, T. M.; Shyam, B.; Ziegelbauer, J. M.; Mukerjee, S.; Ramaker, D. E. *J. Phys. Chem. C* **2008**, *112, 18087-18097.*

[57] Wilson, O. M.; Knecht, M. R.; Garcia-Marthinez, J. C.; Crooks, R. M. *J. Am. Chem. Soc.* **2006**, *128, 4510-4511.*

[58] Murthi, V. S.; Urian, R. C.; Mukerjee, S. *J. Phys. Chem. B* **2004**, *108*, 11011–11023.

Chapter III

Direct O₂ Activation by Pt Nanoparticles Supported on Ta₂O₅

1. Introduction

Aerobic oxidation by heterogeneous catalysts with O_2 as an oxidant is an essential reaction for organic synthesis from the viewpoint of green and sustainable chemistry.[1] Photocatalytic oxidation with O_2 has also been studied extensively with semiconductor TiO_2,[2−6] because it oxidizes several types of substrates such as alcohols, amines, hydrocarbons, and sulfides at room temperature. One critical issue for practical application of the photocatalytic processes is the low catalytic activity under irradiation of visible light ($\lambda > 400$ nm), the main component of solar irradiance. Several TiO_2 materials doped with nitrogen,[7,8] sulfur,[9,10] carbon,[11,12] or boron atoms[13,14] have been proposed to extend the absorption edge into the visible region. All of these doped catalysts, however, suffer from low quantum yields for the reaction (<0.5%), because they inherently contain a large number of crystalline lattices that behave as charge recombination centers.[15] The creation of visible-light-driven-photocatalysts that efficiently promote aerobic oxidation is still a challenge.

A metal particles/semiconductor system, driven by an absorption of visible light by metal particles,[16] is one of the promising photocatalysts for aerobic oxidation. As shown in **Figure 3-1**, Au[17−24] or Pt particles[25−28] supported on semiconductors such as TiO_2, CeO_2, ZrO_2, and $SrTiO_3$ absorb visible light and produce hot electrons (e_{hot}^-) via an intra- or interband transition of 6sp or 5d band electrons.[29−31] These e_{hot}^- are injected into the semiconductor conduction band (CB) through the metal/semiconductor interface. The positive charges (hot holes, δ^+) formed on the metal oxidize substrates, while the CB electrons (e_{CB}^-) are consumed by the reduction of O_2, promoting aerobic oxidation even at room temperature. The quantum yields for the reactions are, however, <5% (at 550 nm), although much higher than those obtained by the doped catalysts (<0.5%).[7−14] The rate-determining step is the injection of e_{hot}^- into the semiconductor CB because it requires the energy to overcome the Schottky barrier (ϕ_B) created at the metal/semiconductor interface.[32,33] Development of a new catalyst that promotes the reaction without e_{hot}^- injection is therefore a key to efficient aerobic oxidation.

Recently, some metal absorption systems that promote reactions on the metal particles "without e_{hot}^- injection" have been proposed.[34] Laser photoexcitation ($\lambda \geq 450$ nm) of Au particles (ca. 10−20 nm) supported on SiO_2 promotes H_2 dissociation ($H_2 + D_2 \rightarrow 2HD$) at room temperature by the e_{hot}^- photoformed on the Au particles.[35] In that, a TiO_2 support is less effective because the e_{hot}^- injection into the TiO_2 CB decreases the number of e_{hot}^- on the Au particles.[36] Aerobic oxidation of carbon monoxide (CO) is promoted

on Pt particles (ca. 2−3 nm) supported on α-Al$_2$O$_3$ under visible light irradiation by a Xe lamp with relatively high quantum yield (ca. 5% at 550 nm).[37] The reaction is promoted by photoexcitation of CO molecules adsorbed on the Pt surface. In that, a high temperature (>373 K) is necessary for high catalytic activity. Aerobic oxidation of ethylene (C$_2$H$_4$ + 1/2O$_2$ → C$_2$H$_4$O) is promoted on Ag nanocubes (75 nm edge length) supported on α-Al$_2$O$_3$ by visible light irradiation with a Xe lamp.[38,39] It is considered that, based on ab initio calculation by density functional theory (DFT), the reaction occurs via a donation of e$_{hot}^-$ to O$_2$ adsorbed on the Ag surface. The formed anionic oxygen species are proposed to be the active species for oxidation, although the species are not detected directly. The Ag/α-Al$_2$O$_3$ system promotes the reaction with very high quantum yield (ca. 60% at 380−800 nm) but needs high reaction temperature (>373 K). This is probably because vibrational activation (dissociation) of the active oxygen species by thermal stimuli is required for oxidation.[40] The design of a visible-light-driven metal particle system that promotes aerobic oxidation at room temperature is therefore still a challenge.
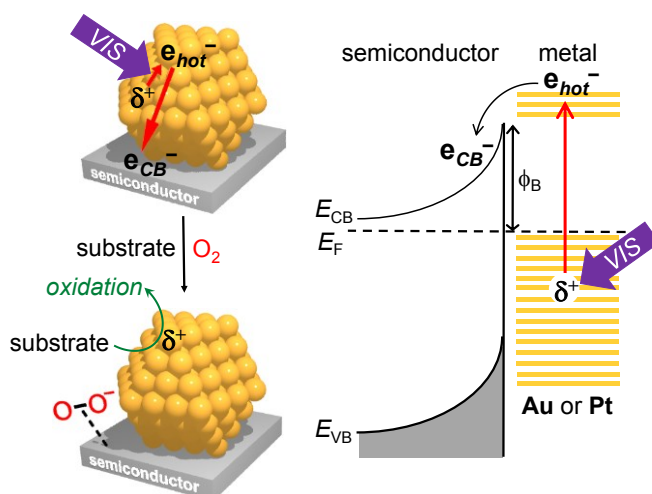
Figure 3-1. Aerobic Oxidation on a Metal/Semiconductor System under Irradiation of Visible Light. Where E_F and ϕ_B [$= W - \chi$ (eV)] are the Fermi level and the height of Schottky barrier, respectively [W = work function of metal (eV); χ = electron affinity of semiconductor CB (eV)].

Herein, we report that visible-light-induced aerobic oxidation at room temperature is facilitated by Pt nanoparticles (~5 nm diameter) supported on semiconductor Ta$_2$O$_5$. These Pt nanoparticles possess very high electron density due to the strong Pt−Ta$_2$O$_5$ interaction. This enhances interband transition of the Pt 5d electrons by absorbing visible light. A large number of e$_{hot}^-$ produced on the photoactivated Pt surface directly activate O$_2$ and create active peroxide species for oxidation. The formation of the species was

detected by spectroscopic analysis. The Pt/Ta_2O_5 catalysts successfully promote aerobic oxidation of alcohols with significantly high quantum yield, ~25% (at 550 nm).

2. Experimental section

2-1. General

All of the reagents used were supplied from Wako, Tokyo Kasei, and Sigma-Aldrich and used without further purification. Water was purified by the Milli Q system. Ta_2O_5 and $SrTiO_3$ were purchased from Wako. TiO_2 (JRC-TIO-1 and JRC-TIO-4), ZrO_2 (JRC-ZRO-3), and CeO_2 (JRC-CEO-3) were kindly supplied from the Catalyst Society of Japan (Japan Reference Catalyst). These properties are summarized in **Table 3-1**.

Table 3-1. Properties of semiconductors used

Semiconductor	Supplier	Average particle size / nm [a]	S_{BET} / m^2 g^{-1} [b]	pzc / pH [c]
Ta_2O_5	Wako	1269	2.6	3.3
TiO_2 (JRC-TIO-1)	Catalysis Society of Japan	21	81	5.0
P25 TiO_2 (JRC-TIO-4)	Catalysis Society of Japan	24	57	6.0
ZrO_2 (JRC-ZRO-3)	Catalysis Society of Japan	107	94	3.4
CeO_2 (JRC-CEO-3)	Catalysis Society of Japan	20	82	6.6
$SrTiO_3$	Wako	222	10	

[a] Hydrodynamic diameter determined by a Horiba LB–500 dynamic light scattering particle size analyzer. [b] BET surface area determined by N_2 adsorption/desorption measurements at 77 K using an AUTOSORB–1–C/TCD analyzer (Yuasa Ionics Co., Ltd.). [c] Point of zero charge for the catalysts determined by Zeta potential measurements on an ELSZ-1000Z analyzer (Otsuka Electronics Co., Ltd.).

2-2. Catalyst Preparation

Pt_x/Ta_2O_5 [x (wt %) = $Pt/Ta_2O_5 \times 100$; x = 0.5, 1, 1.5, 2, 2.5, or 3] were prepared as follows: Ta_2O_5 (1 g) was added to water (40 mL) containing $H_2PtCl_6 \cdot 6H_2O$ (13.3, 26.8, 40.4, 54.2, 68.1, or 82.1 mg). The solvents were removed by evaporation at 353 K with vigorous stirring for 12 h. The obtained powders were dried under air flow and reduced under H_2 flow at the identical temperature. Unless otherwise noted, the H_2 reduction was carried out at 673 K. The heating rate was 2 K min^{-1}, and the holding time at the designated temperature was 2 h, respectively. Pt_2/TiO_2 (JRC-TIO-1), Pt/CeO_2, Pt_2/ZrO_2, and $Pt_2/SrTiO_3$ were prepared in a similar manner to that of Pt_2/Ta_2O_5. Ag_2/Ta_2O_5 and Pd_2/Ta_2O_5 were also prepared in a similar manner, with $AgNO_3$ (32 mg) or $Pd(NO_3)_2$ (44 mg) as a metal source.

66

Au$_2$/Ta$_2$O$_5$ and Au$_2$/TiO$_2$ were prepared by a deposition−precipitation method.[19] Ta$_2$O$_5$ or TiO$_2$ (JRC-TIO-4, 1 g) was added to water (50 mL) containing HAuCl$_4$·4H$_2$O (46 mg). The pH of the solution was adjusted to ~7 with 1 mM NaOH, and the solution was stirred at 353 K for 3 h. The particles were recovered by centrifugation, washed thoroughly with water, and dried at 353 K for 12 h. The powders were calcined under air flow, where the heating rate was 2 K min^{-1} and the holding time at 673 K was 2 h, respectively.

2-3. Photoreaction

Catalyst (10 mg) was added to 2-PrOH (5 mL) within a Pyrex glass tube (φ 12 mm; capacity, 20 mL). The tube was sealed with a rubber septum cap. The catalyst was dispersed well by ultrasonication for 5 min, and O$_2$ was bubbled through the solution for 5 min. The tube with an O$_2$ balloon was immersed in a temperature-controlled water bath, and the temperatures of the solutions were kept rigorously at the designated temperature (deviation: ±0.5 K).[19] The tube was photoirradiated with magnetic stirring using a 2 kW Xe lamp (USHIO Inc., λ >300 nm). The light intensity at 300−800 nm was 21.0 mW cm^{-2}. A glass filter (CS3-72; Kopp Glass Inc.) was used to give light wavelength at λ >450 nm, where the light intensity at 450−800 nm was 16.8 mW cm^{-2}. After photoreaction, the catalyst was recovered by centrifugation, and the resulting solution was analyzed by GC-FID (Shimadzu, GC-1700).

2-4. Action Spectrum Analysis

Catalyst (8 mg) was suspended in 2-PrOH (2 mL) within a Pyrex glass tube (φ 12 mm; capacity, 20 mL). The tube was sealed with a rubber septum cap. The catalyst was dispersed well by ultrasonication for 5 min, and O$_2$ was bubbled through the solution for 5 min. The tube with an O$_2$ balloon was photoirradiated with magnetic stirring by a 2 kW Xe lamp (USHIO Inc.), where the incident light was monochromated by band-pass glass filters (Asahi Techno Glass Co.).[23] The full-width at half-maximum (fwhm) of the lights was 11−16 nm. The temperature of the solutions during photoirradiation was kept at 298 ± 0.5 K in a temperature-controlled water bath. The photon number entered into the reaction vessel was determined with a spectroradiometer (USR-40; USHIO Inc.).

2-5. ESR Measurement

ESR spectra were recorded at the X-band using a Bruker EMX-10/12 spectrometer with a 100 kHz magnetic field modulation at a microwave power level of 10.0 mW, where microwave power saturation of the signal does not occur.[27] The magnetic field was calibrated with 1,1′-diphenyl-2-picrylhydrazyl (DPPH).

Catalyst (10 mg) was placed in a quartz ESR tube and evacuated at 423 K for 3 h. After cooling the tube to room temperature, O_2 (20 Torr) was introduced to the tube and left for 3 h at 298 K in the dark or under photoirradiation using a Xe lamp (2 kW; USHIO Inc.) at λ >450 nm (with CS3-72; Kopp Glass Inc.). The ESR tube was then evacuated for 10 min to remove the excess amount of O_2 and subjected to analysis at 77 K.

2-6. DRIFT Analysis

The spectra were measured on a FT/IR-610 system (JASCP Corp.),[78] equipped with an in situ DR cell (Heat Chamber HC-500, ST Japan, Inc.). The catalyst (20 mg) was placed in the DR cell, and the cell was evacuated ($6.8 \times 10{-3}$ Torr) at 423 K for 3 h. O_2 or CO (1.5 Torr) was introduced to the cell at the designated temperature. The cell was left at the temperature for 3 h in the dark or under irradiation of 450 nm monochromatic light with a Xe lamp (300 W; Asahi Spectra Co. Ltd.; Max-302) equipped with 450 nm bandpass filter. The fwhm of the light was 10 nm, and the light intensity was 68 μW cm^{-2}, respectively. The cell was then evacuated for 10 min to remove the excess amount of O_2 or CO and subjected to analysis at 303 K.

2-7. Other Analysis

TEM observations were performed on a FEI Tecnai G2 20ST analytical electron microscope operated at 200 kV.[79] XRD patterns were measured on a Philips X′Pert-MPD spectrometer. XPS measurements were performed using a JEOL JPS9000MX spectrometer with Mg Kα radiation as the energy source. C 1s binding energy at 284.8 eV was used as a reference for the calibration of XPS lines.[80] Diffuse-reflectance UV−vis spectra were measured on an UV−vis spectrometer (Jasco Corp.; V-550 with Integrated Sphere Apparatus ISV-469) with $BaSO_4$ as a reference.
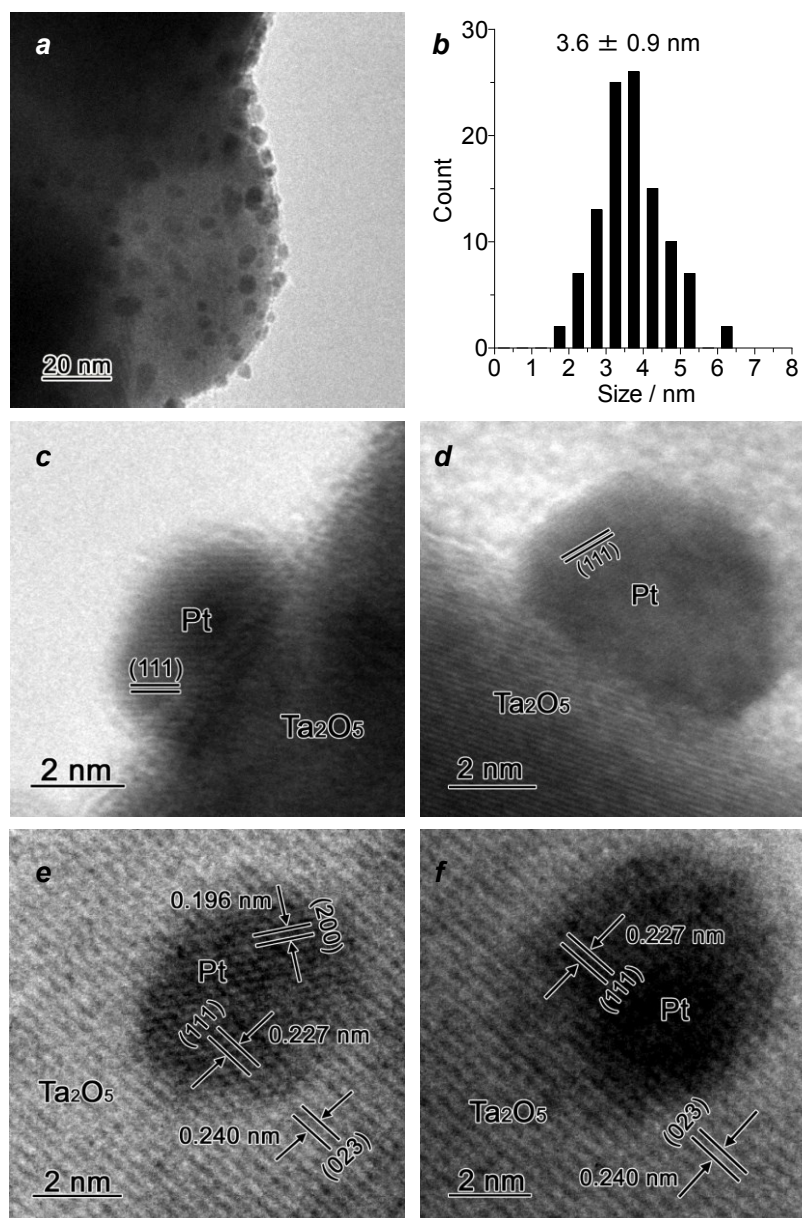
Figure 3-2. (a) Typical TEM image of Pt_2/Ta_2O_5 catalyst and (b) size distribution of the Pt particles. (c−f) High-resolution TEM images of the catalyst.

3. Results and Discussion

3-1. Catalyst Preparation

The Pt_2/Ta_2O_5 catalyst loaded with 2 wt % Pt (= $Pt/Ta_2O_5 \times 100$) was prepared by impregnation of $H_2PtCl_6 \cdot 6H_2O$ onto Ta_2O_5 (average particle size, 1.3 μm; BET surface area, 2.6 m^2 g^{-1}) followed by H_2 reduction at 673 K.[41,42] Transmission electron microscopy (TEM) observation of the catalyst (**Figure 3-2a and 3-2b**) exhibits spherical Pt particles with an average diameter 3.6 nm. High-resolution TEM images (**Figure 3-2c and 3-2d**) reveal that these particles can be indexed as fcc structures, as is the case for bulk Pt

(JCPDS 04-0802). As shown in **Figure 3-3a**, diffuse-reflectance (DR) UV−vis spectra reveal that bare Ta_2O_5 absorbs light at $\lambda < 330$ nm, whereas Pt_2/Ta_2O_5 shows a broad absorption band at $\lambda > 350$ nm, assigned to interband transition of 5d electrons on the Pt particles.[43] These data clearly suggest that visible light activates the Pt particles but does not activate the Ta_2O_5 support.
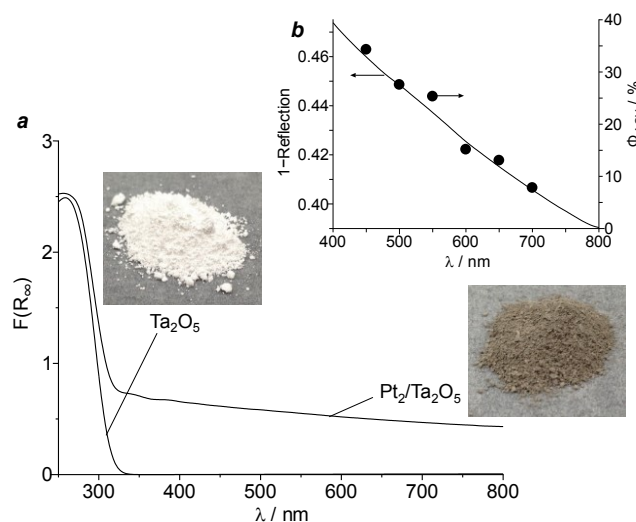
Figure 3-3. (a) DR UV−vis spectra of the catalysts and (b) action spectrum for aerobic oxidation of 2-PrOH on Pt_2/Ta_2O_5. The apparent quantum yield for acetone formation (Φ_{AQY}) was calculated with the equation: Φ_{AQY} (%) = $[\{(Y_{VIS} - Y_{dark}) \times 2\}/(\text{photon number entered into the reaction vessel})] \times 100$, where Y_{VIS} and Y_{dark} are the amounts of acetone formed under visible light irradiation ($\lambda > 450$ nm) and in the dark conditions, respectively.

3-2. Catalytic Activity

High catalytic activity of Pt_2/Ta_2O_5 is demonstrated by aerobic oxidation of 2-propanol (2-PrOH). The reactions were performed by stirring the catalyst (10 mg) in 2-PrOH (5 mL) under an O_2 balloon (~1 atm) in the dark or under visible light irradiation with a Xe lamp ($\lambda > 450$ nm). The temperature of the solution was kept rigorously at 298 ± 0.5 K by a digitally controlled water bath. **Figure 3-4** summarizes the amount of acetone formed by 6 h reaction in the dark (black) or under photoirradiation (white). It is noted that all of the systems selectively produce acetone (mass balance >99%), as is the case for related metal/semiconductor systems.[17−28] Bare Ta_2O_5 is inactive for the reaction in both conditions. In contrast, Pt_2/Ta_2O_5 produces acetone relatively efficiently even in the dark (ca. 0.3 mmol). The striking aspect of this catalyst is the drastic activity enhancement by visible light irradiation; about 5 times the amount of acetone (ca. 1.6 mmol) is produced by the irradiation of $\lambda > 450$ nm light. Other semiconductors (TiO_2, CeO_2, ZrO_2, and $SrTiO_3$)

loaded with Pt or Au particles, which promote the reaction by the e_{hot}^- injection mechanism,[17−28] exhibit only a minor activity enhancement (<0.2 mmol) even by visible light irradiation. In addition, Au, Ag, or Pd particles supported on Ta_2O_5 show almost no activity enhancement. These data suggest that Pt particles, when supported on Ta_2O_5, specifically promote efficient aerobic oxidation under visible light irradiation.

It is generally accepted that a Pt/TiO_2 catalyst shows very high photocatalytic activity under UV irradiation because Pt particles efficiently trap the CB electrons on the photoexcited TiO_2 and create a charge separated state.[44−46] However, as shown by the gray bar in **Figure 3-4**, a Pt_2/TiO_2 catalyst, when irradiated by UV−visible region light (λ >300 nm), produces only a small amount of acetone (ca. 0.25 mmol). This emphasizes extraordinary high catalytic activity of Pt_2/Ta_2O_5 under visible light irradiation. It must be noted that, as shown in **Figure 3-5**, Pt_2/Ta_2O_5 maintains its activity even after prolonged photoirradiation (~36 h), indicating that the catalyst is stable under photoirradiation.

Figure 3-3b shows the action spectrum for aerobic oxidation of 2-PrOH on Pt_2/Ta_2O_5 obtained by monochromatic light irradiation. A good correlation is observed between the absorption spectrum of the catalyst and the apparent quantum yields for acetone formation (Φ_{AQY}). This suggests that interband transition of 5d electrons on the Pt particles by absorbing visible light indeed promotes the reaction. It is noted that the Φ_{AQY} obtained by 550 nm light irradiation is ~25%, which is much higher than that for early reported metal nanoparticle/semiconductor systems (<5%)[17−28] and doped catalysts (<0.5%).[7−14]
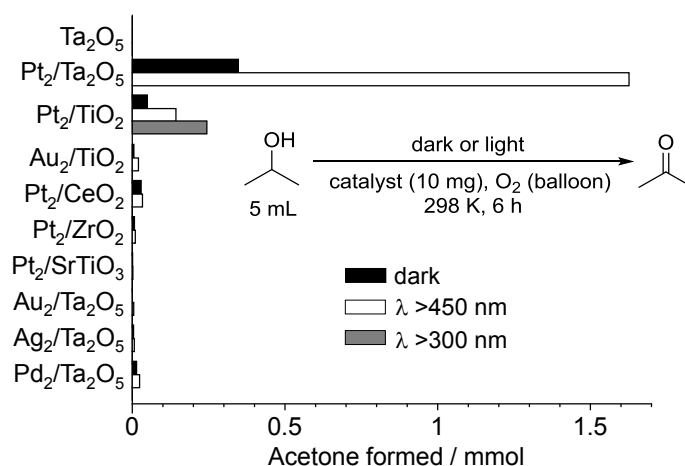
Figure 3-4. Amount of acetone formed by aerobic oxidation of 2-PrOH on the respective catalysts at 298 K, (black) in the dark, (white) under visible light irradiation (λ >450 nm; light intensity at 450−800 nm is 16.8 mW cm^{-2}), and (gray) under UV−visible light irradiation (λ >300 nm; light intensity at 300−800 nm is 21.0 mW cm^{-2}). DR UV− vis spectra of the catalysts are summarized in **Figure 3-6**, and spectral irradiances for the light sources are shown in **Figure 3-7**.
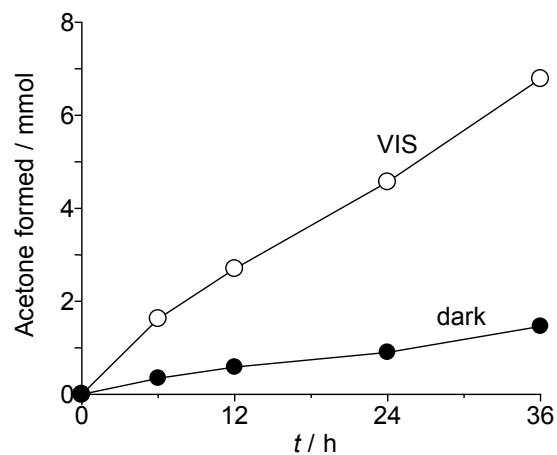
Figure 3-5. Time-dependent change in the amount of acetone formed by aerobic oxidation of 2-PrOH on Pt_2/Ta_2O_5 in the dark or under visible light irradiation ($\lambda >450$ nm). The reaction conditions are identical to those in **Figure 3-4**.

M_2/semiconductor (M = Pt, Au)
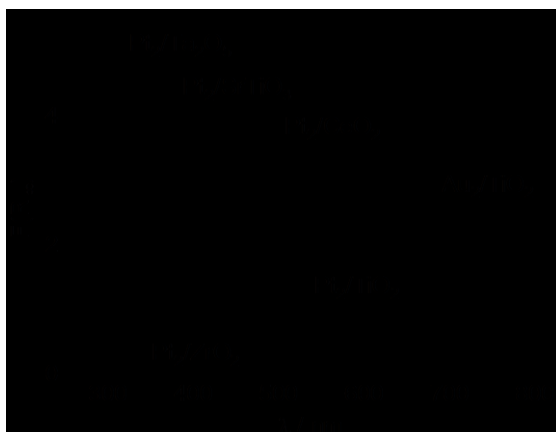
M_2/Ta_2O_5 (M = Pt, Au, Ag, Pd)
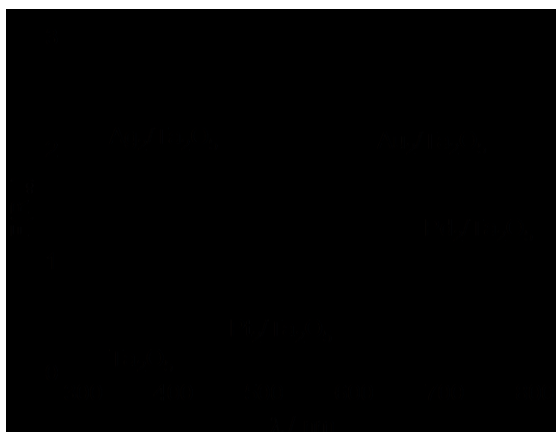
Pt$_x$/Ta$_2$O$_5$
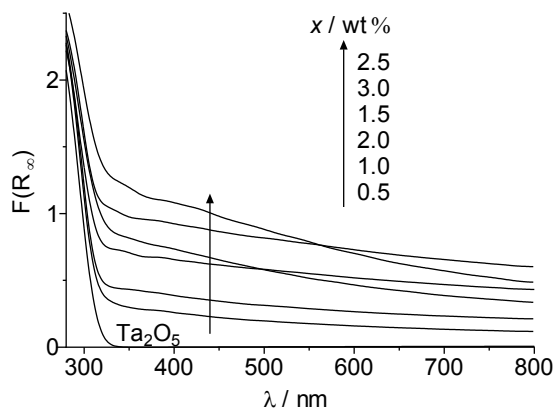
Pt$_2$/Ta$_2$O$_5$ prepared at different H$_2$ reduction temp.
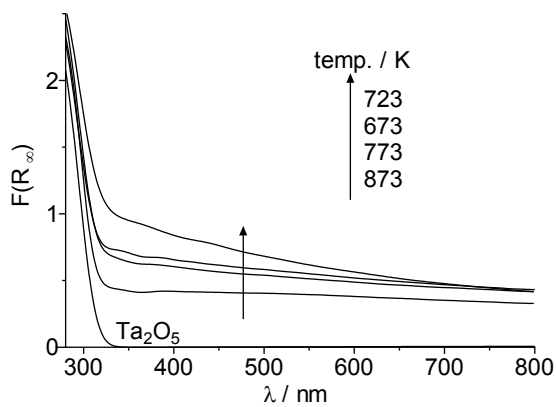
Figure 3-6. DR UV–vis spectra of catalysts.
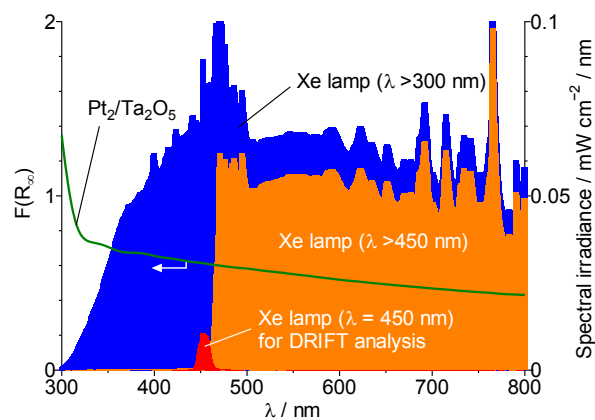
Figure 3-7. Light emmision spectra for Xe lamp (blue) without filter, (orange) with λ >450 nm filter, and (red) with λ = 450 nm band-pass filter. DR UV-vis spectra of Pt$_2$/Ta$_2$O$_5$ catalyst is also shown here.
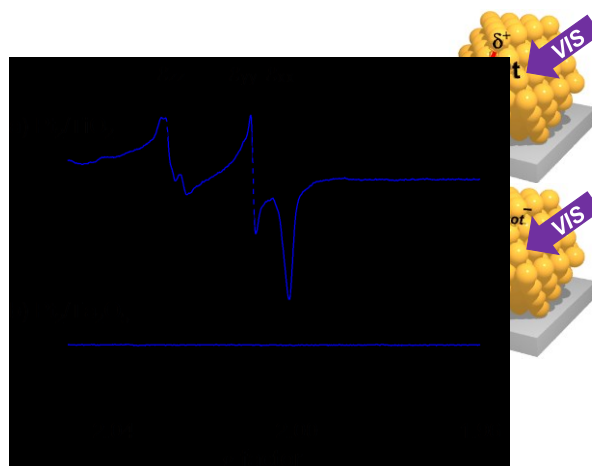
Figure 3-8. ESR spectra of (a) Pt_2/TiO_2 and (b) Pt_2/Ta_2O_5 measured with O_2 at 77 K. The catalysts were left at 298 K with 20 Torr of O_2 (black) in the dark or (blue) under visible light irradiation (λ >450 nm) for 3 h. After evacuation, the respective samples were subjected to analysis at 77 K.
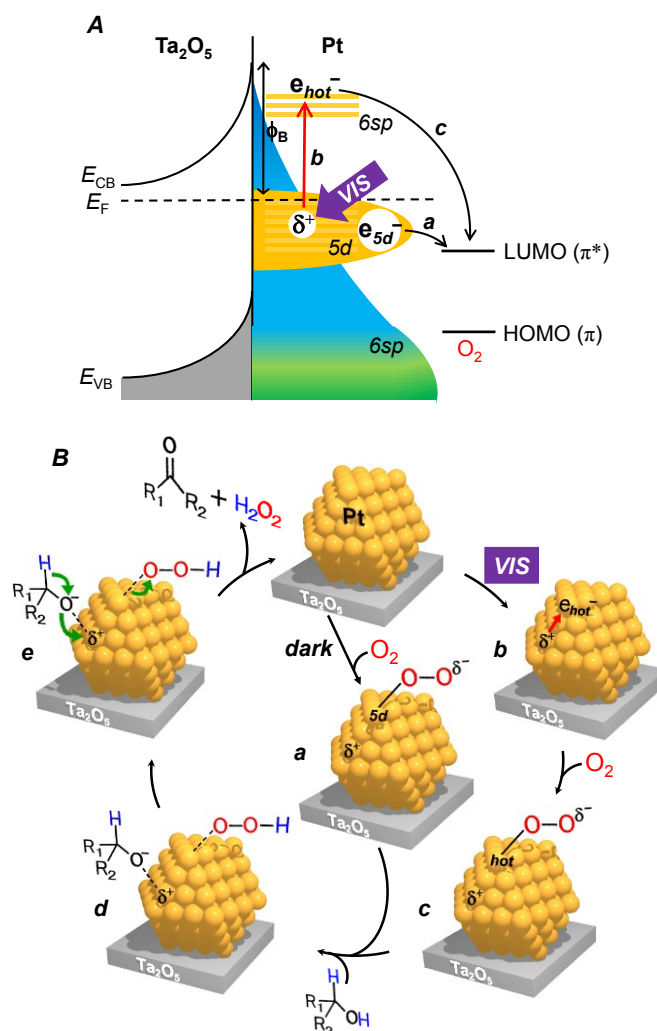
Figure 3-9. (A) Energy Diagram and (B) Proposed Mechanism for Aerobic Oxidation on Pt/Ta_2O_5 in the Dark or under Visible Light

3-3. No e_{hot}^- Injection from Pt to Ta₂O₅

On Pt₂/Ta₂O₅, the e_{hot}^- produced on the photoactivated Pt particles are not injected into the Ta₂O₅ CB. The work function of the Pt particles (average diameter: 3.6 nm) is determined to be W = 6.0 eV,[47−49] and the electron affinity of Ta₂O₅ CB is χ = 3.2 eV.[50,51] The height of Schottky barrier created at the Pt−Ta₂O₅ interface is therefore calculated with the equation, $\phi_B = W - \chi$,[32,33] to be 2.8 eV (λ = 443 nm). This is larger than the energy of light irradiated in the present photoreaction system (λ >450 nm). This suggests that, on Pt/Ta₂O₅, the high ϕ_B suppresses the e_{hot}^- injection from Pt particles to Ta₂O₅ CB. The no e_{hot}^- injection is confirmed by electron spin resonance (ESR) analysis of the catalysts. The Pt₂/TiO₂ catalyst, which promotes aerobic oxidation by the e_{hot}^- injection mechanism,[25−28] was irradiated by visible light (λ >450 nm) with O₂ at 298 K. As shown by the blue line in **Figure 3-8a**, the sample, when subjected to ESR analysis at 77 K, shows strong signals assigned to superoxide anion formed on the TiO₂ surface (g_{xx} = 2.002, g_{yy} = 2.009, g_{zz} = 2.028).[52] This suggests that, as shown in **Figure 3-1**, the e_{hot}^- photoformed on the Pt particles are indeed injected into the TiO₂ CB and reduce O₂ on the TiO₂ surface. In contrast, as shown by the blue line in **Figure 3-8b**, visible light irradiation of Pt₂/Ta₂O₅ with O₂ does not create superoxide signal. This clearly indicates that e_{hot}^- injection from Pt particles to Ta₂O₅ does not occur.

3-4. Catalysis Mechanism on Pt/Ta₂O₅

Mechanism for aerobic oxidation on Pt/Ta₂O₅ can be explained by **Figure 3-9**. In the dark condition, Pt particles partially donate their 5d electrons (e_{5d}^-) to LUMO (π^*) of O₂ (**Figure 3-9.a**).[53−55] This activates O₂ and produces anionic peroxo species ($Pt_{5d}-O-O^{\delta-}$, **Figure 3-9B.a**).[56,57] Visible light absorption of the Pt particles promotes interband transition of their e_{5d}^-, producing a large number of e_{hot}^- (**Figure 3-9A.b and 3-9B.b**). The e_{hot}^- also activate O₂ by partial electron donation (**Figure 3-9A.c**),[39] producing a large number of anionic peroxo species ($Pt_{hot}-O-O^{\delta-}$; **Figure 3-9B.c**). These peroxo species ($Pt_{5d}-O-O^{\delta-}$ and $Pt_{hot}-O-O^{\delta-}$) behave as the active species for oxidation: they abstract the α-hydrogen of alcohos and produce alcoholate and hydroperoxide species on the Pt surface (**Figure 3-9B.d**).[58] Subsequent abstraction of β-hydrogen from the alcoholate species produces the corresponding carbonyl product (**Figure 3-9B.e**).

3-5. Formation of Peroxo Species

In the present Pt/Ta₂O₅ system, anionic peroxo species ($Pt_{hot}-O-O^{\delta-}$) formed by e_{hot}^- donation to O₂ on the Pt surface act as the active species. As reported,[39] aerobic oxidation of ethylene on the Ag/α-Al₂O₃ catalyst under visible light irradiation is also considered to occur via e_{hot}^- donation to O₂ on the Ag surface.

Similar anionic peroxo species (Ag$-$O$-$O$^{\delta-}$) are proposed to act as active species based on the DFT calculation. The formation of the Pt$_{hot}$$-O-O^{\delta-}$ species (**Figure 3-9B.c**) on the Pt surface by visible light irradiation is confirmed by the diffuse-reflectance infrared Fourier transform (DRIFT) analysis of O$_2$ adsorbed onto the catalysts. As shown in **Figure 3-10a**, bare Ta$_2$O$_5$ measured with O$_2$ shows almost no signal in the dark (black) or under irradiation of 450 nm light (blue). In contrast, as shown in **Figure 3-10b** (black), Pt$_2$/Ta$_2$O$_5$ measured with O$_2$ in the dark creates a band at 2037 cm^{-1}, assigned to O$-$O vibration of peroxo species.[59] This suggests that, as shown in **Scheme 3-10A.a and 3-10B.a**, the peroxo species (Pt$_{5d}$$-O-O^{\delta-}$) are indeed produced by partial e$_{5d}^-$ donation to O$_2$.[56,57] In contrast, visible light irradiation of Pt$_2$/Ta$_2$O$_5$ with O$_2$ (**Figure 3-10b**, blue) creates a very strong O$-$O band at the blue-shifted position (2048 cm^{-1}). This suggests that, as shown in **Figure 3-9A.c and 3-9B.c**, a large number of more anionic peroxo species (Pt$_{hot}$$-O-O^{\delta-}$) are indeed produced via a strong e$_{hot}^-$ donation to O$_2$. It is noted that, as shown in **Figure 3-10b** (green), the Pt$_2$/Ta$_2$O$_5$ catalyst, when treated with O$_2$ at high temperature (343 K) in the dark, shows a red-shifted signal at 2037 cm^{-1}, which is similar to that obtained in the dark at 303 K (black). This indicates that, under present photoirradiation conditions, photothermal conversion[60] on the Pt particles does not occur.[61−64] This again suggests that, as shown in **Figure 3-9A.c and 3-9B.c**, visible light irradiation of the Pt/Ta$_2$O$_5$ catalyst produces peroxo species (Pt$_{hot}$$-O-O^{\delta-}$) via an e$_{hot}^-$ donation to O$_2$.

In contrast, as shown in **Figure 3-10c−e**, Pt$_2$/TiO$_2$, Pt$_2$/CeO$_2$, and Pt$_2$/ZrO$_2$ do not show O$-$O band even under visible light irradiation. The O$-$O band intensities on the respective catalysts are consistent with the activity data (**Figure 3-4**). This suggests that, on Pt/Ta$_2$O$_5$, the enhanced e$_{hot}^-$ formation on the Pt particles efficiently activates O$_2$ and produces a large number of peroxo species; this is the crucial factor for high catalytic activity. Figure 5f shows the time-dependent change in the Pt$_{hot}$$-O-O^{\delta-}$ signal on the Pt$_2$/Ta$_2$O$_5$ catalyst, when left in the dark at 303 K after addition of 2-PrOH in the gas phase. The signal decreases with time, and GC analysis of the fouling on the resulting catalyst detected a formation of acetone. These findings clearly suggest that abstraction of alcohol hydrogen by the peroxo species (**Figure 3-9B.c → d**) indeed promotes aerobic oxidation.
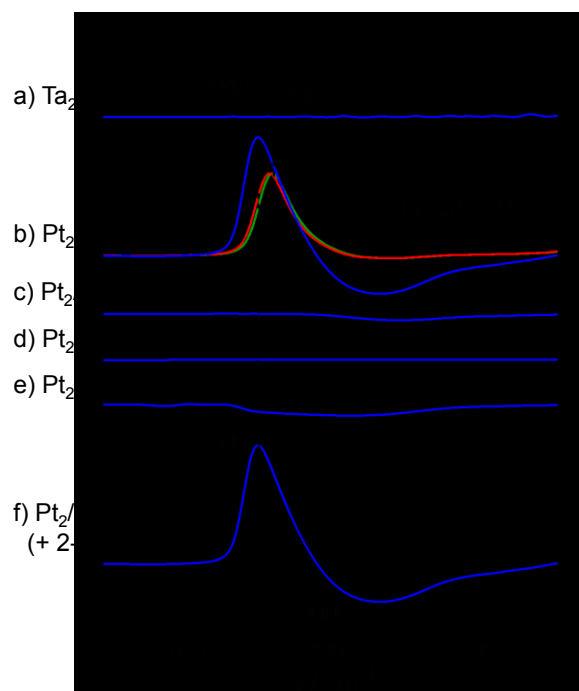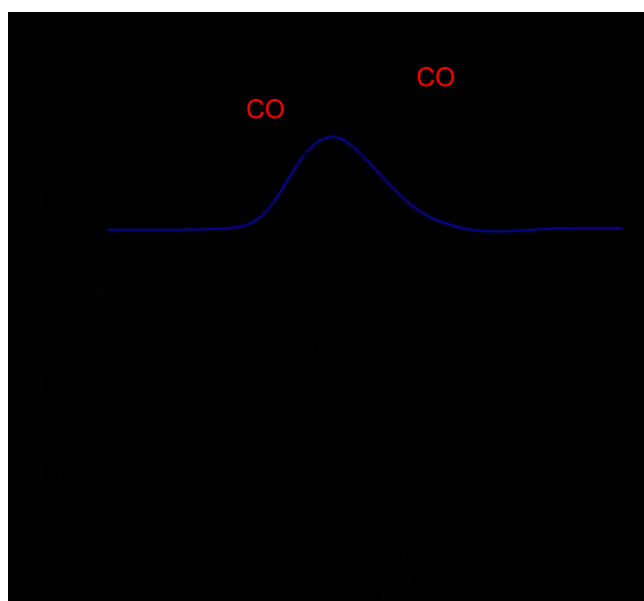
Figure 3-10. (a−e) DRIFT spectra of O_2 adsorbed onto the catalysts, measured (black) in the dark at 303 K, (green) in the dark at 343 K, (blue) under 450 nm light irradiation at 303 K, or (red) under 450 nm light irradiation at 343 K. The catalyst (20 mg) was evacuated (6.8×10^{-3} Torr) at 423 K for 3 h. O_2 (1.5 Torr) was introduced to the cell at the designated temperature and left for 1 h in the dark or under photoirradiation. (f) Time-dependent spectral change (intervals: 5 min) monitored in the dark at 303 K after addition of 2-PrOH (7.5×10^{-1} Torr) to the Pt_2/Ta_2O_5 sample obtained after 450 nm light irradiation at 303 K with O_2 for 1 h (sample b, blue).
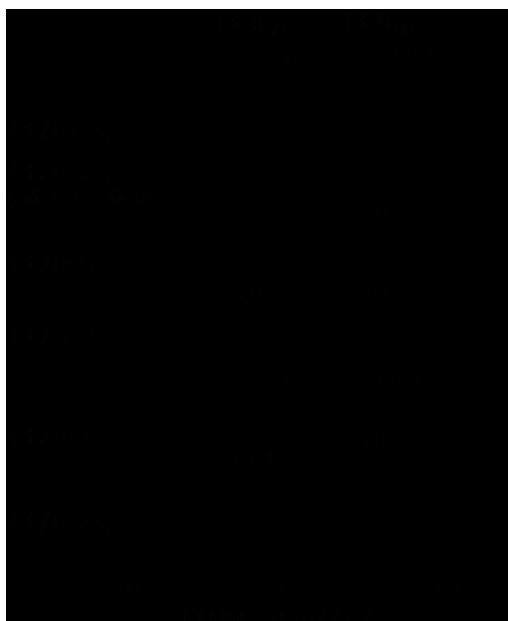
Figure 3-11. XPS chart (Pt 4f level) of respective catalysts.

3-6. Electron Density of Pt Particles on Ta_2O_5

The efficient e_{hot}^- formation on the Pt particles, when supported on Ta_2O_5, is due to the high electron density of the Pt particles by strong Pt−Ta_2O_5 interaction. The Fermi levels of Pt and Ta_2O_5 lie at −5.65 eV (bulk)[49] and −4.25 eV,[65] respectively (from vacuum level), indicating that there is a large Fermi level difference between Pt and Ta_2O_5. Strong metal−support interaction,[66−68] if it occurs, may therefore promote electron donation from Ta_2O_5 to Pt for the Fermi level balancing and result in high electron density of Pt particles. X-ray photoelectron spectroscopy (XPS) of the catalysts confirms this. As shown in **Figure 3-11**, the Pt/Ta_2O_5 catalyst exhibits Pt 4f 5/2 and 7/2 peaks at 73.0 and 69.7 eV, respectively. In contrast, the Pt peaks for other catalysts (Pt/TiO_2, Pt/CeO_2, and Pt/ZrO_2) appear at higher binding energy. This indicates that the Pt particles on Ta_2O_5 are indeed charged more negatively. These data clearly indicate that strong Pt−Ta_2O_5 interaction enhances electron donation from Ta_2O_5 to Pt at the interface and, hence, increases electron density of the Pt particles.[69]

Figure 3-12. DRIFT spectra of CO adsorbed onto the catalysts (black) in the dark or (blue) under 450 nm light irradiation at 303 K. The catalysts (20 mg) were evacuated (6.8×10^{-3} Torr) at 423 K for 3 h. CO (1.5 Torr) was introduced into the cell at 303 K and left for 1 h in the dark or under photoirradiation.

It is well-known that a reducible metal oxide support is crucial for strong metal−support interaction, where the oxygen vacancies of the support adjacent to the reduced metal cations facilitate strong adhesion of metal.[30] A correlation between the reducibility of supports and the interaction strength with metal indicates strong metal−Ta_2O_5 interaction.[70] Strong Pt−Ta_2O_5 interaction is supported by HRTEM

observations. As shown in **Figure 3-3e,f**, the Pt(111) plane is adsorbed onto the Ta_2O_5(023) plane. Their lattice spacings are determined to be 0.227 and 0.240 nm, respectively. A good agreement of the spacings (deviation: ~6%) indicates epitaxial growth of Pt particles on the Ta_2O_5(023) plane.[71,72] These data suggest that strong adhesion of Pt onto the oxygen vacancies of Ta_2O_5 surface facilitates strong Pt−Ta_2O_5 interaction.

The high electron density of the Pt particles on Ta_2O_5 is further confirmed by DRIFT analysis of carbon monoxide (CO) adsorbed onto the Pt particles, because the stretching frequency of the adsorbed CO depends strongly on the electron density of metal particles.[57,73] **Figure 3-12** shows the DRIFT spectra of CO adsorbed onto the catalysts at 303 K. Bare Ta_2O_5 measured in the dark (**Figure 3-12a**) shows almost no signal, indicating that its surface is inactive for CO adsorption. As shown in **Figure 3-12b** (black), Pt_2/Ta_2O_5 shows a CO stretching band at 2046 cm^{-1}. Other Pt-loaded catalysts show blue-shifted bands (**Figure 3-12c−e**). This indicates that the Pt particles on Ta_2O_5 indeed possess high electron density. The XPS and DRIFT data therefore imply that the high electron density of the Pt particles on Ta_2O_5 enhances interband transition of e_{5d}^- and produces a large number of e_{hot}^-.

As shown in **Figure 3-12b** (blue), CO molecules, when adsorbed onto Pt_2/Ta_2O_5 under 450 nm light irradiation, exhibit a redshifted and stronger stretching at 2040 cm^{-1}. This indicates that the Pt particles are charged more negatively by visible light irradiation. This is because CO molecules are strongly adsorbed onto the Pt surface via stronger electron donation from the photoformed e_{hot}^-. This is consistent with the DRIFT data for the formation of peroxo species (**Figure 3-12b**, blue). The results strongly support the proposed mechanism for efficient aerobic oxidation via O_2 activation by the photogenerated e_{hot}^- (**Figure 3-9**).

3-7. Effect of Pt Amount

The catalytic activity of the e_{hot}^--induced aerobic oxidation on Pt/Ta_2O_5 depends on the amount of Pt loaded. The Pt_x/Ta_2O_5 catalysts with different Pt loadings [x (wt %) = Pt/Ta_2O_5 × 100; x = 0.5−3 wt %] were prepared by H_2 reduction at 673 K. As shown in **Figure 3-13a** (orange), these catalysts contain Pt particles with similar sizes (3.6−3.8 nm). The black and white bars show the amounts of acetone formed by aerobic oxidation of 2-PrOH on the catalysts for 6 h in the dark or under irradiation of visible light, respectively. The activity enhancement by photoirradiation increases with the Pt loadings because an increased number of surface Pt atoms produces a larger number of e_{hot}^-. Among the catalysts, Pt_2/Ta_2O_5 shows the largest activity enhancement, and further Pt loadings (x > 2.5) are ineffective. This is because, as often observed for related metal/semiconductor systems,[74] larger Pt loadings lead to an inefficient electron donation from

Ta$_2$O$_5$ to Pt and creates Pt particles with lower electron density. This is confirmed by higher binding energy for the Pt XPS peaks of Pt$_3$/Ta$_2$O$_5$ than that of Pt$_2$/Ta$_2$O$_5$ (**Figure 3-11**). As a result of this, the Pt$_2$/Ta$_2$O$_5$ catalyst containing Pt particles with high electron density enhances interband transition of their e$_{5d}^-$ and exhibits the highest activity enhancement by visible light irradiation.
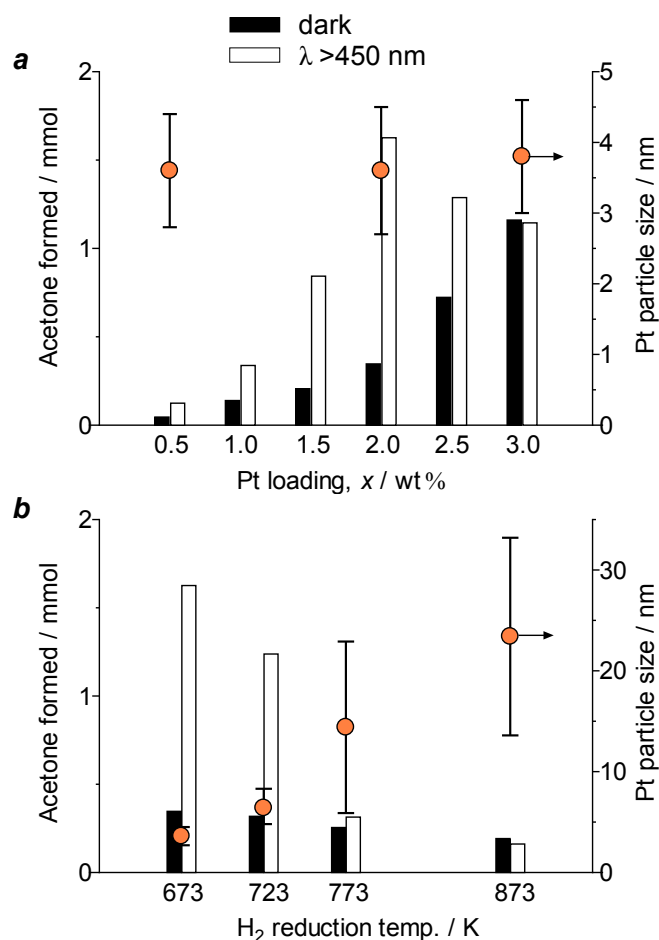

Figure 3-11. Effect of (a) Pt loading (x) of Pt$_x$/Ta$_2$O$_5$ catalysts and (b) H$_2$ reduction temperature of Pt$_2$/Ta$_2$O$_5$ catalysts on the amount of acetone formed by aerobic oxidation of 2-PrOH (6 h reaction), performed (black) in the dark or (white) under visible light irradiation at 298 K. The reaction conditions are identical to those in **Figure 3-4**. Circles denote the average diameters of Pt particles on the respective catalysts. The H$_2$ reduction temperature for the catalysts (a) is 673 K, and the Pt loading of the catalysts (b) is 2 wt %, respectively. Typical TEM images of the catalysts and size distributions of the Pt particles are summarized in **Figure 3-12**.

Pt₀.₅/Ta₂O₅
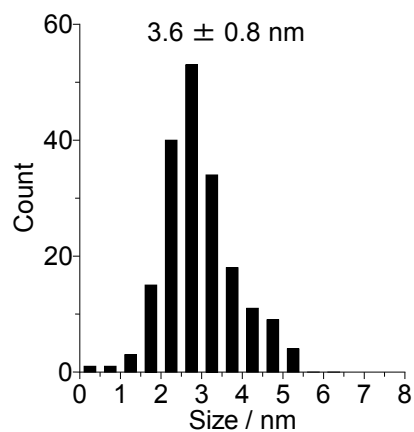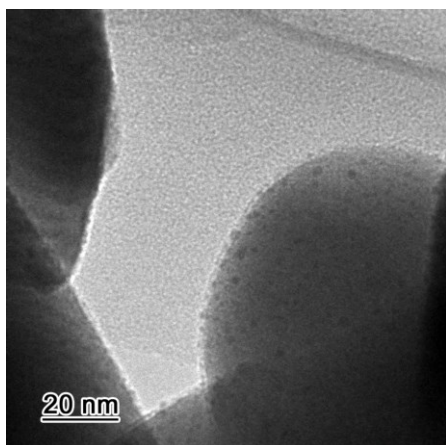
Pt₃/Ta₂O₅
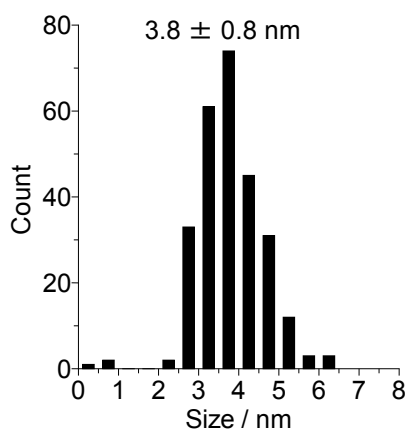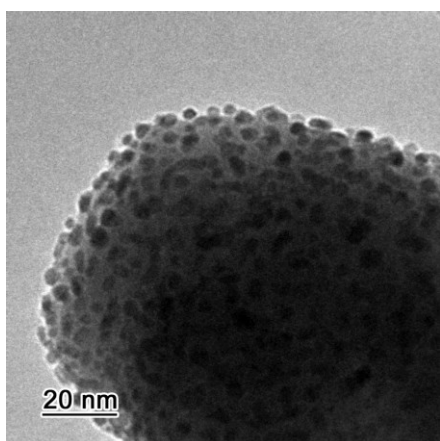
Pt₂/Ta₂O₅ prepared by H₂ reduction at 723 K

81
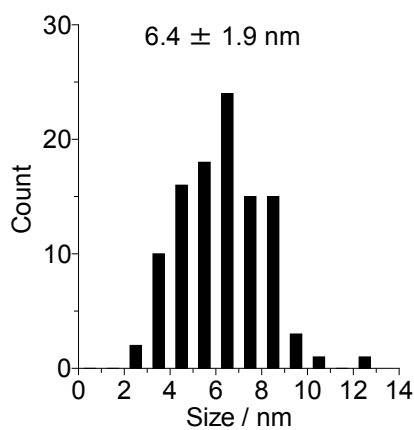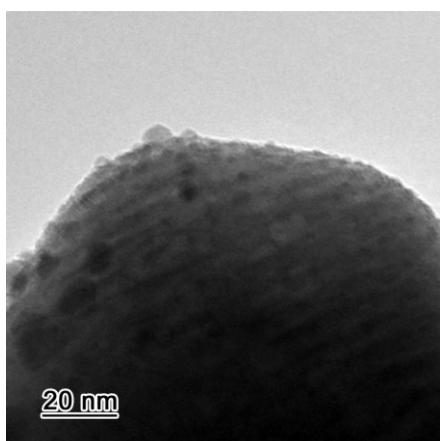
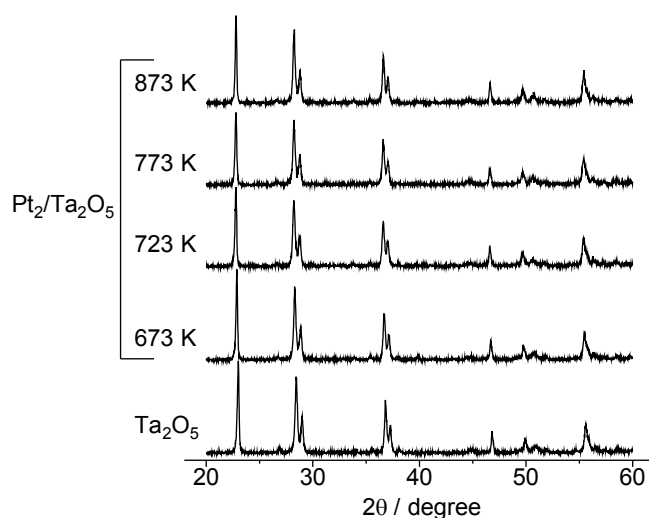**Pt$_2$/Ta$_2$O$_5$ prepared by H$_2$ reduction at 773 K**
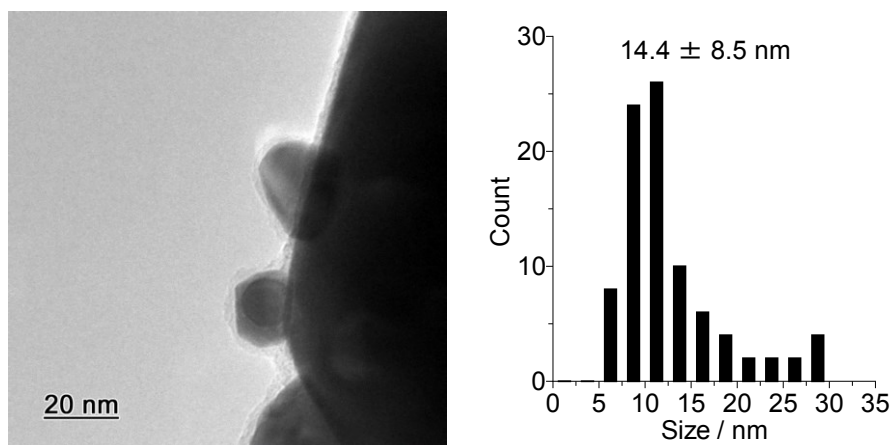
**Pt$_2$/Ta$_2$O$_5$ prepared by H$_2$ reduction at 873 K**
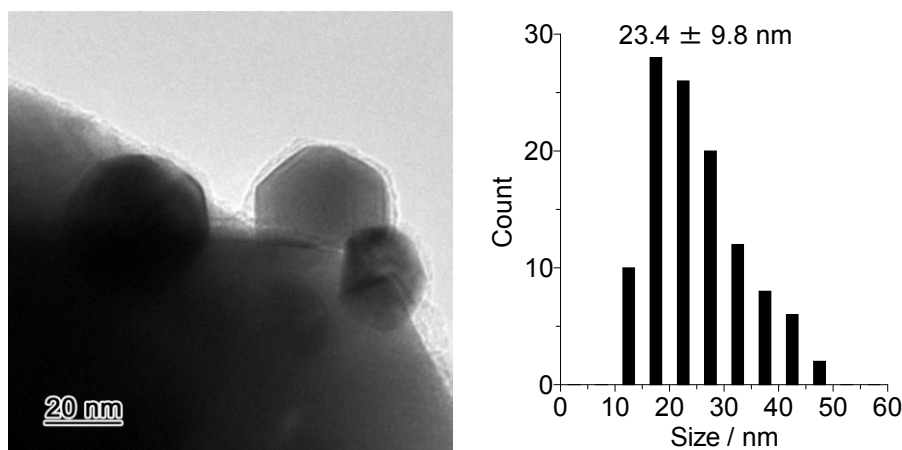
Figure 3-12. Typical TEM images of Pt$_x$/Ta$_2$O$_5$ and size distribution of the Pt particles.

3-8. Effect of Pt Particle Size.

The size of Pt particles also affects the catalytic activity. The Pt$_2$/Ta$_2$O$_5$ catalysts were prepared by H$_2$ reduction at different temperatures (673−873 K) while maintaining 2 wt % Pt loading. As shown in **Figure 3-13b** (orange), the size of Pt particles increases with a rise in reduction temperature due to the sintering of Pt particles.[26] It is noted that, as shown in **Figure 3-14**, X-ray diffraction (XRD) patterns of the catalysts reveal that phase transition of Ta$_2$O$_5$ support scarcely occurs during H$_2$ reduction at this temperature range. As shown by the bar data in **Figure 3-13b**, the increase in the Pt particle size significantly decreases the activity enhancement by visible light irradiation. The size increase decreases the number of surface Pt atoms. This may decrease the number of e_{hot}^-, probably resulting in decreased activity enhancement. These data indicate that the Pt/Ta$_2$O$_5$ catalyst with 2 wt % Pt, containing <5 nm Pt particles, efficiently promotes interband transition of their e_{5d}^- and exhibits the largest activity enhancement by visible light irradiation.

Figure 3-14. XRD patterns of Pt_2/Ta_2O_5 prepared at different H_2 reduction temperature.
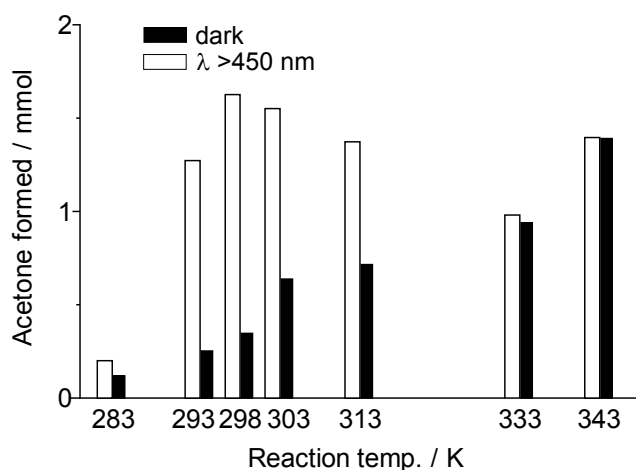
Figure 15. Effect of reaction temperature on the amount of acetone formed during oxidation of 2-PrOH (6 h reaction) with Pt_2/Ta_2O_5 catalyst, performed (black) in the dark or (white) under visible light irradiation. The reaction conditions are identical to those in **Figure 3-4**.
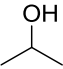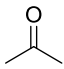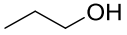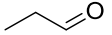
3-9. Effect of Reaction Temperature
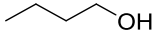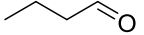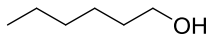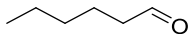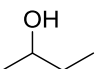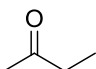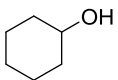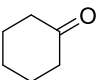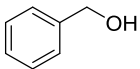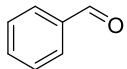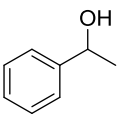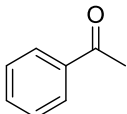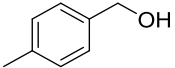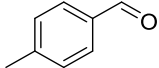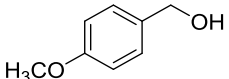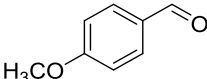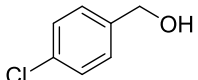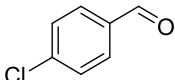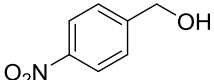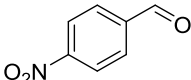
The catalytic activity of Pt_2/Ta_2O_5 is also affected by reaction temperature. **Figure 3-15** summarizes the results of aerobic oxidation at different reaction temperatures on the Pt_2/Ta_2O_5 catalyst prepared by H_2 reduction at 673 K. The dark activity (black bars) increases with a rise in reaction temperature because this enhances the e_{5d}^- donation to O_2[53–55] and produces a larger number of active peroxo species ($Pt_{5d}-O-O^{\delta-}$), as shown in **Figure 3-9A and 3-9B.a**. In contrast, under visible light irradiation (white bars), the highest

83

activity is obtained at 298 K, and the activity decreases at lower or higher temperature. Two factors may affect the reaction. The activity decrease at <298 K is probably due to the decrease in electron conductivity of Pt particles with decreasing temperature.[75-77] This may suppress the e_{hot}^- formation on the Pt surface and, hence, decrease the catalytic activity.

In contrast, the activity decrease at higher temperature is probably due to the enhanced e_{5d}^- donation to O_2. This may suppress interband transition of e_{5d}^- and results in decreased e_{hot}^- formation. As shown in **Figure 3-15**, a rise in temperature at >298 K decreases the photocatalytic activity while increasing the dark activity, and almost no photocatalytic reaction occurs at >333 K. This means that acceleration of the dark reaction at higher temperature suppresses photocatalytic reaction. This is confirmed by DRIFT analysis. As shown by the black line (**Figure 3-10b**), Pt_2/Ta_2O_5 measured with O_2 at 303 K in the dark shows a peak at 2037 cm^{-1}, assigned to the $Pt_{5d}-O-O^{\delta-}$ species formed via an e_{5d}^- donation to O_2. As shown by the green line, the sample, when measured at 343 K in the dark, shows a stronger peak at the same position, indicating that e_{5d}^- donation to O_2 is accelerated by thermal activation of e_{5d}^- at higher temperature. In contrast, as shown by the blue line, the sample measured at 303 K under visible light irradiation shows a peak at 2048 cm^{-1}, assigned to the $Pt_{hot}-O-O^{\delta-}$ species formed via an e_{hot}^- donation to O_2. However, as shown by the red line, the sample measured at 343 K under visible light irradiation shows a red-shifted peak at 2037 cm^{-1}, which is similar to that measured at 343 K in the dark (green). These data suggest that the e_{hot}^- formation is suppressed at higher temperature. Thermal activation of e_{5d}^- at higher temperature enhances the e_{5d}^- donation to O_2. This may suppress the interband transition of e_{5d}^- and results in decreased e_{hot}^- formation.

The above findings suggest that visible light irradiation at around room temperature is the condition suitable for maximizing the activity of the Pt_2/Ta_2O_5 catalyst for aerobic oxidation. It must be noted that, at this photoirradiation condition, the Pt_2/Ta_2O_5 catalyst selectively oxidizes various types of alcohols. As summarized in **Table 3-2**, reactions of aliphatic (linear and cyclic) and benzylic alcohols on Pt_2/Ta_2O_5 successfully produce the corresponding aldehydes and ketones with very high yields (>90 %), even in the presence of electron-withdrawing Cl and NO_2 substituents.

Table 3-2. Aerobic oxidation of various types of alcohols on Pt_2/Ta_2O_5 under visible light irradiation.[a]

Substrate	Substrate conv. / % [b]	Product	Yield / % [b]
OH (isopropanol)	>99	O (acetone)	>99
OH (1-propanol)	>99	O (propanal)	96
OH (1-butanol)	93	O (butanal)	93
OH (1-hexanol)	93	O (hexanal)	90
OH (2-butanol)	>99	O (2-butanone)	94
OH (cyclohexanol)	97	O (cyclohexanone)	95
OH (benzyl alcohol)	>99	O (benzaldehyde)	>99
OH (1-phenylethanol)	>99	O (acetophenone)	97
OH (4-methylbenzyl alcohol)	96	O (4-methylbenzaldehyde)	95
H_3CO— OH (4-methoxybenzyl alcohol)	>99	H_3CO— O (4-methoxybenzaldehyde)	>99
Cl— OH (4-chlorobenzyl alcohol)	>99	Cl— O (4-chlorobenzaldehyde)	>99
O_2N— OH (4-nitrobenzyl alcohol)	>99	O_2N— O (4-nitrobenzaldehyde)	>99

[a] Reaction conditions: toluene (5 mL), alcohol (5 mM), Pt_2/Ta_2O_5 catalyst (100 mg), O_2 (1 atm), Xe lamp (λ >450 nm), light intensity at 450–800 nm (16.8 mW cm^{-2}), temperature (298 ± 0.5 K), time (12 h). [b] Determined by GC analysis.

4. Conclusion

The author found that Pt nanoparticles (~5 nm diameter), when supported on Ta_2O_5, behave as visible-light-driven catalysts for efficient aerobic oxidation at room temperature. Visible light absorption of the Pt particles produces a large number of e_{hot}^- via the enhanced interband transition of their 5d electrons. They activate O_2 and produce a large number of peroxide species behaving as key active species for oxidation. The basic concept presented here, based on the enhanced e_{hot}^- formation on the metal particles by an appropriate semiconductor support and the promotion of photocatalysis without e_{hot}^- injection into the semiconductor CB, may contribute to the creation of more active catalyst driven by visible light and to the design of sunlight-driven organic synthesis.

5. References

[1] Sheldon, R. A.; Arends, I. W. C. E.; Dijksman, A. *Catal. Today* **2000**, *57*, 157−166.

[2] Fox, M. A.; Dulay, M. T. *Chem. Rev.* **1993**, *93*, 341−357.

[3] Maldotti, A.; Molinari, A.; Amadelli, R. *Chem. Rev.* **2002**, *102*, 3811−3836.

[4] Palmisano, G.; Augugliaro, V.; Pagliaro, M.; Palmisano, L. *Chem. Commun.* **2007**, 3425−3437.

[5] Fagnoni, M.; Dondi, D.; Ravelli, D.; Albini, A. *Chem. Rev.* **2007**, *107*, 2725−2756.

[6] Shiraishi, Y.; Hirai, T. *J. Photochem. Photobiol., C* **2008**, *9*, 157−170.

[7] Asahi, R.; Morikawa, T.; Ohwaki, T.; Aoki, K.; Taga, Y. *Science* **2001**, *293*, 269−271.

[8] Miyauchi, M.; Ikezawa, A.; Tobimatsu, H.; Irie, H.; Hashimoto, K. *Phys. Chem. Chem. Phys.* **2004**, *6*, 865−870.

[9] Ohno, T.; Akiyoshi, M.; Umebayashi, T.; Asai, K.; Mitsui, T.; Matsumura, M. *Appl. Catal., A* **2004**, *265*, 115−121.

[10] Yan, X.; Ohno, T.; Nishijima, K.; Abe, R.; Ohtani, B. *Chem. Phys. Lett.* **2006**, *429*, 606−610.

[11] Sakthivel, S.; Kisch, H. *Angew. Chem., Int. Ed.* **2003**, *42*, 4908−4911.

[12] Irie, H.; Watanabe, Y.; Hashimoto, K. *Chem. Lett.* **2003**, *32*, 772−773.

[13] Zhao, W.; Ma, W.; Chen, C.; Zhao, J.; Shuai, Z. *J. Am. Chem. Soc.* **2004**, *126*, 4782−4783.

[14] Zaleska, A.; Sobczak, J. W.; Grabowska, E.; Hupka, *J. Appl. Catal., B* **2008**, *78*, 92−100.

[15] Chen, X.; Mao, S. S. *Chem. Rev.* **2007**, *107*, 2891−2959.

[16] Primo, A.; Corma, A.; García, H. *Phys. Chem. Chem. Phys.* **2011**, *13*, 886−910.

[17] Tian, Y.; Tatsuma, T. *J. Am. Chem. Soc.* **2005**, *127*, 7632−7637.

[18] Kowalska, E.; Mahaney, O. O. P.; Abe, R.; Ohtani, B. Phys. *Chem. Chem. Phys.* **2010**, *12*, 2344−2355.

[19] Tsukamoto, D.; Shiraishi, Y.; Sugano, Y.; Ichikawa, S.; Tanaka, S.; Hirai, T. *J. Am. Chem. Soc.* **2012**, *134*, 6309−6315.

[20] Tanaka, A.; Hashimoto, K.; Kominami, H. *J. Am. Chem. Soc.* **2012**, *134*, 14526−14533.

[21] Kimura, K.; Naya, S.; Jin-nouchi, Y.; Tada, H. *J. Phys. Chem. C* **2012**, *116*, 7111−7117.

[22] Naya, S.; Kimura, K.; Tada, H. *ACS Catal.* **2013**, *3*, 10−13.

[23] Sugano, Y.; Shiraishi, Y.; Tsukamoto, D.; Ichikawa, S.; Tanaka, S.; Hirai, T. *Angew. Chem., Int. Ed.* **2013**, *52*, 5295−5299.

[24] Liu, L.; Li, P.; Adisak, B.; Ouyang, S.; Umezawa, N.; Ye, J.; Kodiyath, R.; Tanabe, T.; Ramesh, G. V.; Ueda, S.; Abe, H. *J. Mater. Chem. A* **2014**, *2*, 9875−9882.

[25] Zai, W.; Xue, S.; Zhu, A.; Luo, Y.; Tian, Y. *ChemCatChem* **2011**, *3*, 127−130.

[26] Shiraishi, Y.; Tsukamoto, D.; Sugano, Y.; Shiro, A.; Ichikawa, S.; Tanaka, S.; Hirai, T. *ACS Catal.* **2012**, *2*, 1984−1992.

[27] Shiraishi, Y.; Sakamoto, H.; Sugano, Y.; Ichikawa, S.; Hirai, T. *ACS Nano* **2013**, *7*, 9287−9297.

[28] Shiraishi, Y.; Sakamoto, H.; Fujiwara, K.; Ichikawa, S.; Hirai, T. *ACS Catal.* **2014**, *4*, 2418−2425.

[29] Hao, Q.; Juluri, B. K.; Zheng, Y. B.; Wang, B.; Chiang, I.-K.; Jensen, L.; Crespi, V.; Eklund, P. C.; Huang, T. J. *J. Phys. Chem. C* **2010**, *114*, 18059−18066.

[30] Park, J. Y.; Baker, L. R.; Somorjai, G. A. *Chem. Rev.* **2015**, *115*, 2781−2817.

[31] Link, S.; El-Sayed, M. A. *Int. Rev. Phys. Chem.* **2000**, *19*, 409−453.

[32] Schottky, W. *Eur. Phys. J. A* **1939**, *113*, 367−414.

[33] Nakato, Y.; Ueda, K.; Yano, H.; Tsubomura, H. *J. Phys. Chem.* **1988**, *92*, 2316−2324.

[34] Brongersma, M. L.; Halas, N. J.; Nordlander, P. *Nat. Nanotechnol.* **2015**, *10*, 25−34.

[35] Mukherjee, S.; Zhou, L.; Goodman, A. M.; Large, N.; Ayala-Orozco, C.; Zhang, Y.; Nordlander, P.; Halas, N. J. *J. Am. Chem. Soc.* **2014**, *136*, 64−67.

[36] Mukherjee, S.; Libisch, F.; Large, N.; Neumann, O.; Brown, L. V.; Cheng, J.; Lassiter, J. B.; Carter, E. A.; Nordlander, P.; Halas, N. J. *Nano Lett.* **2013**, *13*, 240−247.

[37] Kale, M. J.; Avanesian, T.; Xin, H.; Yan, J.; Christopher, P. *Nano Lett.* **2014**, *14*, 5405−5412.

[38] Christopher, P.; Xin, H.; Linic, S. *Nat. Chem.* **2011**, *3*, 467−472.

[39] Christopher, P.; Xin, H.; Marimuthu, A.; Linic, S. *Nat. Mater.* **2012**, *11*, 1044−1050.

[40] Avanesian, T.; Christopher, P. *J. Phys. Chem. C* **2014**, *118*, 28017−28031.

[41] Shiraishi, Y.; Ikeda, M.; Tsukamoto, D.; Tanaka, S.; Hirai, T. *Chem. Commun.* **2011**, *47*, 4811−4813.

[42] Shiraishi, Y.; Takeda, Y.; Sugano, Y.; Ichikawa, S.; Tanaka, S.; Hirai, T. *Chem. Commun.* **2011**, *47*,

7863−7865.

[43] Bigall, N. C.; Härtling, T.; Klose, M.; Simon, P.; Eng, L. M.; Eychmüller, A. *Nano Lett.* **2008**, *8*, 4588−4592.

[44] Szabó-Bárdos, E.; Czili, H.; Horváth, A. *J. Photochem. Photobiol., A* **2003**, *154*, 195−201.

[45] Subramanian, V.; Wolf, E. E.; Kamat, P. V. *J. Am. Chem. Soc.* **2004**, *126*, 4943−4950.

[46] Zhang, H.; Chen, G.; Bahnemann, D. W. *J. Mater. Chem.* **2009**, 19, 5089−5121.

[47] The work function of metal particles (*W*) depends on their sizes and is defined as the following equation: $W = W_{bulk} + 1.08/d$ (ref 48). The work function of bulk Pt (W_{bulk}) is 5.7 eV (ref 49). The *W* of Pt particles (average diameter: $d = 3.6$ nm) on the Pt_2/Ta_2O_5 catalyst is therefore determined to be 6.0 eV.

[48] Wood, D. M. *Phys. Rev. Lett.* **1981**, *46*, 749−749.

[49] Bardeen, J. *Phys. Rev.* **1947**, *71*, 717−727.

[50] Yamamoto, T. A.; Nakagawa, T.; Seino, S.; Nitani, H. *Appl. Catal., A* **2010**, *387*, 195−202.

[51] Liang, D.; Gao, J.; Wang, J.; Chen, P.; Wei, Y.; Hou, Z. *Catal. Commun.* **2011**, *12*, 1059−1062.

[52] Anpo, M.; Che, M.; Fubini, B.; Garrone, E.; Giamello, E.; Paganini, M. C. *Top. Catal.* **1999**, *8*, 189−198.

[53] Li, T.; Balbuena, P. B. *J. Phys. Chem. B* **2001**, *105*, 9943−9952.

[54] Tominaga, H.; Nagai, M. *Electrochim. Acta* **2009**, *54*, 6732−6739.

[55] Liu, K.; Lei, Y.; Wang, G. *J. Chem. Phys.* **2013**, *139*, 204306.

[56] Kim, Y. D.; Fischer, M.; Ganteför, G. *Chem. Phys. Lett.* **2003**, *377*, 170−176.

[57] Tsunoyama, H.; Ichikuni, N.; Sakurai, H.; Tsukuda, T. *J. Am. Chem. Soc.* **2009**, *131*, 7086−7093.

[58] Ishida, T.; Nagaoka, M.; Akita, T.; Haruta, M. *Chem. - Eur. J.* **2008**, *14*, 8456−8460.

[59] Li, C.; Domen, K.; Maruya, K.; Onishi, T. *J. Am. Chem. Soc.* **1989**, *111*, 7683−7687.

[60] Chen, X.; Zhu, H.-Y.; Zhao, J.-C.; Zheng, Z.-F.; Gao, X.-P. *Angew. Chem., Int. Ed.* **2008**, *47*, 5353−5356.

[61] Photothermal conversion on the photoirradiated Pt particles scarcely occurs in the present system. The temperature increase on the surface of an individual Pt particle in solution under photoirradiation can roughly be estimated by the equation, $\Delta T = \sigma_{abs}I/(4\pi R_{eq}\beta\kappa)$, where σ_{abs} = absorption cross section, I = intensity of the incident light, R_{eq} = radius of a sphere with the same volume as the particle, β = thermal capacitance coefficient dependent on the nanoparticle aspect ratio, κ = thermal conductivity of solvent (ref 62). The σ_{abs} value for <100 nm Pt particle is reported to be $<1 \times 10^{-14}$ m^2 (ref 63). Other parameters for our catalysts are as follows: R_{eq} <25 nm, I = 168 W m^{-2}, $\beta = 1$, $\kappa = 0.137$ W m^{-1} K^{-1} (ref 64). The

theoretical temperature increase, ΔT, is determined with these parameters to be 3.9×10^{-5} K. This very small temperature increase suggests that photothermal conversion scarcely occurs in the present Pt/Ta_2O_5 system.

[62] Baffou, G.; Quidant, R.; García de Abajo, F. J. *ACS Nano* **2010**, *4*, 709−716.

[63] Langhammer, C.; Kasemo, B.; Zorić, I. *J. Chem. Phys.* **2007**, *126*, 194702.

[64] Li, C. C. *AIChE J.* **1976**, *22*, 927−930.

[65] Chun, W.-J.; Ishikawa, A.; Fujisawa, H.; Takata, T.; Kondo, J. N.; Hara, M.; Kawai, M.; Matsumoto, Y.; Domen, K. *J. Phys. Chem. B* **2003**, *107*, 1798−1803.

[66] Horsley, J. A. *J. Am. Chem. Soc.* **1979**, *101*, 2870−2874.

[67] Sexton, B. A.; Hughes, A. E.; Foger, K. *J. Catal.* **1982**, *77*, 85−93.

[68] Shiraishi, Y.; Kofuji, Y.; Kanazawa, S.; Sakamoto, H.; Ichikawa, S.; Tanaka, S.; Hirai, T. *Chem. Commun.* **2014**, *50*, 15255−15258.

[69] The Pt 4f peaks on the Pt_2/Ta_2O_5 catalyst scarcely change even after visible light irradiation (**Figure 3-11**). This clearly indicates that oxidation states and electron density of Pt particles do not change after photoreaction.

[70] Tauster, S. J.; Fung, S. C.; Baker, R. T. K.; Horsley, J. A. *Science* **1981**, *211*, 1121−1125.

[71] Bernal, S.; Botana, F. J.; Calvino, J. J.; López, C.; Pérez-Omil, J. A.; Rodríguez-Izquierdo, J. M. *J. Chem. Soc., Faraday Trans.* **1996**, *92*, 2799−2809.

[72] Ketteler, G.; Ranke, W. *Phys. Rev. B: Condens. Matter Mater. Phys.* **2002**, *66*, 033405.

[73] Yoon, B.; Häkkinen, H.; Landman, U.; Wörz, A. S.; Antonietti, J.−M.; Abbet, S.; Judai, K.; Heiz, U. *Science* **2005**, *307*, 403−407.

[74] Uchihara, T.; Matsumura, M.; Yamamoto, A.; Tsubomura, H. *J. Phys. Chem.* **1989**, *93*, 5870−5874.

[75] Hamanaka, Y.; Nakamura, A.; Omi, S.; Del Fatti, N.; Vallée, F.; Flytzanis, C. *Appl. Phys. Lett.* **1999**, *75*, 1712−1714.

[76] Yeshchenko, O. A.; Bondarchuk, I. S.; Alexeenko, A. A.; Kotko, A. V. *Funct. Mater.* **2013**, *20*, 357−365.

[77] Yeshchenko, O. A.; Bondarchuk, I. S.; Gurin, V. S.; Dmitruk, I. M.; Kotko, A. V. *Surf. Sci.* **2013**, *608*, 275−281.

[78] Shiraishi, Y.; Hirakawa, H.; Togawa, Y.; Hirai, T. *ACS Catal.* **2014**, *4*, 1642−1649.

[79] Shiraishi, Y.; Tanaka, K.; Shirakawa, E.; Sugano, Y.; Ichikawa, S.; Tanaka, S.; Hirai, T. *Angew. Chem., Int. Ed.* **2013**, *52*, 8304−8308.

[80] Shiraishi, Y.; Kanazawa, S.; Kofuji, Y.; Sakamoto, H.; Ichikawa, S.; Tanaka, S.; Hirai, T. *Angew. Chem., Int. Ed.* **2014**, *53*, 13454−13459.

General Conclusions

This dissertation work described highly efficient visible-light-driven photocatalysts based on Pt nanoparticles/semiconductor heterojunction. Chapter I described that Pt/TiO$_2$ catalysts efficiently promote aerobic oxidation of aniline under visible light with much higher activity and selectivity for nitrosobenzene production than those on Au/TiO$_2$. Chapter II described that PtCu/TiO$_2$ promote aerobic oxidation of alcohols with higher activity than those on Pt/TiO$_2$ because the decreased Schottky barrier by the Cu alloying efficiently promotes the e_{hot}^- injection to TiO$_2$. Chapter III described that Pt/Ta$_2$O$_5$ promote aerobic oxidation of alcohols with significantly high activity without e_{hot}^- injection. In that, the e_{hot}^- directly activate O$_2$ on the Pt surface due to the high Schottky barrier and efficiently produce active oxygen species, thus promoting efficient aerobic oxidation.

In Chapter I, the author found that the Pt/P25 catalyst promotes efficient aerobic oxidation of aniline to nitrosobenzene under visible light irradiation (>450 nm). Pt nanoparticles activated by visible light transfer their e$^-$ to the TiO$_2$ conduction band. The positive charge that remained on the Pt surface oxidizes aniline, and the e$^-$ on TiO$_2$ reduces O$_2$, promoting aerobic oxidation of aniline. The high activity of Pt/P25 is ascribed to the high Lewis basicity of Pt particles due to the strong Pt−support interaction at the anatase−rutile interfaces. These Pt particles promote reductive deprotonation of aniline, resulting in the efficient photooxidation of aniline. The catalytic activity of Pt/P25 strongly depends on the amount and size of Pt particles. The catalyst containing 2 wt % Pt particles with ~3 nm diameters exhibits the best catalytic performance. The selectivity for nitrosobenzene formation also depends on the reaction temperature; reaction at low temperatures suppresses condensation of aniline with the formed nitrosobenzene and produces nitrosobenzene with a very high selectivity (~90%).

In Chapter II, the author found that bimetallic alloy nanoparticles consisting of 80 mol % of Pt and 20 mol % of Cu, supported on anatase TiO$_2$, behave as highly efficient photocatalysts for aerobic oxidation under visible light irradiation (λ >450 nm). The activity of the alloy catalyst is much higher than that of the monometallic Pt catalyst. The enhanced activity is due to the decrease in the work function of nanoparticles by Cu alloying. This decreases the height of the Schottky barrier created at the nanoparticle/anatase heterojunction and promotes smooth e$^-$ transfer from the photoactivated nanoparticles to anatase. The activity strongly depends on the size of alloy particles. Smaller particles (<3 nm diameter) have larger work function and create a larger Schottky barrier, resulting in decreased activity. In contrast, larger particles (>5 nm diameter) possess a smaller number of perimeter metal atoms. This thus suppresses smooth e$^-$ transfer from photoactivated nanoparticles to anatase, resulting in decreased activity. As a result of this, alloy

nanoparticles with 3–5 nm diameters exhibit the highest photocatalytic activity. Sunlight activation of the catalyst successfully promotes selective and efficient oxidation of alcohols. The efficient charge separation at the Pt–Cu alloy nanoparticle/anatase interface clarified here may contribute to the creation of more active photocatalysts driven by visible light and the design of photocatalytic systems for selective organic transformation by sunlight.

In Chapter III, the author found that Pt nanoparticles (~5 nm diameter), when supported on Ta_2O_5, behave as visible-light-driven catalysts for efficient aerobic oxidation at room temperature. Visible light absorption of the Pt particles produces a large number of e_{hot}^- via the enhanced interband transition of their 5d electrons. They activate O_2 and produce a large number of peroxide species behaving as key active species for oxidation. The basic concept presented here, based on the enhanced e_{hot}^- formation on the metal particles by an appropriate semiconductor support and the promotion of photocatalysis without e_{hot}^- injection into the semiconductor CB, may contribute to the creation of more active catalyst driven by visible light and to the design of sunlight-driven organic synthesis.

Suggestions for Future Work

This dissertation work described the visible-light-driven photocatalysts with high photocatalytic activity by Pt nanoparticles–semiconductor heterojunction system. The author points out here the extension of this work for the design of Pt/Ta_2O_5 photocatalyst towards the application of sunlight as a light source for organic synthesis.

In Chapter III, the author found that Pt/Ta_2O_5 photocatalyst efficiently activates O_2 on the Pt nanoparticles under visible light irradiation. Visible light irradiation to Pt/Ta_2O_5 produces a large number of e_{hot}^- by absorption of the Pt nanoparticles due to enhancement of interband transition of Pt 5d electrons. They efficiently activate O_2 and produce a large number of peroxide species. Therefore, in the presence of hydrogen atom (H) instead of O_2, photoactivated Pt nanoparticles may activate H, and produce hydride species (H^-). Pt nanoparticles however cannot form H^- stably due to its low hydrogen overpotential.[1] Pd alloying with Pt nanoparticles may form H^- on the alloy nanoparticles due to the stronger H–Pd interaction,[2] Pt–Pd bimetallic alloy nanoparticles may thus promote reduction reactions such as hydrogenation of organic compounds. Previously, our research groups found that Pt–Pd bimetallic nanoparticles loaded on TiO_2 ($PtPd/TiO_2$) promote photocatalytic dehalogenation of aromatic halides with alcohol as hydrogen source under UV irradiation.[3] UV irradiation to $PtPd/TiO_2$ produce CB electrons (e_{CB}^-) by excitation of TiO_2, and the formed e_{CB}^- are trapped to Pt–Pd alloy nanoparticles. In that, $PtPd/TiO_2$ produce H^- by electron donation from Pt–Pd alloy nanoparticles to H atom, which is produced by dehaydrogenation of alcohol. This thus promotes dehalogenation of organic halides under UV irradiation. Pt–Pd bimetallic alloy nanoparticles loaded on Ta_2O_5 ($PtPd/Ta_2O_5$) probably promote photocatalytic dehalogenation of organic halides with alcohol as hydrogen source under visible light irradiation. Visible light irradiation to Pt–Pd alloy nanoparticles produce e_{hot}^- by absorption of metal nanoparticles. The e_{hot}^- produce H^- on the alloy metal nanoparticles by activation of H atom, which is produced by dehydrogenation of alcohol with $PtPd/Ta_2O_5$. The formed H^- induces dehalogenation of organic halides (**Figure 9**). Although the detailed reaction mechanisms remain to be clarified, this alloy system with visible light irradiation would be one of the candidates for the application metal-semiconductor system for highly efficient organic synthesis under visible light irradiation.
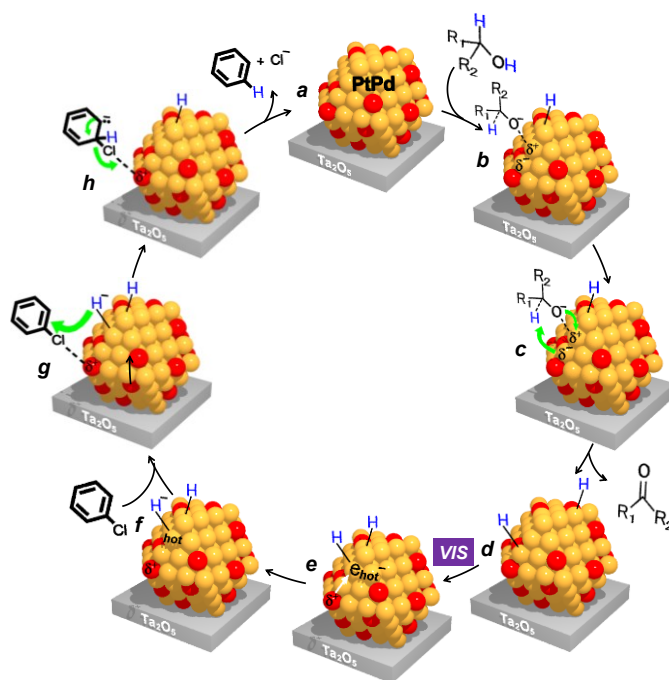
Figure 9. Proposed mechanism for photocatalytic dehalogenation of aromatic halides with alcohol as H source on Pt-Pd/Ta_2O_5 catalyst under visible light irradiation.

In addition, in Chapter III, the author found that Pt/Ta_2O_5 exhibits significantly high photocatalytic activity due to the high electron density of Pt nanoparticles. In the Pt/Ta_2O_5 system, the e_{hot}^- are not injected into Ta_2O_5 conduction band due to the high Schottky barrier. Strong Pt–Ta_2O_5 interaction increases the electron density of Pt nanoparticles by promoting electron transfer from Ta_2O_5 to Pt nanoparticles. It is well known that strong metal–support interaction occurs by high temperature H_2 treatment of metal nanoparticles loaded on reducible metal oxide.[4] In that, Pt nanoparticles loaded on a reducible metal oxide semiconductor, which has high Fermi level, may exhibit high photocatalytic activity under visible light irradiation. It is reported that gallium oxide (Ga_2O_3) is a reducible metal oxide semiconductor, and interacts with Pt by high temperature H_2 treatment.[5] Moreover, Ga_2O_3 has the high Fermi level energy.[6] These results indicates that Pt nanoparticles loaded on Ga_2O_3 catalyst may efficiently activate O_2 by the e_{hot}^- of Pt nanoparticles, and promote efficiently aerobic oxidation under visible light irradiation (**Figure 10**). This may contribute to clarify the influence of SMSI on photocatalytic activity via non-e_{hot}^--injection mechanism, and the design of more efficiently photocatalysts. Although the detailed reaction mechanisms remain to be clarified, this concept would contribute to the improvement of photocatalytic activity under visible light irradiation.
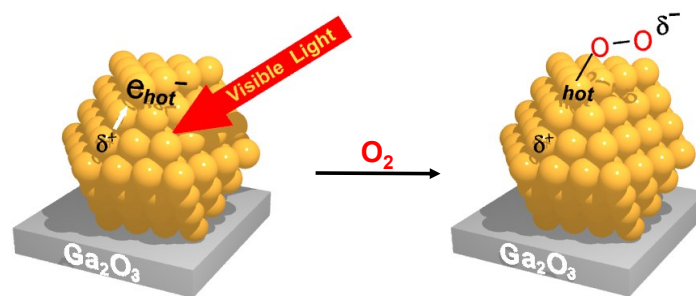
Figure 10. O_2 activation by the e_{hot}^- on Pt/Ga_2O_3 catalyst under visible light irradiation.

References

[1] Ohtani, B.; Iwai, K.; Nishimoto, S.; Sato, S. *J. Phys. Chem. B*, **1997**, *101*, 3349−3359.

[2] Yamauchi, M.; Kobayashi, H.; Kitagawa, H. *ChemPhysChem.* **2009**, *10*, 2566−2576.

[3] Shiraishi, Y.; Takeda, Y.; Sugano, Y.; Ichikawa, S.; Tanaka, S.; Hirai, T. *Chem. Commun.* **2011**, *47*, 7863–7865.

[4] Tauster, S. J.; Fung, S. C.; Baker, R. T. K.; Horsley, J. A. *Science* **1981**, *211*, 1121–1125.

[5] Qu, J.; Zhou, X.; Xu, Feng, X.; Gong, X.-Q.; Tsang, S. C. E. *J. Phys. Che. C* **2014**, *118*, 24452–24466.

[6] Hedge, M.; Hosein, I. D.; Radovanovic P. V. *J. Phys. Chem. C* **2015**, *119*, 17450–17457.

List of Publication

Papers:

(1) **Shiraishi, Y.; Sakamoto, H.; Fujiwara, K.; Ichikawa, S.; Hirai, T.** Selective Photocatalytic Oxidation of Aniline to Nitrosobenzene by Pt Nanoparticles Supported on TiO_2 under Visible Light Irradiation, *ACS Catal.* **2014**, *4*, 2418–2425.

(2) **Shiraishi, Y.; Sakamoto, H.; Sugano, Y.; Ichikawa, S.; Hirai, T.** Pt–Cu Bimetallic Alloy Nanoparticles Supported of Anatase TiO_2: Highly Active Catalysts for Aerobic Oxidation Driven by Visible Light, *ACS Nano*, **2013**, *7*, 9287–9297.

(3) **Sakamoto, H.; Ohara, T.; Yasumoto, N.; Shiraishi, Y.; Ichikawa, S.; Tanaka, S.; Hirai, T.** Hot–Electron–Induced Highly Efficient O_2 Activation by Pt Nanoparticles Supported on Ta_2O_5 Driven by Visible Light, *J. Am. Chem. Soc.* **2015**, *137*, 9324–9332.

Related works

(1) **Shiraishi, Y.; Kanazawa, S.; Sugano, Y.; Tsukamoto, D.; Sakamoto, H.; Ichikawa, S.; Hirai, T.** Highly Selective Production of Hydrogen Peroxide on Graphitic Carbon Nitride (g-C_3N_4) Photocatalyst Activated by Visible Light. *ACS Catal.* **2014**, *4*, 774–780.

(2) **Shiraishi,Y.; Shirakawa, E.; Tanaka, K.; Sakamoto, H.; Ichikawa, S.; Hirai, T.** Spirothiopyran-Modified Gold Nanoparticles: Reversible Size Control of Aggregates by UV and Visible Light Irradiations. *ACS Appl. Mater. Interface* **2014**, *6*, 7554–7562.

(3) **Shiraishi, Y.; Kanazawa, S.; Kofuji, Y.; Sakamoto, H.; Ichikawa, S.; Tanaka, S.; Hirai, T.** Sunlight-Driven Hydrogen Peroxide Production from Water and Molecular Oxygen by Metal-Free Photocatalysts. *Angew. Chem., Int. Ed.* **2014**, *53*, 13454–13459.

(4) **Shiraishi, Y.; Kofuji, Y.; Kanazawa, S.; Sakamoto, H.; Ichikawa, S.; Tanaka, S.; Hirai, T.** Platinum Nanoparticles Strongly Associated with Graphitic Carbon Nitride as Efficient Co-Catalysts for Photocatalytic Hydrogen Evolution under Visible Light. *Chem. Commun.* **2014**, *50*, 15255–15285.

(5) **Hirakawa, H.; Shiraishi, Y.; Sakamoto, H.; Ichikawa, S.; Tanaka, S.; Hirai, T.** Photocatalytic Hydrogenolysis of Epoxides with Alcohol as a Reducing Agent on TiO_2 Loaded with Pt Nanoparticles. *Chem. Commun.* **2015**, *51*, 2294–2297.

(6) **Hirakawa, H.; Katayama, M.; Shiraishi, Y.; Sakamoto, H.; Wang, K.; Ohtani, B.; Ichikawa, S.; Hirai, T.** One-Pot Synthesis of Imines from Nitroaromatics and Alcohols by Tandem Photocatalytic and Catalytic Reactions on Degussa (Evonik) P25 Titanium Dioxide. *ACS Appl. Mater. Interfaces*, **2015**, *7*,

3797–3806.

(7) **Selvam, K.; Sakamoto, H.; Shiraishi, Y.; Hirai, T.** One-Pot Synthesis of Secondary Amines from Alcohols and Nitroarenes on TiO_2 Loaded with Pd Nanoparticles under UV Irradiation. *New. J. Chem.* **2015**, *39*, 2467–2473.

(8) **Selvam, K.; Sakamoto, H.; Shiraishi, Y.; Hirai, T.** Photocatalytic Secondary Amine Synthesis from Azobenzenes and Alcohols on TiO_2 Loaded with Pd Nanoparticles. *New J. Chem.* **2015**, *39*, 2856–2860.

(9) **Shiraishi, Y.; Kofuji, Y.; Sakamoto, H.; Tanaka, S.; Ichikawa, S.; Hirai, T.** Effect of Surface Defects on Photocatalytic H_2O_2 Production by Mesoporous Graphitic Carbon Nitride under Visible Light Irradiation. *ACS Catal.* **2015**, *5*, 3058–3066.

(10) **Shiraishi, Y.; Tanaka, H.; Sakamoto, H.; Ichikawa, S.; Hirai, T.** Amino-Substituted Spirothiopyran as an Initiator for Self-Assembly of Gold Nanoparticles. *RSC Advances,* **2015**, *5*, 77572–77580.

(11) **Hirakawa, H.; Shiota, S.; Shiraishi, Y.; Sakamoto, H.; Ichikawa, S.; Hirai, T.** Au Nanoparticles Supported on $BiVO_4$: Effective Inorganic Photocatalysts for H_2O_2 Production from Water and O_2 under Visible Light. *ACS Catal.* **2016**, *6*, 4976–4982.

(12) **Kofuji, Y.; Isobe, Y.; Shiraishi, Y.; Sakamoto, H.; Tanaka, S.; Ichikawa, S.; Hirai, T.** Carbon Nitride-Aromatic Diimide-Graphene Nanohybrids: Metal-Free Photocatalysts for Solar-to-Hydrogen Peroxide Energy Conversion with 0.2% Efficiency. *J. Am. Chem. Soc.* **2016**, *138*, 1019–1025.

(13) **Kofuji, Y.; Ohkita, S.; Shiraishi, Y.; Sakamoto, H.; Tanaka, S.; Ichikawa, S. Hirai, T.** Graphitic Carbon Nitride Doped with Biphenyl Diimide: Efficient Photocatalyst for Hydrogen Peroxide Production from Water and Molecular Oxygen by Sunlight. *ACS Catal.* **2016**, *6*, 7021–7029.

Acknowledgment